Rotary Jet Spinning of Polymer Fibres

James Jack Rogalski

2018

Submitted in partial fulfilment of the requirements of the
Degree of Doctor of Philosophy

Queen Mary University of London

Statement of Originality

I, James Jack Rogalski, confirm that the research included within this thesis is my own work or that where it has been carried out in collaboration with, or supported by others, that this is duly acknowledged below, and my contribution indicated. Previously published material is also acknowledged below.

I attest that I have exercised reasonable care to ensure that the work is original and does not to the best of my knowledge break any UK law, infringe any third party's copyright or other Intellectual Property Right, or contain any confidential material.

I accept that the College has the right to use plagiarism detection software to check the electronic version of the thesis.

I confirm that this thesis has not been previously submitted for the award of a degree by this or any other university.

Signature:

Date:

Details of Publications:

1. Rogalski, J.J., C.W.M. Bastiaansen, and T. Peijs, Rotary jet spinning review – a potential high yield future for polymer nanofibers. Nanocomposites, 2017. 3(4): p. 97-121.
2. Rogalski, J.J., C.W.M. Bastiaansen, and T. Peijs, PA6 Nanofibre Production: A Comparison between Rotary Jet Spinning and Electrospinning. Fibers, 2018. 6(2): p. 37.
3. Rogalski, J.J., C.W.M. Bastiaansen, and T. Peijs, Rheological Modelling of the Rotary Jet Spinning Process. Polymer Engineering & Science, 2018 (Submitted).

Acknowledgements

Many PhD graduates will be able to confirm that the kind support provided by friends, academics, university support staff and colleagues throughout their research journey proved invaluable. To this end, I would like to start by offering my sincere thanks to everyone who helped and supported me through the last 4 years at Queen Mary University.

Firstly, to all the staff at NanoForce and academics at the university who so kindly donated their time in helping me with queries and experimental setup. My thanks go to Han Zhang, Jian Yao, Olivier Picot, Wei Tu, Ben Milsom and Maurizio Leo. I would also like to thank Russell Bailey from Nanovision for his assistance in SEM imaging and Alice Williams in the materials characterisation lab for all their help.

My thanks go to DSM, Netherlands, without whose financial support this research would not have been possible. A special thank you to Harm van der Werff, Peto Verdaasdonk and Roman Stepanyan at DSM for their support. This work was also partly supported by the UK Engineering and Physical Sciences Research Council (EPSRC), under grant number 1502193.

To my PhD supervisors Ton Peijs and Kees Bastiaansen, whose help, support and encouragement throughout these years has been invaluable. Thank you Kees for our detailed discussions regarding every aspect of my research. You made me think outside the box on several occasions which has no doubt improved my research abilities for the future. Thank you, Ton, for all your guidance throughout my research. In addition to your constant support, you gave me the opportunity to conduct this research project for my PhD in the first place, for which I will always be grateful.

Finally, living with someone who is doing a PhD can never be easy. I cannot thank my wife Laura enough for her unwavering support throughout the last 4 years during every stage of elation and despair that inevitably comes with the successes and failures present in a research project. You are my everlasting ray of sunshine.

Abstract

Polymeric nanofibres can be produced from a variety of methods such as electrospinning and melt blowing, with fibres being produced having applications in many sectors such as biomedicine, composites and filtration. Existing methods are not however capable of producing nanofibres to commercial volumes in an energy efficient way. In this research we investigate a new method of producing nanofibres, namely Rotary Jet Spinning (RJS), which is a relatively new method of fibre production similar to candyfloss production, where centrifugal forces are used to expel jets of polymer from a state of melt or solution in order to produce polymeric fibres. We investigate this method in detail, initially concentrating on the comparison between electrospinning and RJS. Firstly, it was found that electrospinning produced slightly smaller fibre diameters compared to RJS over a broader range of solution concentrations. Secondly, the ability to produce high modulus fibres was investigated by means of an imidization technique, where polyamic acid solution was produced and spun into fibres before conversion to a co-polyimide fibre with an elastic modulus of around 40 GPa. In the third experimental chapter, the viscosity reliability of the RJS process was evaluated by means of computational fluid dynamics simulations, where it was shown that low viscosity (1-10 Pa.s) Newtonian fluids are required to establish fibre production. For fluids with lower viscosities, beading occurred in solution spinning and droplets were produced from melt spinning. Viscosities higher than the recommended value resulted in blockage, with no fibres being produced from either method. Lastly, the production of ceramic fibres was evaluated to establish the ability of the RJS process to produce a ceramic nanofibre. Fibres on the nanoscale were not achieved, however a variation in solvent volatility and crosslinking time were factors in fibre diameter reduction, with solvent variations highlighting the potential of this process to achieve the required fibre size from RJS and thereby demonstrating this technology as a viable option for high volume fibre production.

Table of Contents

List of Figures

List of Tables

1

An Introduction to Rotary Jet Spinning

Polymer nanofibre research is a topical field in the materials world today [1] and is made up of many different types of production and assembly methods based around the development and pace of the technology being introduced. Within each novel way of manufacturing nanofibres, a myriad of uses for each type exists. It is this demand for varying uses which provides the driving force behind the research into newer, better technologies. Each new iteration or technology jump tries to overcome the flaws of their predecessors. This constant innovation and continuing research are looking towards the use of nanofibres to complement the existing burgeoning microfibre industry. Nanofibres, which are fibres typically less than one micrometre in diameter, are slowly being introduced into the market as technologies to successfully manufacture them in large volumes become available.

The manufacturing techniques that are available to produce nanofibres, as well as microfibres, vary greatly, with some techniques offering benefits that supersede others in either volume, cost or environmental qualities etc. While some techniques produce vast amounts of material in a short space of time, others are only capable of producing insignificant amounts not suitable for industrial scale applications.

1.1 Why polymer nanofibres?

There exist many reasons why it is beneficial for certain applications to prefer nanofibres over microfibres, largely due to their ability to offer advantages due to their reduced diameter. Within this nanoscale, the fibres have a greater surface area to volume ratio and tuneable porosity [2], making them attractive for applications such as filtration and composites, where filters may benefit from increased efficiency by reducing the fibre diameter [3], and nanocomposites may show potentially enhanced properties, notably toughness, due to an increase in surface area [4-6]. In a typical filtration application of nanofibre mats as can be seen in Figure 1.1, the pollen spore is incapable of travelling through the nanofibre mat, rendering it a suitable air filtration application for a variety of objects (Figure 1.2).

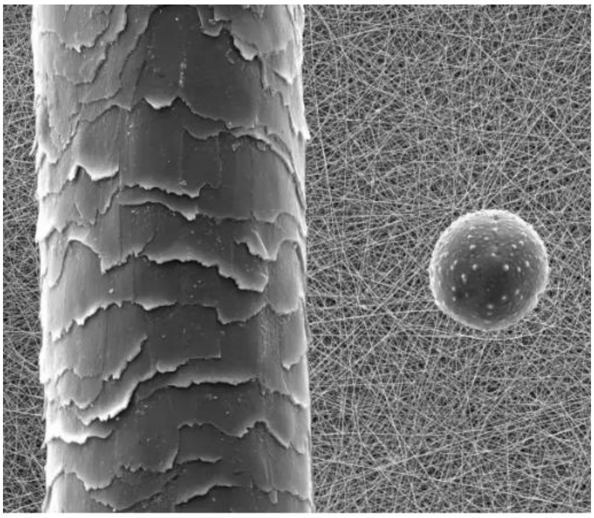

Figure 1.1: Nanofibre scale (Human hair, pollen grain, nanofibre mat). Photograph courtesy of Elmarco [7].

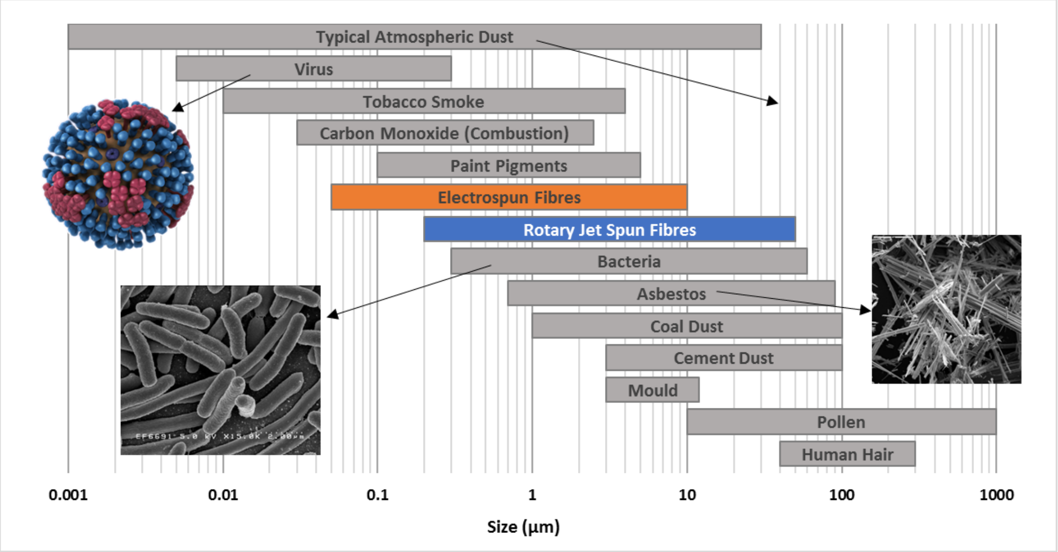

Figure 1.2: Comparison of the sizes of typical objects relevant for air filtration with fibre diameters of RJS and electrospun (ES) fibres.

Currently, nanoscale fibres can be produced using existing techniques such as electrospinning [8-10], melt blowing [11, 12], island-in-the-sea spinning [13-15] and template synthesis [16] to name a few. These methods and others like them, which will only be described in limited detail here, have been the primary method of nanofibre production for some time. There exist drawbacks to many of these methods, be it low production rates or having to using large quantities of energy for fibre production. A more efficient method is needed to create nanofibres which would increase production rates and reduce power consumption. One such method that could answer these requirements is rotary jet spinning (RJS).

1.2 Introducing rotary jet spinning (RJS)

RJS is known by a few names within the research community, however the RJS title sums up the process better than most. RJS is also known as centrifugal spinning, rotor spinning, pressure gyration and Forcespinning™. This last term was introduced as a brand name by FibeRio® Technology Co. (Acquired by Clarcor Inc. in 2016, who were subsequently acquired by Parker Hannifin in 2017), for what appeared to be the only commercial enterprise specialising in the development and production of RJS machinery on the market. It was at the University of Texas where the initial patents were filed by Lozano and Sarkar before being commercialised by FibeRio. [17, 18]

Since the granting of FibeRio's RJS patents in the last decade [17, 19-25], a flurry of research relating to this field has started to emerge. Around a third of publications cited here which utilise RJS as a primary nanofibre production method have used equipment produced by FibeRio in some way, but the majority do not, opting to create their own rotary jet spinning machines instead. Although the mechanics behind RJS are simple and resemble candy floss making machines that have been around for decades, developing a device that is capable of precision control for the benefit of tuneable fibre morphology is key.

To gauge the scale of recent interest in centrifugally spun fibres, results from a patent search into characteristic patent code D01D 5/18 shown in Figure 1.3, which classifies any patent relating to natural or artificial threads or fibres created by means of rotating spinnerets, shows the filing of patents since the year 2000. Under this classification, which is included as one of multiple classifications in a patent registration, all the equipment or processes that are being patented are directly related to polymer nanofibre manufacturing or applications.

More patent categories exist which give an overview of the rise of this technology, however this classification code search depicts the trend well enough to consider only one type for illustration purposes.

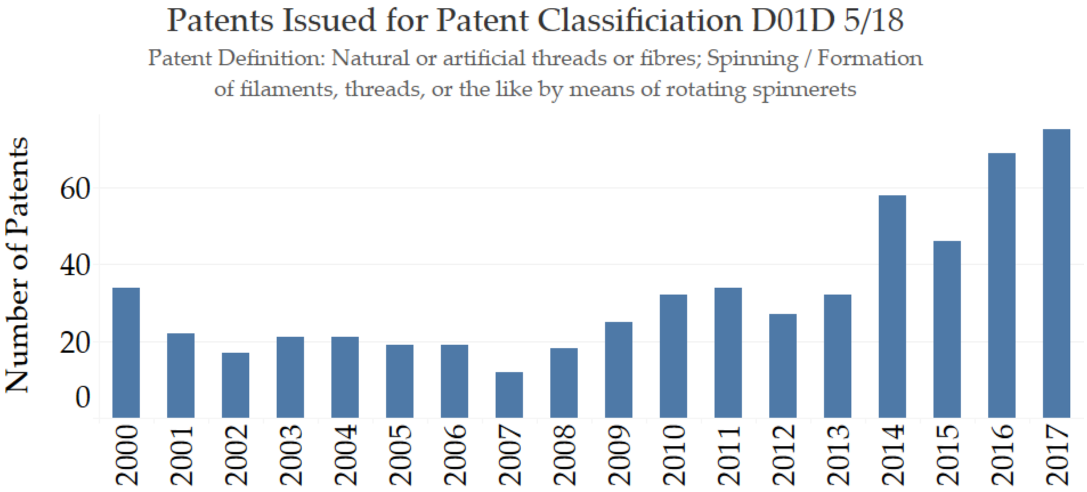

Figure 1.3: Number of patents issued matching the RJS related classification since 2000. Data compiled from Espacenet.com [26].

The highest number of patent registrations come from China and the United States, with a steady rise in patents relating to fibre spinning occurring since 2007, and a slight reduction from both the USA and China in 2012 and 2013. Recent years account for the highest registrations, indicating a continued interest in the technology, with 2017 being the largest number to date. Figure 1.4 shows a geographical representation of the countries that are most active in patent registrations for this classification, highlighting China and the USA's overall dominance.

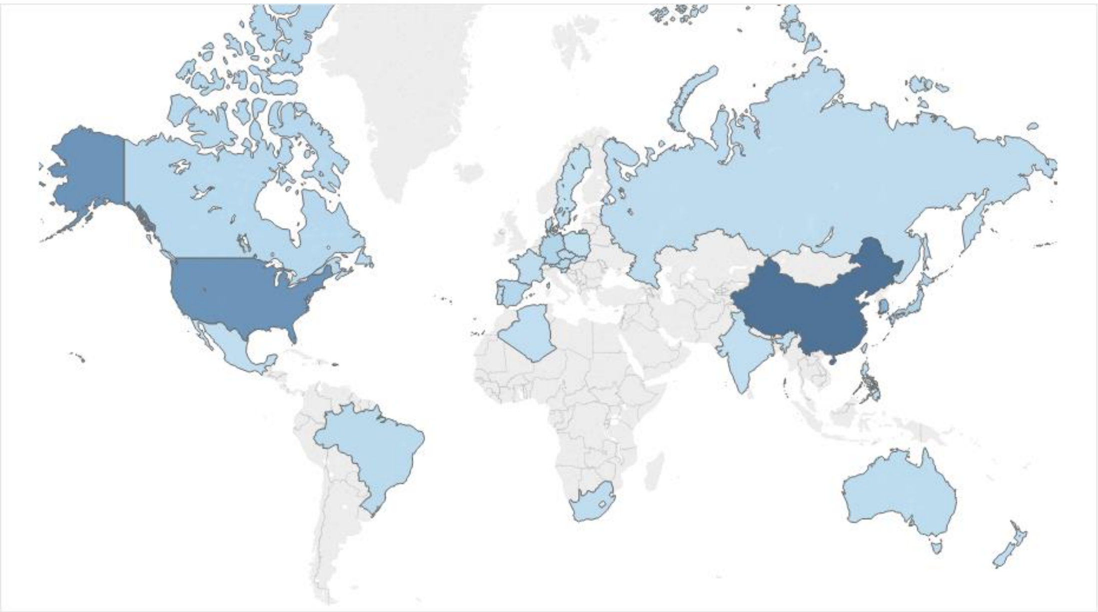

Figure 1.4: World Heat Map representing the most active countries in registrations for RJS related patents by total volume from 2000 to 2017. Data compiled from Espacenet.com [26].

Publications relating directly to RJS, the primary focus of this review, can be seen in Figure 1.5. These illustrate the number of scientific publications per year according to Web of Science (WoS) since this technology started to gain traction. The search was conducted using all aliases for RJS as previously described. Data before 2010 shows virtually no publications on this specific subject.

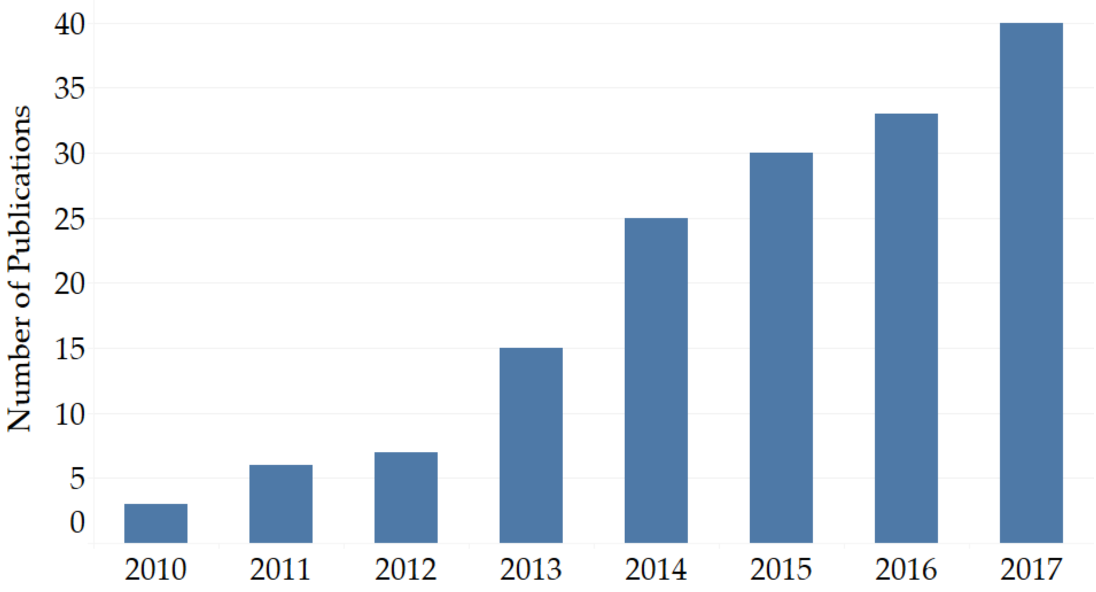

Figure 1.5: Publications related to RJS by year from 2010 to 2016, according to WoS.

The fundamental principle behind RJS is relatively straightforward although the technology does require some knowledge of polymer chemistry, processing and fluid mechanics. The basic concept of RJS is illustrated in Figure 1.7 and is not too dissimilar to a well-known method used in the catering industry for the manufacture of candy floss.

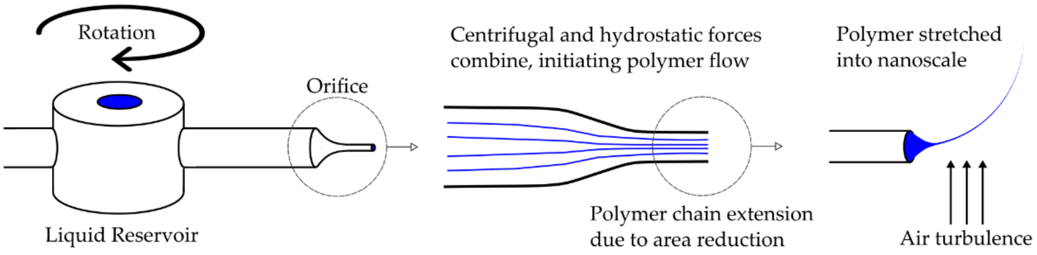

Figure 1.6: Illustration of the RJS process, demonstrating the effect of centrifugal forces expelling polymer solution or melt through the geometry constriction, before being stretched by the rapid rotation and air flow over the polymeric fibre.

Basic requirements in RJS are a reservoir to hold the polymer, which is in either solution or melt form, and a nozzle through which the polymer is spun once it is rotated at a high enough angular velocity to initiate jet expulsion. In addition to this, a collector to "catch" the fibres after they are spun and stretched in the air vortices as they make their way from the nozzle is also needed. This can take many forms, but the most common method used is a radial array of vertical collector bars. A collection of images shown in Figure 1.7 detail the existing table-top laboratory versions and the industrial versions of the Forcespinning® products produced by FibeRio, along with a nanofibre spinning demonstration.

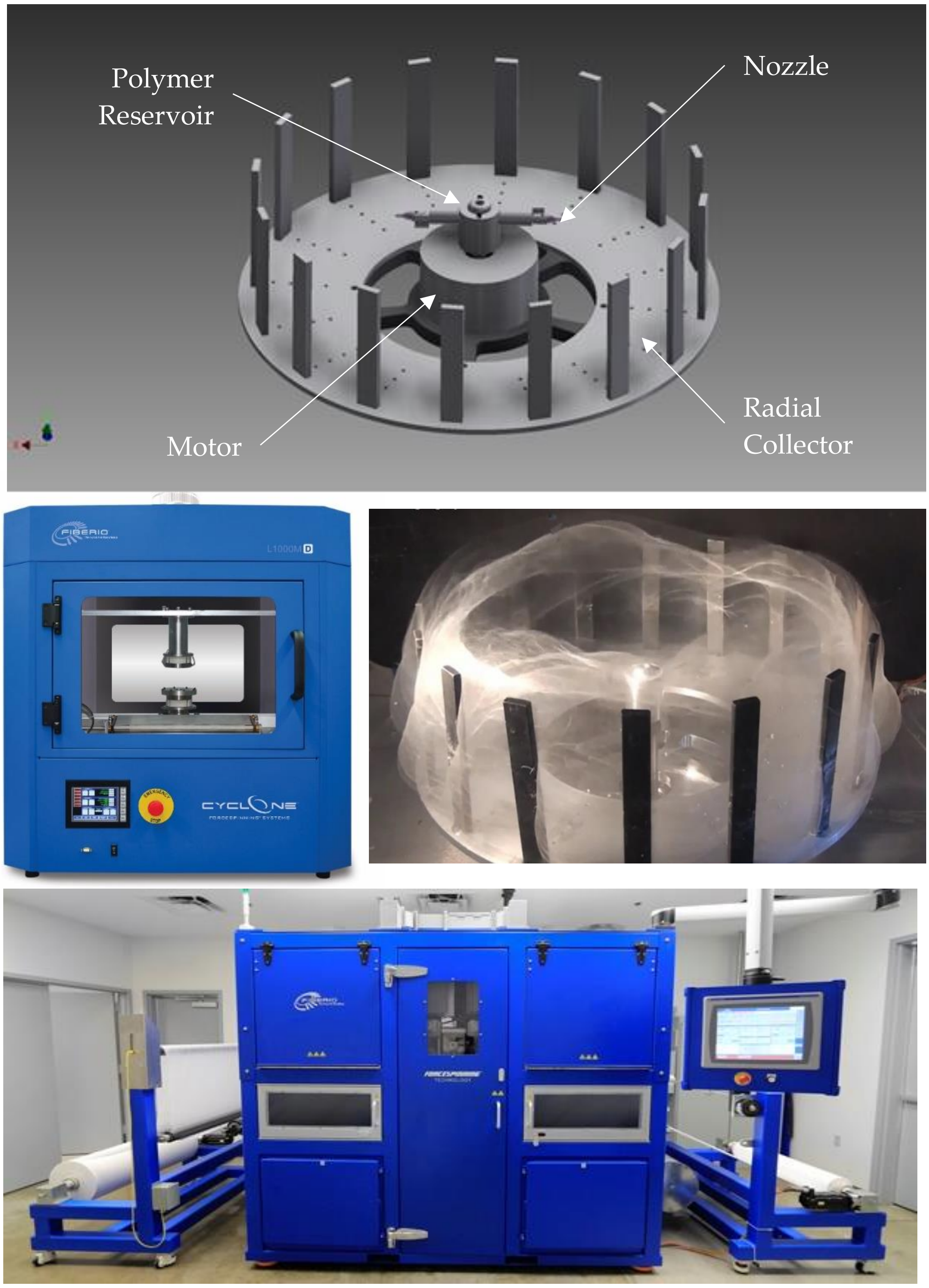

Figure 1.7: Schematic illustration of rotary jet spinning (RJS), comprised of an electric motor driven rotating spinneret with polymeric fibres being ejected outwards towards the vertical collector bars in this typical setup. Photographs (top left to bottom) of the FibeRio Cyclone™ L1000M laboratory machine, with fibre spinning demonstration, and the Fibre Engine FX System which is configurable for 1.1-meter (FX1100) or 2.2-meter (FX2200) line widths, achieving an output of up to 200 grams per minute and compatible with line speeds of up to 200 meters per minute. Photographs courtesy of FibeRio.

1.3 Comparisons with other techniques

Many techniques other than RJS can be used to create polymeric nanofibres, but none with as much capacity for industrial scaling using such low power consumption. Other nanofibre production methods include drawing [27, 28], template synthesis [16, 29, 30], phase separation [31], self-assembly [32-34], islands in the sea [14, 35], electrospinning [8-10, 36-41] and melt-blown spinning [12, 42-44]. Each of these processes have distinct advantages and disadvantages, which have been summarised by Nayak et al. [45] are presented in Table 1.1.

Table 1.1: List of nanofibre production methods. After Nayak et al. [45]

Manufacturing process	**Scope for scaling-up**	**Repeat-ability**	**Control of fibre dimension**	**Advantages**	**Disadvantages**
Electrospinning (solution)	Yes	Yes	Yes	Long and continuous fibres	Solvent recovery issues, low productivity, jet instability
Electrospinning (melt)	Yes	Yes	Yes	Long and continuous fibres	Thermal degradation of polymers, electric discharge problem
Melt blowing	Yes	Yes	Yes	Long and continuous fibres, high productivity, free from solvent recovery issues	Polymer limitations, thermal degradation of polymers
Island in the sea spinning	Yes	Yes	Yes	Long and continuous, relative uniformity	Solvent recovery and extra processing
Template synthesis	No	Yes	Yes	Easy to vary diameter by using different templates	Complex process
Drawing	No	Yes	No	Simple process	Discontinuous process

Manufacturing process	**Scope for scaling-up**	**Repeat-ability**	**Control of fibre dimension**	**Advantages**	**Disadvantages**
Phase-separation	No	Yes	No	Simple equipment required	Only works with selective polymers
Self-assembly	No	Yes	No	Easy to obtain smaller nanofibres	Complex process
Rotary jet spinning	Yes	Yes	Yes	Free from very high voltage, eco-friendly	Requirement of high temperatures

Although RJS is sometimes labelled as "eco-friendly", the process can only be credited as such if the solvent is recycled or not used at all, such as with melt RJS. However, alternative methods used to produce fibres from the melt can use significantly more energy, thus making them less environmentally friendly. In all of these melt processing techniques thermal degradation is a possibility, but can be overcome by using thermal stabilizers [46].

1.3.1 Electrospinning

Electrospinning (ES) is a method that relies on an electrostatic force to spin a fibre from a polymer solution droplet suspended from a capillary by overcoming the surface tension in the droplet to form fibres on a counter electrode [39, 47-51]. This can be conducted through a single needle approach (Figure 1.8), or multiple needles can be used to increase production rate of fibres. Needleless systems such as Elmarco's Nanospider™ technology also exist, allowing semi-industrialised volumes of fibre to be produced on a scale of <200 g.h^{-1} using polyvinyl alcohol (PVA) for example [7, 50].

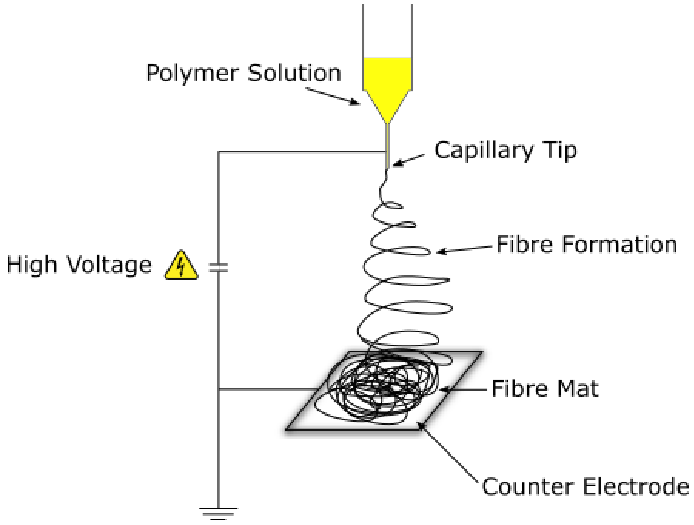

Figure 1.8: Typical electrospinning setup showing the polymer solution being delivered through a needle to a capillary tip, before being caught in the electrostatic attraction of the counter electrode, drawing a fibre across the void into the whipping zone before being deposited as a fibre mat.

When comparing electrospinning with RJS, we can demonstrate the variance in parameters such as fibre diameter with some ease. In comparing the production of poly(ethylene oxide) (PEO) fibres from these two systems, similarity can be gauged and discussed. Won et al. [52] produced beadless nanofibres through the electrospinning of a PEO/water solution at concentrations of 3, 4 and 7 wt.%. The average fibre diameters were between 0.36 μm and 1.96 μm, with the larger diameters a result of other solvents such as ethanol, chloroform and dimethylformamide (DMF). This can be directly compared with PEO/water solutions ranging between 6 and 10 wt.% produced by Padron et al. using RJS [53] in which fibre diameters obtained were 0.13 – 0.32 μm dependant on angular velocity of the spinneret. A conclusion can be drawn from this simple comparison that the diameters achievable from electrospinning are comparable to Rotary Jet Spinning.

1.3.2 Melt blowing

Although we will not cover all techniques in this review, it is important to compare RJS with other techniques such as melt blowing (Figure 1.9). This technology utilises fast flowing heated air and dies to extrude a polymer melt, where after the produced fibre is carried along in the stream of hot air, which is typically the same temperature as the die, before being deposited on a collection device [11]. This stream of heated air flows at very high velocities which is very energy consuming due to the high velocity and temperatures which are required [42].

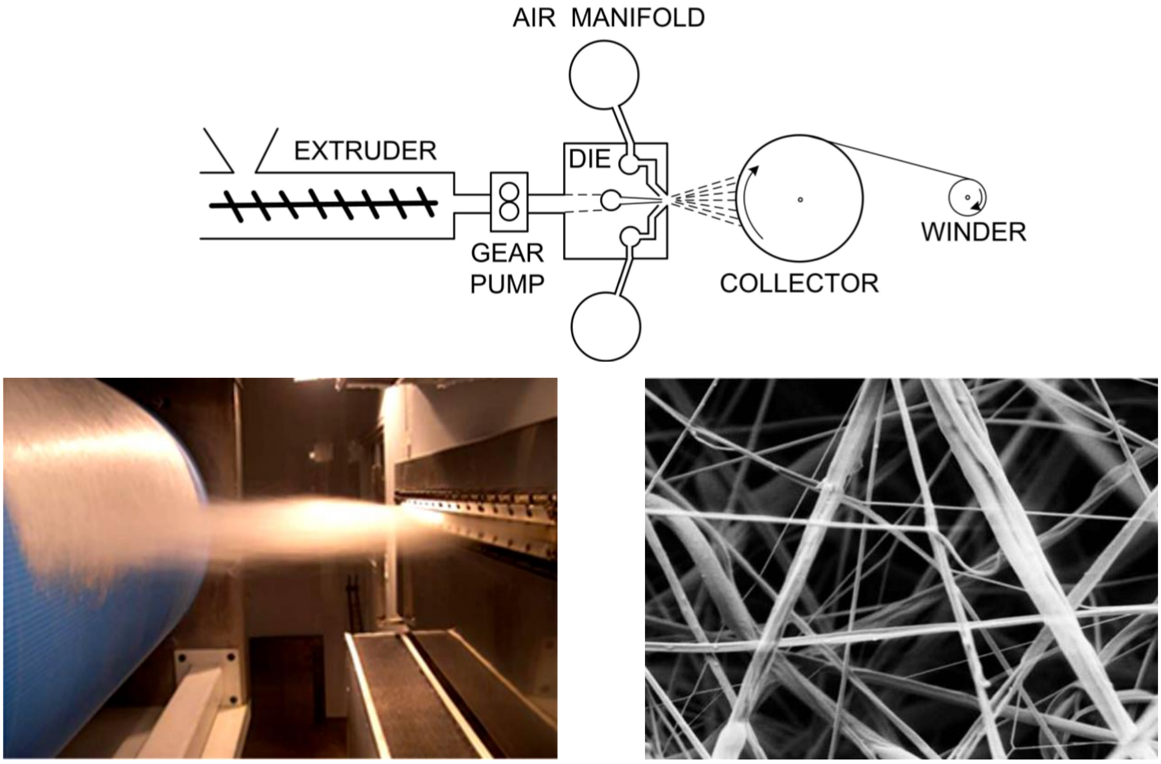

Figure 1.9: Schematic of the melt blowing process where heated air moves at speed past a polymer melt to create fibres (top). Image of the melt blowing process and produced fibre. Reproduced from Hiremath & Bhat [54].

1.3.3 Other methods

Template synthesis is a method that consists of creating nanowires by filling a porous template that contains a large number of straight cylindrical holes with a narrow size distribution. Although scientifically interesting it is however not suited for large scale industrial production [16]. Drawing, phase separation and self-assembly are also not suitable for large scale applications and will not be discussed further here as a comparison to RJS.

The island-in-the-sea method of nanofibre creation is however a method that can be scaled towards mass production but does not produce continuous fibres. It is based on the use of two incompatible polymers which are melt blended together to form a morphology replicating that of islands in the sea, where the islands are the nanofibres and the sea is the sacrificial matrix used to aid in the drawing of the fibres [55].

1.4 Efficiency and yield of RJS

RJS shows promise towards market adaptability when combined with considerations such as energy efficiency. In RJS we do not require the high voltages that come with electrospinning or the high velocity air jets that are required in melt blowing – both of which are relatively large contributors to the overall cost of fibre production. Another benefit afforded to RJS is that (when melt spinning) we do not have to rely on the use of harmful solvents, resulting in a "greener" product – a feature which is however also possible with most other fibre production methods.

Lab scale versions of RJS machines can already produce more than 50 times the rate (60 $g.h^{-1}$ per orifice [53] versus 0.11 $g.h^{-1}$ [50, 53]) of a single needle lab scale electrospinning setup if only comparing one orifice. The standard number of orifices on a RJS machine would be at least 2, some with many more, dependant on design, meaning a 100 fold increase in production rate for a lab scale RJS machine over a single needle electrospinning machine. RJS spinnerets can in turn be positioned in parallel to create a system which covers a larger area for creating continuously fed nonwoven mats.

Exploring the production rates of processes capable of producing industrial volumes of nanofibres highlights even more the differences between methods when considering the commercial future of polymer nanofibres. FibeRio's Cyclone™ Fibre Engine FX System, which is designed with a modular and expandable architecture configurable for 1.1-meter (FX1100) or 2.2-meter (FX2200) line widths, can achieve continuous outputs of up to 12000 $g.h^{-1}$ with line speeds of up to 200 $m.min^{-1}$ and controllable fibre diameters of around 500 nm [56]. In comparison, the highest production rates of the leading electrospinning systems are 210 $g.h^{-1}$ for Inovenso's Nanospinner416, 1-meter line width needleless electrospinning system, depending on polymer solution used (see Table 1.2).

Table 1.2: A comparison of industrial nanofibre production systems, showing manufacturer's quoted production rates of continuous nanofibre deposition on substrates, with the FibeRio FX2200 RJS system being the highest.

Manufacturer	**Nonwoven mat output width**	**Quoted production rates**
Nanospider™ (NS 8S1600U) by Elmarco (Liberec, Czech Republic)	1600 mm	78 g.h^{-1} 1680 m.h^{-1} 2640 m^2.h^{-1} [57]
NW-101 by MECC Co. Ltd (Fukuoka, Japan)	600 mm	600 m.h^{-1} [58]
Nanospinner416 by Inovenso (Istanbul, Turkey)	1000 mm	210 g.h^{-1} 210 m^2.h^{-1} [59]
SPIN line by SPUR® (Zlin, Czech Republic)	1200 mm	192 g.h^{-1} 300 m^2.h^{-1} [60]
Fluidnatek LE-1000 by Bioinicia (Valencia, Spain)	3000 mm	Not Available
FX2200 by FiberRio (McAllen, Texas, USA)	2200 mm	12000 g.h^{-1} 12000 m.h^{-1} [56]

In addition to the Nanospider™ needles systems, multi-jet systems have been developed and are now commercialised by companies such as 4SPIN (Czech Republic), MECC Co. Ltd (Japan), Inovenso (Turkey), SPUR (Czech Republic), and Fluidnatek (Spain). These systems are complex to provide direct production rate comparisons for due to manufacturers quoting various fibre diameters, polymers, solutions and deposition thicknesses, and in some cases only machine speed capabilities. All systems except the RJS FX2200 are electrospinning machines. The only real alternative contender for micro and nanoscale fibre production is melt blowing, which is capable of production rates of around 1500 g.h^{-1} [45], but does not provide continuously uniform fibre diameters in the nanoscale.

1.5 Fibre diameters

Figure 1.10 shows the fibre diameters of published RJS data from a range of studies [53, 61-85]. The large variability in diameters is generally due to different processing settings (e.g. rotational velocity, orifice size, temperature) and material characteristics (e.g. viscosity, molar mass), rather than statistical variability. Viscosity affects the fibre diameter in RJS and Figure 1.10 shows a wide variety of fibre diameters for studies that have reported a range of sizes for certain materials. Where only a small diameter variance is shown, the publication often did not specify an upper and lower diameter range, but rather mentioned only a single value. Values quoted are mean values of all samples measured by the studies, and for simplicity in comparison, does not include the error or standard deviation values in this figure.

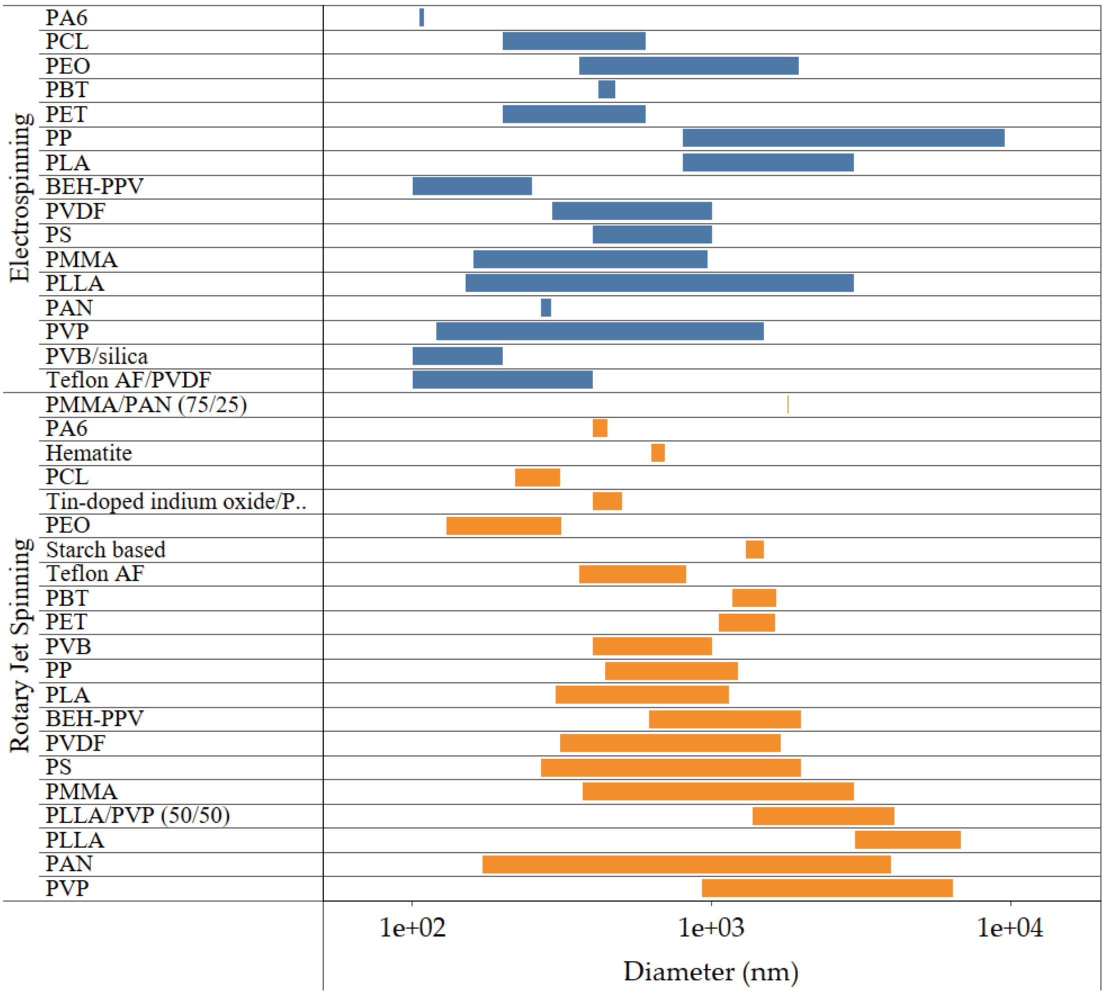

Figure 1.10: A comparison of reported fibre diameter ranges for rotary jet spinning [53, 61-85] and electrospinning [41, 52, 86-96].

These fibre diameters illustrate the typical values that can be achieved with the materials shown. Data shown does not necessarily represent the smallest diameters that are possible with this technology but are an indication of what has so far been achieved. Comparing the smallest diameters of 10 materials from RJS and ES indicated that reported diameters for ES are on average around 10% smaller for the sample taken. However, electrospinning has been around for much longer and these smaller diameters could be simply the result of a better understanding of the ES process, rather than some intrinsic limitation of the RJS process.

There is however a larger variation in the uniformity of fibre diameter in RJS compared with ES. The increase and spread in fibre diameters for RJS in comparison to ES can be attributed to, but not limited to, the phenomenon that occurs during the start-up process. For example, in the solution spinning of polycaprolactone (PCL) in dichloromethane, Figure 1.11 shows diameters for the initial duration of RJS, where a reduction in the fibre diameter is evident up to an equilibrium point at 30 seconds. Taking these initial larger diameter fibres into account when measuring the average diameter will increase reported values and skew like for like comparisons. In almost all reported RJS fibre diameters, this phenomenon is not considered or at least mentioned for consideration. It should be noted that the diameters achievable in a continuous RJS device would reach the equilibrium state at a much smaller diameter to that of the start.

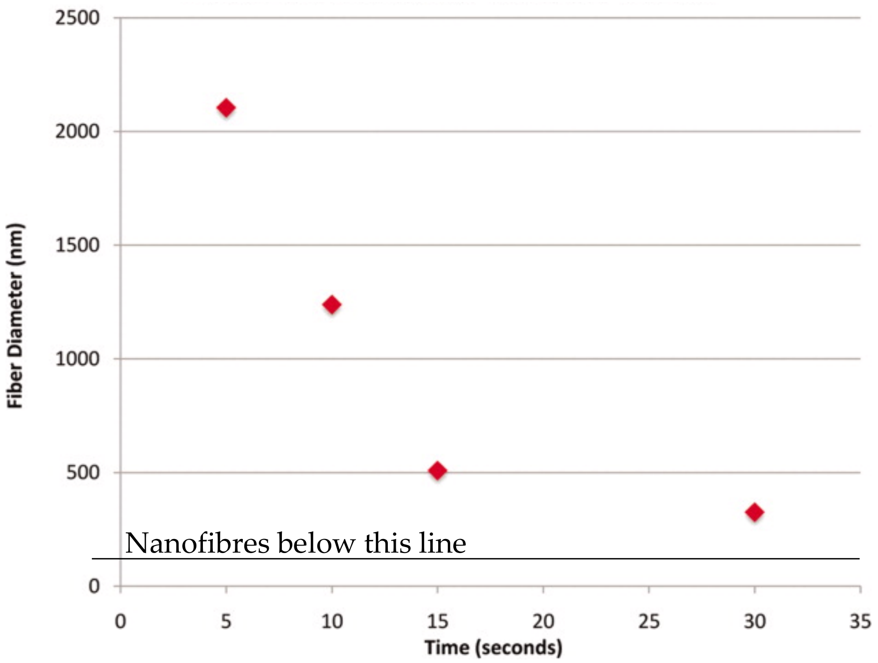

Figure 1.11: Fibre diameter at various spinning times, showing a diameter reduction of RJS fibres during initial 30 seconds start up time, demonstrating the potentially skewed data of reported fibre diameter distributions if start up effects are not considered. Reproduced from McEachin et al [63].

1.6 Potential nanofibre applications

The nanofibre industry is a global marketplace with many vendors such as Donaldson Company, Finetex EnE, FibeRio Technology, Elmarco, Asahi Kasei and eSpin Technologies having the largest presence. A market research report by Tecnnavio claims that the global nanofibre market will steadily grow by an annual compound growth rate of around 28% by 2021, with the textile industry being accounting for as the primary growth factor [97]. According their report, the textile industry will leverage specific nanofibre properties such as hydrophobicity and antibacterial applications, while other industries will leverage nanofibres to replace conventional superabsorbent polymers for their eco-friendliness.

1.6.1 Biomedical

A commonly published nanofibre application in RJS is based around biomedicine. This application exploits the ability of the nanofibres to offer significantly increased surface area to volume ratios than any other material, which is a highly desirable property in this field. Pelipenko et al. [98] describe that these novel materials can be employed in the treatment of various diseases as well as in the field of regenerative medicine. The promise is that biological function lost in host tissues will be able to be restored and maintained using newly developed tissue engineering procedures, using nanofibres [99-102]. A common goal in the design of tissue engineering scaffolds is to mimic the natural interfaces that interact selectively with a specific cell type through biomolecular recognition [103, 104].

Like tissue scaffolds, wound dressings are another biomedical application which has seen much focus, exploiting high surface areas within the nanofibres to foster the perfect conditions for cell growth, embryologic development, organogenesis and wound repair [105, 106].

Using RJS nanofibres in direct contact with the human body is only one aspect of the biomedical applications of nanofibres. Zhu et al. [107] for example, have investigated affinity absorption materials by functionalising poly(vinyl alcohol-co-ethylene) (PVA-co-PE) with Cibacron Blue F3GA to evaluate their effectiveness. Affinity membranes can selectively remove bacteria, endotoxins and viruses from biologically active liquids and water, and if it becomes cheaper to manufacture these types of products, it could benefit developing nations battling against waterborne disease.

Another interesting biological application for RJS nanofibres is that of controlled drug release [104, 108-111]. By being able to provide a predictable and controlled drug release over time by exploiting the high volume to surface area of nanofibres, one such study by Wang et al. using RJS has shown that producing aligned fibre mats are preferable when designing for a slower and more controlled release of drugs, rather than a more rapid release for random oriented fibres due to the increased aqueous interaction. In their research, a lab-built device was used to produce polyvinylpyrrolidone (PVP) fibres between 6 and 19 μm in size via combination of electrospinning and rotary jet spinning [110].

1.6.2 Composites

Another interesting application area for nanofibres is their use within composites or nanocomposites. This area has seen research from nanofibre production areas such as electrospinning [112-115] and vapour grown carbon fibres (VGCF) [116, 117] in the past, with multiple reviews written on their promising future [4, 118-120]. Engineering composites typically consist of high modulus (> 50 GPa) and high strength (> 1 GPa) fibres embedded in a low modulus polymer matrix, which through the interaction between the two, leads to improved mechanical properties of both materials to a level more than which would be expected from each material individually. Increased mechanical strength from nanofibres will be a requirement should nanofibre based composites be successful, but only limited success has been seen to date as reviewed in detail by Yao et al. [8] and Peijs [121]. Various polymeric materials have been trialled as composite reinforcement, with higher modulus materials such as glass [115, 122] and carbon [115, 123] nanofibres being among them. Polymer nanofibres, most often produced by electrospinning, typically have Young's moduli of less than 3 GPa and tensile strengths below 300 MPa [8], which renders them rather ineffective as reinforcement for bulk engineering plastics such as epoxies, polyesters, polyamides or polypropylenes [121]. However, it has been shown that such fibres can be effective as reinforcements for biomedical engineering purposes when combined with hydrogels [124].

Manufacturing fibres in the nano-scale is of great interest for composites, as these fibres have a high aspect ratio and large available fibre surface area, potentially leading to high energy absorption mechanisms through debonding and pull-out. As a simple example, a 10 μm diameter microfibre has the same cross-sectional area as 10,000 nanofibres with diameter 100 nm – resulting in much more surface area to interact with a composite matrix to aid in energy absorption processes as described above [125].

Papkov et al. [126] found that by reducing the diameter of electrospun polyacrylonitrile (PAN) fibres from 2.8 μm to ~0.1 μm increased the elastic modulus from 0.36 to 48 GPa, with the largest increase in elastic modulus below 250 nm (see Figure 1.16). This increase was also commented on by Yao et al. [8] in their review of high strength and high modulus electrospun nanofibres, where it is noted that this is not the only method of achieving increased mechanical properties. Flexible chain polymers generally achieve chain alignment (and thereby higher modulus and strength) through post-drawing, whereas rigid-chain polymers offer the ability to chemically guarantee higher chain alignment during the spinning process.

Two examples of rigid chain polymers being used to produce high mechanical strength nanofibres for use in composites has been investigated using poly(p-phenylene terephthalamide) (PPTA) [38] and also polyimide (PI) [127]. A composite of electrospun co-polyimide nanofibres within a styrene-butadiene-styrene (SBS) triblock copolymer (Kraton®) matrix was produced, where a Young's modulus ranging from ~2.5 GPa to ~7 GPa was achieved for fibre volume fractions ranging from 21% to 62%, respectively. These values were in good agreement with predictions made using the rule of mixtures (gROM) [127]. For this, the fibre orientation in the composite laminates was measured, showing an average misalignment angle of 14°. By back calculating the values obtainable for a fully aligned fibre mat a Young's modulus of 26.5 GPa was estimated for a perfectly aligned UD laminate, yielding a co-polyimide fibre modulus of around 60 GPa, which is similar to commercial high-performance fibres like Kevlar 29.

During electrospinning, albeit on a smaller scale, it is possible to obtain good levels of fibre alignment using the rotating disc method, but an equivalent of such method has not been produced for RJS yet. Badrossamay et al. [128], Erickson et al. [129] and Wang et al. [110] have developed their own RJS systems to produce aligned fibres, although these studies combined both electrospinning and RJS to achieve this. No reported study has yet achieved a high level of fibre alignment using RJS without the aid of electrospinning.

1.6.3 Filtration media

The physical separation of matter occurs predominantly in one of two methods, filtration or sedimentation. Fibres work extremely well when it comes to filtration to separate matter, as they can be scaled according to the size required. The size of the nonwoven fibre mat porosity required depends on the droplet or particle size that needs to be prohibited from passing through. Filters can be made of many materials, with the most common being natural fibres, synthetic polymers, metals, carbon, ceramics and paper-like materials [130].

A typical high-performance filter such as a high efficiency particulate air (HEPA) filter is required to have a minimum removal efficiency of 99.97% of particles greater than or equal to 0.3 μm in diameter in an air flow rate between 3-10 $m.s^{-1}$ (as defined by the United States Department of Energy, DoE in the USA, or a range between 85% - 99.999995% in Europe (European Norm EN 1822:2009). There is also a specification of minimal pressure drop over the filter of around 300 Pa.

Fibre based filter costs are at the low to mid-range price compared to other materials such as paper, with new technologies such as RJS hoping to introduce new methodologies for old technologies. According to data published in the Filters and Filtration Handbook [130], the retail price of spunbound fibre filters range from \$0.065 - \$6.50/m^2, whereas paper filters are the cheapest at \$0.20 to \$0.33/m^2.

Among the most prominent concerns when developing filtration media is the ability of the filter to maintain its usefulness and prevent further harm to users when used as an air filtration device. Because most polymer nanofibres are continuous, there is very little chance of them becoming airborne and entering the body. In addition to this benefit, a primary advantage of using nanofibres in filtration applications is their high surface to volume ratio which increases particulate filtration efficiency, and by nature of the design, results in surface loading instead of depth loading as is typical of other nonwoven substrates [131]. This is achieved by increasing the number of overlapping fibres that exist which will limit the flow of particles by trapping them. Therefore, a smaller diameter and hence more fibres result in a higher ratio of blockage points for travelling particulate matter.

Figure 1.12 shows a standard HEPA filter test of varying air flow rates conducted on polyamide (PA) 6 nanofibre mats, comparing with the industry standard HEPA filter [132]. Samples 1 and 2 were 10 and 5 times thinner respectively than the standard HEPA filter being tested, and pressure drop data suggested that the HEPA filter had the lowest pressure drop compared to the PA 6 filters. Although this shows superior efficiency from the HEPA filter, the potential to use significantly less material in the PA6 filter versus the HEPA filter, for similar filtration efficiencies, shows promise.

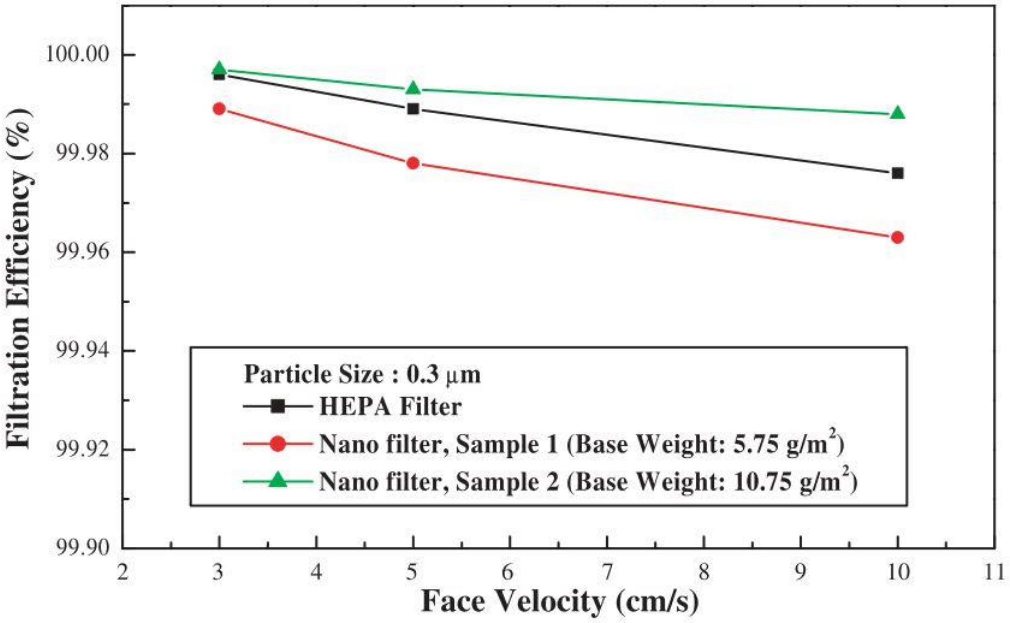

Figure 1.12: Filtration efficiency of PA6 nanofibre filters. A standard HEPA filter is compared with two base weight nanofibre mats with average fibre diameters of 200 nm. Doubling the base weight led to a demonstrable increase in efficiency. Reproduced from Ahn et al. [132].

A real world study of nanofibres for use in air filtration was conducted at Kaufman North Pit in Clearfield Country, Pennsylvania, USA, where a mining vehicle had a comparable cellulose filter tested against a cellulose + nanofibre filter [3]. The result was a reduction in dust particles from 86% to 93%, concluding in a successful trial of the retrofitted nanofibre air filters.

In an attempt to improve the efficiency of filters, Podgorski et al. demonstrated that there is an increase of up to 2.6 times the quality factor (QF) of nanofibre based filters versus those created using microfibres [133], where QF is a method to evaluate filter performance by measuring the filter efficiency as well as the pressure drop over the filter.

1.6.4 Additional potential applications

Although a subset of potential nanofibre applications has already been listed, it is important to note a few more which are currently being researched by use of RJS. One such application, in a bid to improve sensor technology, is in the development of polyaniline (PANI) nanofibre gas sensors by utilising the ability of conducting polymers to display a transition between insulating and conducting states which may occur due to chemical treatments with redox agents. This method can be used to develop optical, chemical and biosensors [134].

Flexible solar cell technology has been investigated by creating nanostructured films from poly(3-hexylthiophene) (P3HT) fibres by mixing them with a molecular acceptor such as [6,6]-phenyl C61-butyric acid methyl ester (PCBM) in solution. By using this process, one could produce an efficient layer of an organic solar cell [135].

Further potential applications being studied include supercapacitors based on flexible graphene/polyaniline nanofibre composite films [136], graphene/polyaniline nanofibre composites as supercapacitor electrodes [137], lithium-ion battery separators from polyacrylonitrile (PAN) [77, 138], polystyrene (PS) nonwoven fabrics featuring radiation induced colour changes [139], nanofibre hydrophilic studies [70, 140, 141] and anionic dye adsorption techniques [142] to name but a few.

1.7 Materials used in rotary jet spinning

Many polymeric materials have been considered for RJS of nanofibres, with material choice driven by specific fibre characteristics stemming from research goals or end-user applications. Applications and future research directions into nanofibres including RJS fibres are attributed to a few key areas of interest, namely filtration [3], healthcare, environmental engineering, biotechnology, composites [121], defence & security and the energy sectors [143].

Many researchers have started studies into RJS nanofibres driven by applications within specific sectors such as medicine, where fibres resemble cellular topographies [63] or are capable of targeted outcomes such as drug delivery [68]. Others have focused on using conjugated polymers in the RJS process for areas such as photovoltaic cells, light-emitting diodes and biocompatible materials [64]. The fibres that are created for these purposes are spun from either a melt state or a solution state, all of which are listed below.

1.7.1 Solution spinning materials

As a relatively new technique for producing fibres, RJS is still undergoing an interesting period of initial research, whereby the materials that are being selected are seemingly either for general research into the RJS technique itself, or they target potential end use applications. The materials chosen are for a relatively broad range of potential applications, but the most common theme amongst specific research is in the field of biomedicine (See Table 1.3).

Table 1.3: RJS (solution) materials choices from published data.

Polymer	**Application**	**Ref.**
Poly(lactic acid) (PLA) Polyethylene oxide (PEO) Gelatine	Biomedical, tissue engineering	[61]
Poly(2,5-bis(20-ethyl-hexyl)-1,4-phenylenevinylene) (BEH-PPV) Polyethylene oxide (PEO)	Photo-luminescent qualities for applications in light emitting diodes	[64]
Polycaprolactone (PCL)	Study of RJS process	[63, 144]
Polyvinylidene fluoride (PVDF)	Study of RJS process	[66]
Polytetrafluoroethylene (PTFE)	Super-hydrophobic properties for anti-fouling applications	[70]
Polyacrylonitrile (PAN)	Carbon fibre precursor	[67, 145]
Poly(vinyl butyral) (PVB)	Study of RJS process	[84]
Polyvinylpyrrolidone (PVP)	Sacrificial polymer in fabrication of tin-doped indium oxide nanofibers	[62]
Polyvinylpyrrolidone (PVP) Polycaprolactone (PCL)	Biomedical applications, drug delivery vehicle	[68, 110]
Poly(L-lactic acid) (PLLA) Polyvinylpyrrolidone (PVP)	Biomedical, tissue engineering	[71]
Polyvinylchloride (PVC) Polyethylene glycol (PEG) Chitosan Gelatine Polyurethane (PU)	Study of RJS process	[146]
Polyamide 6 (PA6)	Study of RJS process	[147, 148]
Bacterial cellulose (BC)	Biomedical, tissue engineering	[149]
Polymethyl methacrylate (PMMA) Polyacrylonitrile (PAN)	Battery applications	[85, 138, 150]

Polystyrene (PS)	Composite reinforcement, refractory filtration systems, molecular anisotropy study	[81, 151]
Polystyrene (PS) Polycarbomethylsilane (PCmS)	Silicon carbide precursor	[152]
Thermoplastic polyurethane (TPU)	Switchable hydrophobicity applications for oil-water separation, graphene composite filler study	[141, 153]
Polyvinylpyrrolidone (PVP) SnCl4·5H2O	Gas sensing membranes	[154]
Polyvinyl alcohol (PVA) SnO2/PAN (Carbon)	Composite nanofibre for lithium-ion battery anodes	[155, 156]
Polyvinylpyrrolidone (PVP)	Electrostatic-assisted RJS process	[157]

In these studies, the fibres produced were evaluated in one of two ways. Firstly, in terms of the RJS process, and secondly in the specific capability towards an intended application. The results showed that application specific publications found favourable quantitative results based on initial objectives, while publications which focused more on the general process of RJS mainly focused on diameters or physical properties of fibres to further understand the RJS process. Several, more recent publications on RJS have continued to focus on processing and application specific research [15, 47, 104, 106, 138, 142, 158-167].

1.7.2 Melt spinning materials

Conversely to solution spinning and like electrospinning, RJS in the melt phase has not seen as much research due to the difficulty in processing fibres from the relatively viscous melt (see Table 1.4). There is unfortunately very little information on unpublished or failed experiments in RJS and thus on materials which did not work. As literature suggests, melt spinning would seem to be more limited in the materials choices facing it, with only a few materials available in the list below from published works:

Table 1.4: RJS (melt) materials choices from published data.

Polymer	**Application**	**Ref.**
Polypropylene (PP)	Study of RJS process, Hydrophilic nonwoven applications	[69, 74, 140]
Polybutylene terephthalate (PBT)	Study of RJS process	[65]
Polycaprolactone (PCL)	Biomedical applications	[76, 168]
Polyethylene terephthalate (PET) Polyvinylpyrrolidone (PVP)	Study of RJS process	[78]
Crystalline Olanzapine Crystalline Piroxicam Crystalline Sucrose	Biomedical applications (Drug delivery focus)	[109]

In the publications listed in Table 1.4, three were using RJS with a very specific application in mind, while the others were studies of the RJS process itself for specific polymers. These specific application focused studies were successfully able to use the RJS process for the creation of tissue scaffolds as well as drug delivery systems.

1.8 Processing and properties

The method by which RJS research has been conducted is all based on the same principle of a rotating spinneret (defined as an enclosed material container with multiple orifices) and some collection device – be that vertical collector bars, a solid cylindrical collector or a flat surface. In almost all reported cases, fibres are produced by altering the rotational velocity from 2,000 – 16,000 rpm, with some opting for higher rotational velocities due to smaller spinneret geometries where a similar centrifugal force would be required. Altering the processing parameters in RJS yields a variation in fibre diameter.

Processing variables within RJS include temperature, rotational velocity, collector distance, orifice diameter and spin duration. The spin duration mainly affects the volume of the fibres yielded but is nonetheless a basic parameter that is used in lab scale research. For continuous fibre production, it is only the other variables that need to be considered. Other parameters that affect fibre properties and diameters will be related to the polymer material itself, depending on whether it is spun from solution or melt. Considering the material’s spinnability, a certain upper (blockage) and lower (beading) limit for viscosity will exist for each combination of polymer solution concentration, or temperature for polymer melts. The flow behaviour such as Newtonian and non-Newtonian fluids are also expected to introduce a viscoelastic complexity to the prediction of polymers which will be suitable for RJS which is discussed in length in chapter 4.

Rotational velocity is what drives the RJS process, and increasing this will yield a greater centrifugal force with which to eject the polymer from the orifice. This basic premise of RJS is utilised by Mellado and coworkers in their equation derived for the critical rotational velocity threshold as given below [169].

$$\Omega_{th} = \sqrt{\frac{\sigma}{a^2 S_0 \rho}} \tag{1.1}$$

Equation 1.1 signifies that for a given polymer, each threshold will differ based on measurements of stress (σ), orifice diameter (a), distance from centreline to orifice opening (S_0) and density (ρ). With these measurements obtained beforehand, the theory predicts that a critical rotational velocity should be selected for a chosen polymer melt/solution. As mentioned, the viscoelasticity of the material affects the ability for a fibre to be spun.

To demonstrate this, a study by Shanmuganathan et al. has shown the variance in fibre diameter of polybutylene terephthalate (PBT) when altering the processing temperature [65]. Their data in Table 1.5 shows that for a rotational speed of 12,000 rpm, the fibre diameter changed from 1.64 μm at 280 °C to 1.17 μm at 320 °C. This shows that for PBT, an increase in processing temperature leads to thinner fibres. This will typically be the case for all polymers, as viscosity is reduced with temperature for thermoplastic polymers. It is worth noting that the viscosity of the polymer melt will have a great effect on spinnability, with low viscosity Newtonian fluids being the best contenders, as the standard systems are generally not pressure driven. (For pressure driven systems see pressure gyration publications [153, 170, 171])

Table 1.5: PBT fibre diameter variance with processing temperature, showing little variation with rotational velocity, but defined change from temperature effecting the polymer viscosity [65].

Rotational speed (rpm)	**Processing temperature (°C)**	**Average diameter (µm)**	**Std. deviation**	**Nanofibres (%)**
10,000	300	1.35	0.78	36
12,000	300	1.31	0.68	40
15,000	300	1.38	0.68	28
12,000	280	1.64	0.90	26
12,000	320	1.17	0.92	55

Solution spinning does not rely on elevated temperatures to reduce viscosity, as they are typically spun at room temperature. Instead of temperature, the reliance here will be on solution concentration and how it affects morphology of the fibres in the RJS process, as shown by Badrossamay et al. in Figure 1.13.

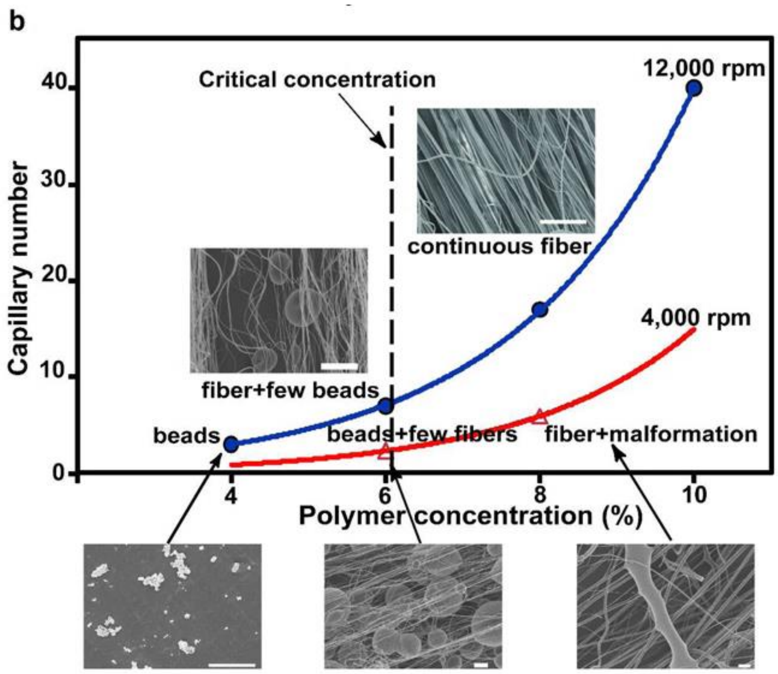

Figure 1.13: Nanofibre morphology reliance based on PLA concentration, showing that a critical concentration is needed to produce continuous bead-free fibres. Reproduced from Badrossamay et al. [61].

Their research demonstrates that jet break-up, and therefore fibre quality, may be estimated by the capillary number; defined as the ratio of the Weber number ($We = \frac{\rho U^2 D}{\gamma}$) to the Reynolds number ($Re = \frac{\rho U D}{\eta}$), which characterizes the ratio of the viscous force to surface tension force, where ρ is density, η is dynamic viscosity (which is directly related to the molecular weight and solution concentration), γ is surface tension of the polymer solution, U is the polymer jet exit speed based on a stationary frame and D is the orifice diameter. A lower capillary number results in shorter jet lengths and earlier jet break-up to isolated droplets. It therefore highlights the critical polymer concentration for this polymer type, to produce the best quality polylactic acid (PLA) fibres [61].

A study by Mohan et al. [151] has also investigated, in some detail, the ability of atactic-polystyrene (PS) to be melt spun by pressurized RJS. Here the authors were particularly interested in molecular anisotropy of RJS fibres as compared to electrospun fibres, with the highest level of anisotropy found in ES fibres. It was found that polymer solutions only yielded bead-free fibres between concentrations of 5-16 wt.%.

These types of analysis are a good methodology to employ for considering the types of polymers suitable for RJS, as this could potentially lead to further research whereby polymer properties can be used to approve or discard their ability to be spun without the time and effort expended on experimental testing.

1.8.1 Fibre diameters

Fibre diameter measurements are a common and effective characterisation method which is typically conducted using scanning electron microscopy (SEM) [71, 74, 145], optical microscopy (OM) [65] or transmission electron microscopy (TEM) [172] for imaging purposes.

The fibre diameters reported have several common influencing factors. Initial observations report a reduction in fibre diameter with an increase in rpm (therefore centrifugal force). In the case of PLA, increasing the rotation speed from 4,000 to 12,000 rpm resulted in a reduction in fibre diameter from 1143 (± 50) to 424 (± 41) nm

[61]. In the case of melt spinning, fibre diameters were also reduced with an increase in temperature as previously noted, due to the reduction in melt viscosity with elevated temperatures. Zander [76] shows in Table 1.6 that with increasing PCL melt temperature, the fibre diameter initially decreased before increasing at an even lower viscosity due to high temperatures and potential polymer degradation.

Table 1.6: PCL fibres produced by RJS, showing diameter reductions with increasing temperatures, before increasing diameter from high temperature processing [76].

Temperature (°C)	**Viscosity (Pa.s)**	**Fibre diameter (μm)**
120	158.1	9.7 ±4.9
140	130.4	8.8 ±3.1
200	43.3	7.0 ±1.1
250	17.8	12.8 ±8.4

The trend of decreasing and then increasing fibre diameter was also shown for an increase in rotational velocity by O'Haire et al. [74] in which they attempted to melt spin fibres from a melt blowing grade polypropylene (Lyondell MF650Y, MFI=1800 g dmin^{-1}) and a 1 wt.% concentration of multi walled carbon nanotube (MWCNT) dispersion.

Table 1.7: Melt processing effect on fibre diameter, showing the PP/MWCNT nanocomposite fibre variation in diameter with increasing spinneret speed [74].

Compound	**Spinneret speed (r.min^{-1})**	**Mean fibre diameter (μm)**	**Proportion of fibres < 1 μm (%)**	**Mean fibre diameter (nm)**	**Proportion of fibres > 5 μm (%)**
Pure PP	12,000	0.51	91.5	439	0
	13,000	0.63	88.3	502	0.7
PP/MWCNT	13,000	1.87	53.7	702	6.4
	14,000	1.05	56.7	633	0.6
	16,000	1.75	63.5	621	9.7

Reported in Table 1.7 is the proportion of fibres with a diameter greater than 5 μm. This is a phenomenon that appears to show up in RJS as a by-product from the start of the spinning cycle. By producing nanofibres from a PCL solution, measurements taken by McEachin et al. [63] at different interval times (5, 10, 15, 30 s) throughout the spinning cycle demonstrated this issue (see Figure 1.11). Explaining this phenomenon, the authors describe the effect of droplet elongation in the initial stages of fibre drawing from the orifice, in which the initial fibres that are collected have not had time to fully elongate or have sufficient solvent evaporation. This leads to an equilibrium diameter being reached somewhere after around 30 s in the spinning cycle at 6000 rpm as shown in Table 1.8. Due to this, many published mean fibre diameters from RJS will have artificially higher values due to the initial non-equilibrium state at start-up being included, and not accounted for.

Table 1.8: Average PCL fibre diameters of 16 wt.% polymer concentration solution RJS at 6000 rpm. Fibres collected after set intervals showing a reduction in the fibre diameter with time [63].

Sample	**Average diameter (μm)**
16 wt.% @ 5 s	2.10 ±1.00
16 wt.% @ 10 s	1.24 ±0.90
16 wt.% @ 15 s	0.51 ±0.26
16 wt.% @ 30 s	0.33 ±0.11

O'Haire et al. [74] corrects for this start-up phenomenon by allowing fibres that fall into this initial spin duration to be discounted from the values of the averages quoted by setting a size limit of 5 μm. Once these values are removed, a far more realistic mean value for the fibre diameter is obtained.

In research completed by Padron et al. [53], the fibre spinning process was filmed at a high frame rate, as shown in Figure 1.14, to view the polymer jet leaving the orifice. They investigated the effect of the angle of the orifice in comparison to the fibre diameters for a 6 wt.% polyethylene oxide (PEO) solution at 6000 rpm and concluded that the smallest diameter fibre was produced with a straight orifice, rather than 30° in the direction of rotation, or 89° against the direction of rotation.

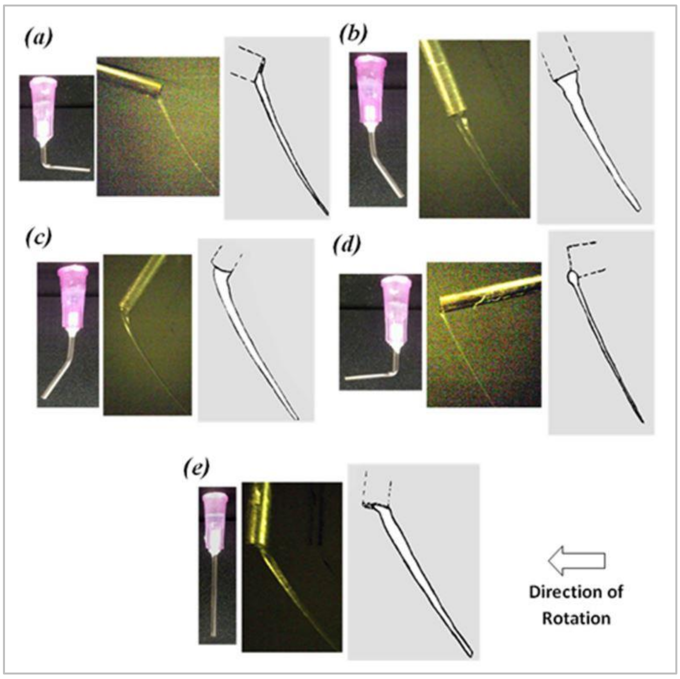

(a) curved opposite of rotation 89°

(b) curved opposite of rotation 30°

(c) curved direction of rotation 30°

(d) curved direction of rotation 89°

(e) straight needle

Figure 1.14: Analysis of the effect of orifice direction during spinning, showing that a straight needle (e) produced the smallest fibre diameter compared to other needle angles (a-d). Reproduced from Padron et al. [53].

Another influencing processing factor studied by Zander [76] illustrates the change in fibre diameter with collector distance variation. In his research, PCL fibres were collected at distances of 10, 12 and 14 cm from the orifice, producing fibres with diameters of 8.2±5.8, 8.3±4.4 and 7.0±1.1 μm, respectively. Although this small amount of data is not conclusive, it does indicate that there is indeed a variation of fibre diameter with collector distance.

1.8.2 Mechanical properties

Limited data is available in terms of mechanical properties of nanofibres produced by RJS, or nanofibres in general, due to the overall difficulty in testing individual nanofibres. Nanoscale mechanical testing requires extremely small loads for deformation, along with expert handling of the fibres due to their size. According to Tan et al. [173], the practicalities of testing individual nanofibres have the following five challenges: 1) Ability to manipulate extremely small fibres, 2) Finding a suitable mode of observation, 3) Sourcing of an accurate and sensitive force transducer, 4)

Sourcing of an accurate actuator with high resolution, and 5) Preparing samples of single-strand nanofibres.

The most common methods of nanofibre tensile testing include the use of atomic force microscope (AFM) cantilevers [174-176], 3-point bending testing [177-179] or commercial nano-tensile testing [38, 127]. The AFM testing method essentially relies on the fixing of a fibre to the end of a stationary point and the AFM cantilever, before applying a tensile load. The elastic modulus can then be measured using the force calculated from angle of deflection of the cantilever arm and the applied extension.

In another method, Wang et al. [177] performed a 3-point bending test, shown in Figure 1.15, on electrospun PVA/MWCNT composite nanofibres to establish mechanical properties. They used an AFM cantilever to perform the test to measure fibre deflection, from which they could calculate the Young's modulus. These are however all time-consuming methods which require a high degree of precision, coupled with the fact that it remains difficult to manipulate single fibres within these test rigs.

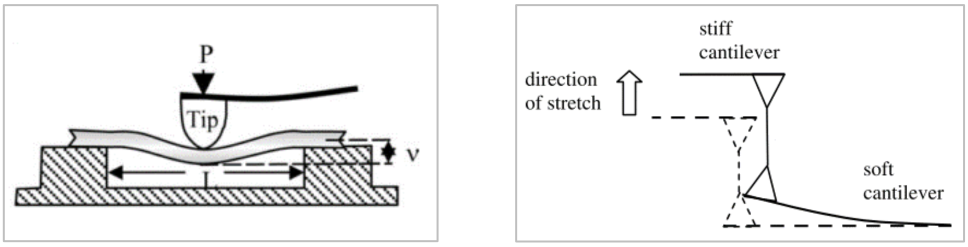

3-Point Bending Test

Cantilever Type Testing

Figure 1.15: Methods of mechanical testing on nanofibres using AFM cantilevers. Adapted from Tan et al. [173].

Tensile testing using commercially available equipment can be conducted by collecting aligned fibres on a ready-made frame, for use in a universal tensile testing machine. Electrospun PCL and PLA nanofibres have been successfully tested in this way [180]. A single PCL fibre that was used measured 1.4±0.3 μm, with a tensile modulus of 120±30 MPa and a tensile strength of 40±10 MPa being observed. This study also commented on the fact that there was no apparent correlation between Young's modulus and fibre diameter in these fibres. Although fibre modulus generally increases with decreasing fibre diameter, this effect is typically only observed for diameters below ~250 nm [126], which is much lower than the 1.4 µm fibre diameter tested by Tan et al. In Figure 1.16, by Arinstein et al. [181], it shows that a reduction in diameter of electrospun PA 6,6 fibres lead to a considerable increase in mechanical properties of these fibre due to improved molecular orientation and chain confinement.

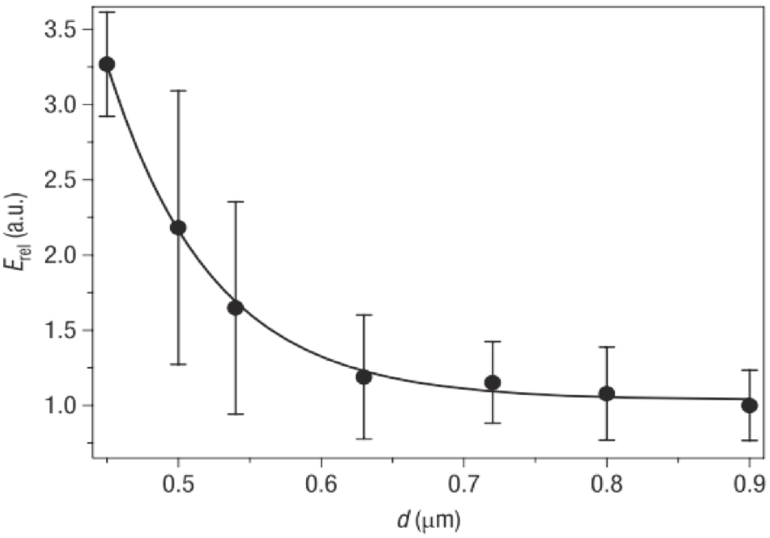

Figure 1.16: Relative Young's modulus of PA 6,6 fibres as a function of diameter. These results show a definite increase in mechanical properties with reducing fibre diameters. Reproduced from Arinstein et al. [181].

Another option available in testing nanofibres is to test a bundle of multiple fibres together in a micro tensile tester. Yao et al. [182] tested electrospun co-polyimide nanofibre bundles of 30 nanofibres and reported a Young's modulus of 38 GPa and tensile strength of 1.6 GPa. The bundle data was evaluated using Daniels' theory [183] based on Weibull statistics in order to estimate individual fibre strengths.

Figure 1.17 shows the testing procedure of a single nanofibre using the framing method as proposed by Chen et al. [184]. In their paper they discussed the mechanical properties of single electrospun polyimide nanofibres with a diameter of ~250 nm and reported a record high tensile modulus of 89 GPa.

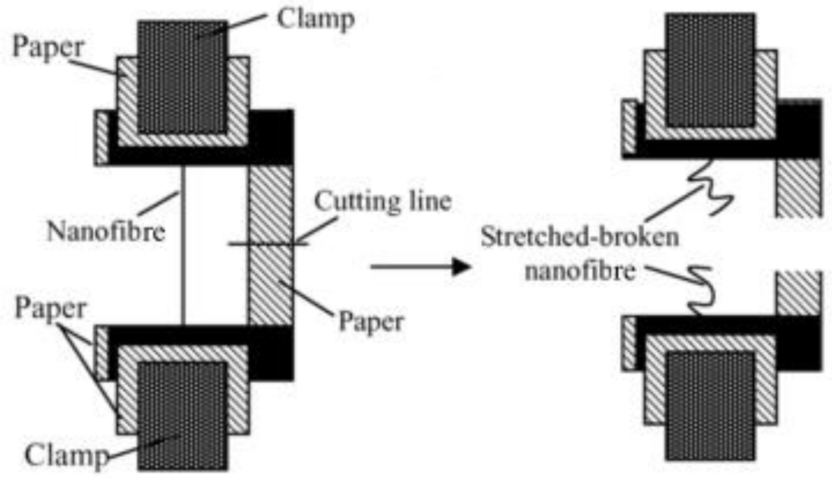

Figure 1.17: Tensile testing of a single polymer nanofibre using the paper frame method. Reproduced from Chen et al. [184].

In the case of RJS, only a handful of publications have considered the mechanical properties of the materials produced. In one of these publications, PTFE nanofibre yarns were tested. The polymer solution was prepared by dissolving the PTFE in Fluorinert FC-40, before being rotary jet spinning and subsequently collected for assembly as yarns. Tensile testing of these twisted yarns produced a modulus of 348 MPa [70].

As briefly mentioned, RJS research has so far not been able to develop a deposition methodology that allows for fibre alignment in a similar way as the rotating drum or disc method does in electrospinning. By collecting oriented fibres, it would ensure more accurate mechanical testing data using the frame method (see Figure 1.17). Upson et al. however used this method to test a nanofibre web produced by RJS, aligning the testing frame (and thereby the tensile testing direction) with the spinning direction of the fibres [164].

Simplified methods of testing mechanical properties of polymer nanofibers are essential for future developments, although existing methods do provide some data which allows us to compare mechanical properties of nanofibre yarns [185], bundles, and in rare occasions even single polymer nanofibres.

1.9 Modelling the rotary jet spinning process

With any of the material's processing techniques available, modelling has a lot to offer to further refine and optimize the process. Knowledge that is gained from modelling is used to improve and understand the process in more detail, which is sometimes simply not possible through experimental techniques alone. Modelling the RJS process involves the use of basic parameters such as polymer viscosity, centrifugal force, Coriolis force, air drag on the fibre and also the evaporation time of a solvent in the collector during spinning [53]. Several publications investigating viscoelastic properties and production methods [163, 186-191] provide great insight into the complexity of the RJS process and will provide useful directions for future RJS models.

Models which focus on electrospinning which have recently been published [49, 192] include additional variables to RJS modelling such as the volumetric charge density and electrical potential during processing. One property which is obviously absent in electrospinning models are rotational velocities, but in many of these electrospinning models there is good agreement between predicted fibre morphology and that obtained through experimentation.

Figure 1.18 shows a basic representation of the forces involved in the RJS process in agreement with assumptions made by Mellado et al. [169].

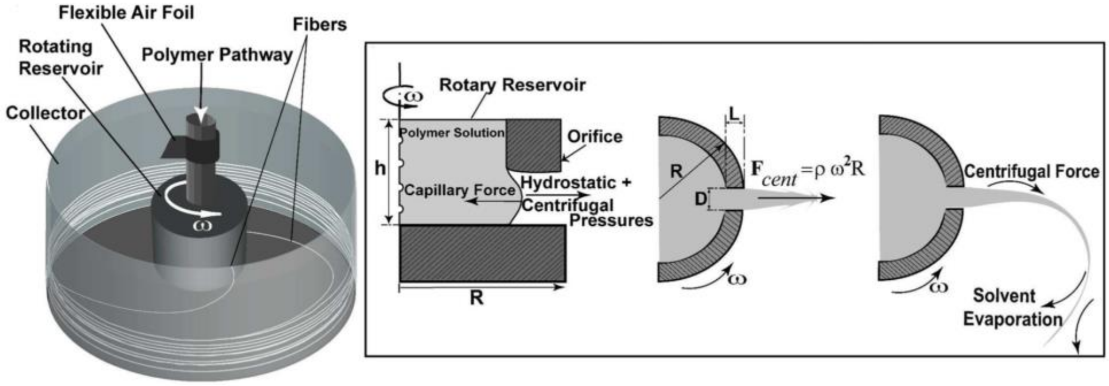

Figure 1.18: Schematic of RJS process and the relevant physics as produced by Badrossomay et al. [61].

There have been one-dimensional (1D) studies that have investigated related parameters such a spiralling slender jets emerging from a rapidly rotating orifice in both a viscous model by Decent et al. [186] and an inviscid model by Wallwork et al. [193]. This research, and other related studies have set the initial basis for RJS models.

Valipouri et al. [83, 194] performed experiments using both air-sealed (isolated) and open air (non-isolated) flow RJS setups to evaluate the prediction from a numerical model. The reason for this is due to the complexity of the addition of air resistance to the model once the system accounts for drag forces on the drawing fibre as it spins.

Based on co-ordinate systems from Wallwork et al. [193] and Decent et al. [186], Valipouri et al. [83] established a model to evaluate the process. The main forces considered were centrifugal, Coriolis and viscous forces in a comparison between isolated and non-isolated models.

The model outcome, shown in Figure 1.19, could accurately predict the experimental trajectory profiles for the isolated jets based on simulations, but was not able to accurately predict the trajectories of the non-isolated flow experiments, when using water as a test fluid.

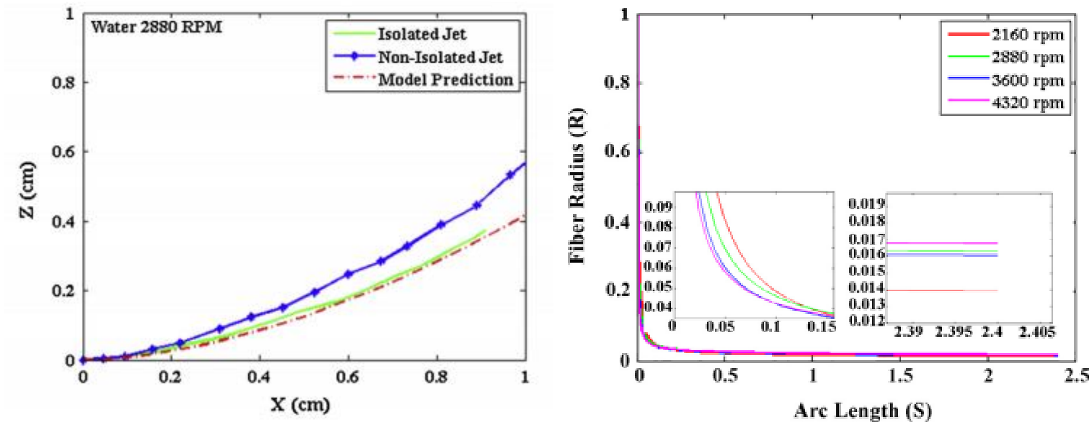

(a) (b)

Figure 1.19: Experimental vs. model behaviour of (a) H20 and (b) polyacrylonitrile (PAN). The prediction of trajectory shows the isolated jet having good fit with the model, and the non-isolated jet with poor fit. Fibre radius predictions of PAN using a dimensionless value over the arc length show good correlation with measured experimental diameters, predicting only very small variances with rotational velocity. Reproduced from Valipouri et al [83].

The conclusion that Valipouri et al. reached was that an increase in trajectory curvature was found in the non-isolated open-air system due to the increase in air resistance/turbulence within the spinning area. Fibre diameters of polyacrylonitrile (PAN) were also measured and compared with a simulation derived value, showing a correlation based on rotational velocity variation.

In a separate publication by Valipouri et al. [194] regarding the numerical study of RJS and the effect of angular velocity, they investigated the influence of non-dimensional numbers such as the Rossby number on fibre diameter. Here it was concluded that a decrease in Rossby number (which in real terms indicates an increase in angular velocity) reduces the size of the fibre diameter, contracts the trajectory, and increases the tangential velocity. This further enhances the experimental proof of reduced fibre diameter with increasing angular velocity, of which some qualitative agreement with experimental data has been established.

When investigating a new technique and possible ways to numerically evaluate its behaviour, it may be possible to arrive at the same conclusions from different models, thus confirming each other's findings.

To this end, Mellado et al. [169] produced what they called "A simple model for nanofibre formation by rotary jet spinning". In it, they establish three key moments in the lifecycle of nanofibre formation, namely 1) jet initiation, 2) jet elongation and 3) solvent evaporation. It is in these three areas that experimental and theoretical studies produce a phase diagram, which can with some certainty predict the production rates and quality of fibres as shown in Figure 1.20.

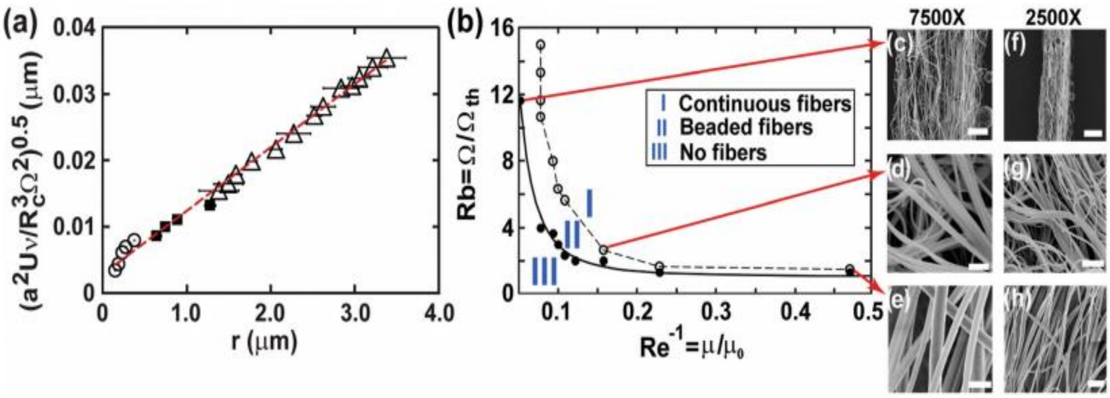

Figure 1.20: Diagrams illustrating fibre radius prediction by Mellado and co-workers [169], showing (a) fibre radius measurements based on processing parameters, (b) a phase diagram which divides the scaled angular velocity-viscosity planes into regimes I, II, III, (c, f) beaded fibres, (d, g) continuous fibres and (e, h) large continuous fibres collected from regime I. Scale bars are 4 μm (c)-(e) and 20 μm (f)-(h).

The final fibre radius and threshold rotational velocity for fibre production are calculated using equations 1.2 and 1.3, as proposed by Mellado et al. [169]:

$$r \sim \frac{aU^{0.5}\upsilon^{0.5}}{R_c^{3/2}\Omega} \tag{1.2}$$

where r is radius of fibre, a is orifice diameter, U is exit velocity of polymer, ν is kinematic viscosity defined at viscosity/density, R_c is radius to collector and Ω is rotational velocity.

$$\Omega_c \sim \frac{\rho R_c^2 \sigma^2}{a^2}\eta^{-3} \tag{1.3}$$

where Ωc is critical rotational velocity, ϱ is density, R_c is radius to collector, σ is surface tension, a is orifice diameter and η is viscosity.

This study highlighted the fact that the formation of fibres using RJS is influenced by a few key factors. The tuning of fibre radii is essentially controlled by varying viscosity, angular velocity (which directly affects the polymer exit velocity), distance to the collector and the radius of the orifice, which are all shown to be parameters in the model prediction for fibre radius.

While studying the interaction of the RJS process with various material property variations, Badrossamay et al. [61] experimented with polymer concentrations in solution as a benchmark for fibre quality. In their publication, they reviewed the effect of a change in polymer concentration on molecular chain entanglement, and the critical concentration (C*) at which the presence of a sufficient amount of entanglements dramatically alters the viscoelastic properties of the spinning solution to facilitate fibres of a higher quality (those without beading).

As with RJS, electrospinning also relies on chain entanglements. A detailed study by Shenoy et al. [195] has shown this to be the case for several polymer/solvent systems in which distinct zones are present. The divide these zones into 1) good fibre formation, 2) fibre and bead formation, or 3) beads or droplets only. In their research, Shenoy et al. calculated that for stable fibre formation to occur, a minimum of 2.5 entanglements per chain should exist.

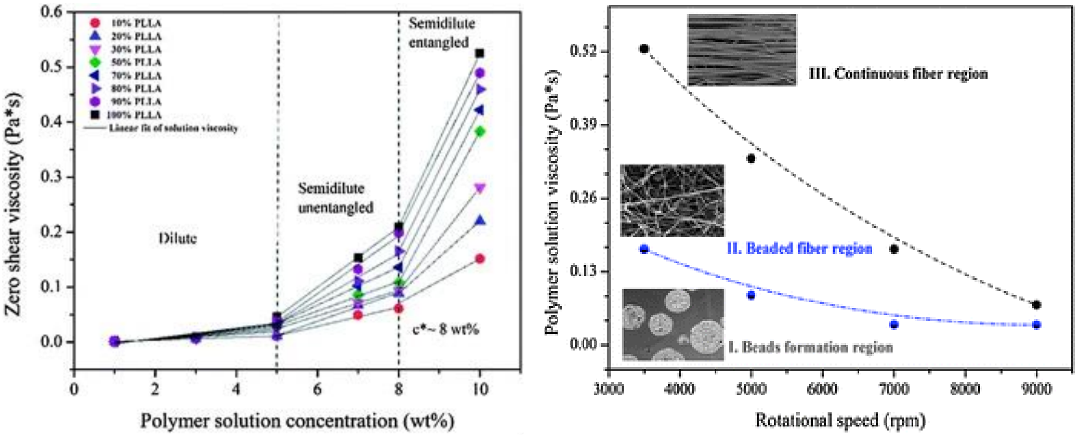

(a) (b)

Figure 1.21: Zero shear viscosity versus polymer solution concentration for polyvinyl pyrrolidone/poly(L-lactic acid) (PVP/PLLA) blends with (a) varying PLLA content and (b) PVP/PLLA fibre quality, showing how the critical entanglement ratio affects the quality of the fibre throughout all spinning speeds. Reproduced from Ren et al. [71].

A polyvinylpyrrolidone (PVP) / poly(L-lactic acid) (PLLA) and dichloromethane (DCM) solution was chosen to evaluate the critical concentration phenomenon, with polymer concentrations ranging from 0.1 wt.% – 10 wt.%. In Figure 1.21, the gradient change of the zero shear viscosity versus polymer concentration signifies the alteration in molecular entanglements. There are usually three distinct regimes observed in these graphs, indicating a step change in the overlapping of polymer chains from a dilute, semi-dilute disentangled state to a semi-dilute entangled state. These gradients can vary depending on the different chain lengths, chain configurations, polydispersity and molecular weight of the PLLA and PVP in this study [71].

It is typical in non-branched linear polymer melts for the zero shear viscosity to scale with the molecular weight to the power of ~3.4 above the critical entanglement molecular weight, M_e [196], however polymer solutions can deviate slightly from this gradient [197] above the critical concentration, C*.

It is this overlapping of polymer chains, with increasing polymer concentration, which results in a critical concentration being reached. In the case of RJS of PLA/chloroform, C* is 8 wt.%. At this concentration, there are enough chain entanglements to create rheological behaviour that can produce bead-free fibres at sufficient rotational velocities. As shown in Figure 1.13, the critical concentration may indicate when a polymer solution is likely to produce a good quality fibre, but the angular velocity must still be sufficient to expel the polymer and overcome the surface tension in the drawn fibre so as not to induce malformations such as beading.

As with previous modelling examples in RJS, non-dimensional numbers are often the key to understanding the limitations of the process. In Badrossamay et al.'s evaluation of them [61], the Capillary number (defined as the ratio of the Weber number to the Reynolds number) indicates whether a fibre would be of better quality by possessing a higher value. They state that the Capillary number could estimate jet break-up, whereby lower Capillary numbers result in shorter jet lengths and earlier jet break-up to isolated droplets [61, 198].

A two-dimensional (2D) inviscid model for RJS focuses on determining the fibre radius and trajectories as a function of arc length and was produced by Padron et al. [199]. This model is geared towards predicting final fibre diameters, with the hope of reducing experimental time and material waste. To do this, the parameters studied included angular velocity, material properties, collector diameter, orifice size and solvent evaporation rate. This model is however 2D which assumes that the gravitational forces are much smaller than the centrifugal forces produced in the system.

Non-dimensional numbers provide ratios between various forces in the system being studied. Padron et al. [64] reviews some of the most important ones in Table 1.9 below:

Table 1.9: List and definitions of non-dimensional numbers used for the prediction of general fluid behaviour. Adapted from Padron et al. [64].

Dimensionless number	**Ratio description**
Reynolds number	Inertial forces to viscous forces
Froude number	Fibre's inertial force to gravitational force
Weber number	Fibre's inertial force to surface tension
Rossby number	Fibre's inertial force to Coriolis force
Deborah number	Polymer relaxation time to flow
Capillary number	Fibre's viscous forces to surface tension

Padron et al. produced comparable solutions to those of Wallwork et al. [193] where the trajectory and diameters of beads formed using the prilling process were studied. This process is similar to RJS and based on viscous material ejected from a rotating surface, typically used to create pellets from materials heated to low viscosity melting points such as fertilizers or detergent powders [200]. The steady state solutions that were obtained were then used to compare similarly derived equations for time-dependant parameters with constant angular velocity, transforming the equations into partial differential equations.

Padron et al.'s work clearly displays an ability to model and predict the variation in fibre diameter along its axis with respect to time, including information on the trajectory of such fibres. However, their work does not include a viscous element, and could therefore be misleading when comparing with experimental data. However, with a viscoelastic component included in such a model, a powerful prediction tool would become available.

Such a model was presented in a further publication by Padron et al. [53] in which they study the fibre forming process from a material property point of view, along with high speed photography to capture the physics of the jet as it leaves the orifice. This work once again summarised the importance of all the processing parameters including the rheological properties, viscosity and relaxation time of the polymeric material. As discussed by Padron et al. [53], it is important to consider the large deformations that are present in the RJS process, and to choose appropriate viscoelastic models which will be able to approximate the solution or material properties such as a Pipkin diagram [201] in Figure 1.22, which separates a materials' viscoelastic properties into regimes based on their dynamic response.

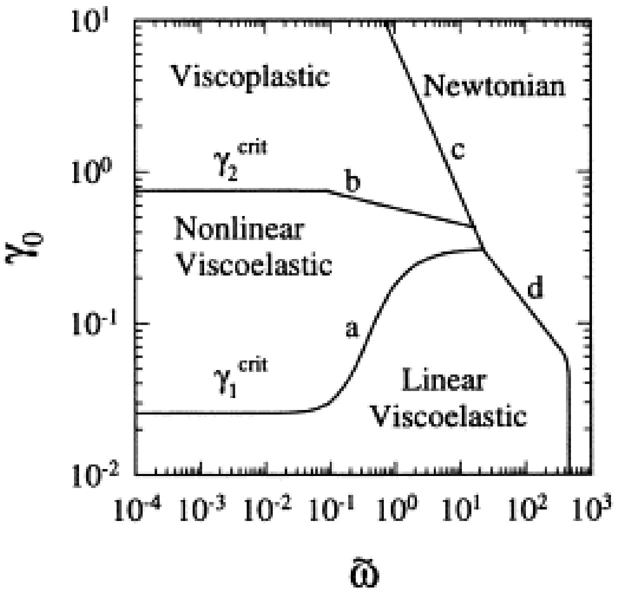

Figure 1.22: Pipkin diagram showing demarcated areas of viscoelastic behaviour, evaluating strain amplitude (γ_0) versus dimensionless frequency ($\tilde{\omega}$) in a study of alumina and silicone oil suspensions, where $\tilde{\omega} = \omega/E_0^2$ (E_0 being electric field strength). Reproduced from Parthasarathy et al. [202].

In their research, Padron et al. define RJS falling into the non-linear viscoelastic regime in Figure 1.22. It goes on to define the coordinate system using a rotating reference, and the governing equations used are described by the continuity equation:

$$\nabla \cdot \boldsymbol{u} = 0 \tag{1.4}$$

where u is the relative velocity of the fibre jet; and the Cauchy momentum equations:

$$\frac{\partial \boldsymbol{u}}{\partial t} + (\boldsymbol{u} \cdot \nabla)\boldsymbol{u} = -\frac{\nabla P}{\rho} + \boldsymbol{g} + \frac{\nabla \boldsymbol{T}}{\rho} - \boldsymbol{\omega} \times (\boldsymbol{\omega} \times \mathbf{r}) - 2\boldsymbol{\omega} \times \boldsymbol{u} \tag{1.5}$$

Where P is the pressure, g is the gravity vector, T is the stress tensor, ω is the angular velocity of the spinneret, and r is a position vector describing a point along the fibre.

Exit velocities for both continuous and non-continuously fed spinnerets are calculated using the parameters from Figure 1.23 below:

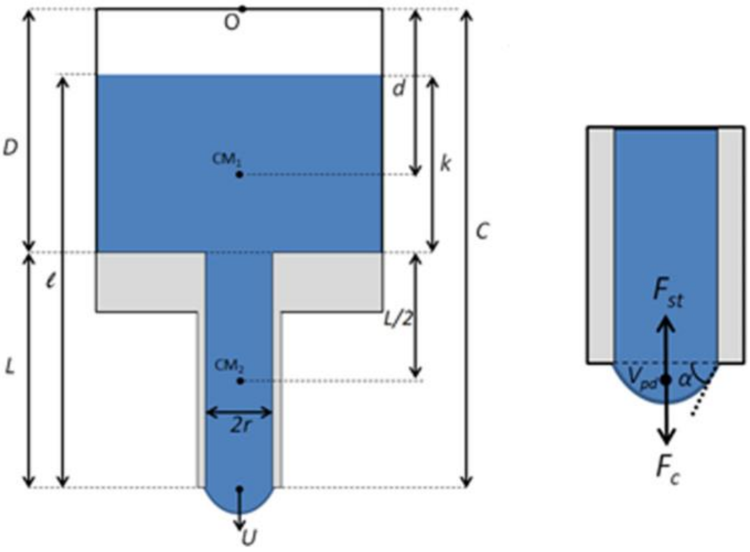

Figure 1.23: Representation of the forces on the polymeric fluid within the RJS geometry. Reproduced from Padron et al. [53].

Based on these calculations for velocity U, the critical angular velocity Ω_{cr} and critical exit velocity U_{cr} of the system were established in equation 6:

$$\Omega_{cr} = \sqrt{\frac{2\pi r\sigma \sin\alpha}{\rho V_{pd} C}} \tag{1.6}$$

$$U_{cr} = -\frac{8L\mu}{\rho r^2} + \frac{1}{2}\sqrt{256\left(\frac{L\mu}{\rho r^2}\right)^2 + \frac{8\pi r\sigma \sin\alpha}{\rho V_{pd} C}\left[D^2 + 2L\left(C - \frac{L}{2}\right)\right]} \tag{1.7}$$

where ρ is density, V_{pd} is volume of the pendant drop and μ is viscosity.

High speed imagery was used to establish the shape of the pendant drop (Figure 1.24) as it approaches the critical velocity threshold, which results in fibre jet initiation. After this point, when the fibre has commenced its extension, the velocity of the jet increases due to the simultaneous pushing and pulling momentum from both sides of the capillary. This velocity is expressed in an equation by Padron et al. [53] by adding an additional term U_f (fibre velocity) into equation 7.

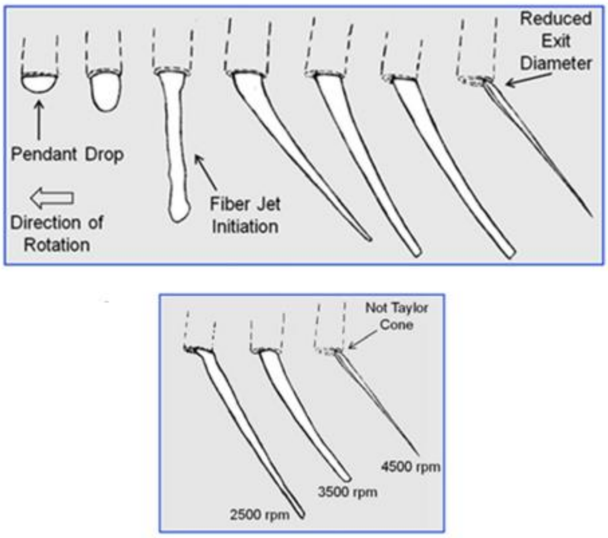

Figure 1.24: Evolution of fibre jet at increasing rotational velocities, showing the change from pendant drop to fully drawn fibre producing flow. Reproduced from Padron et al. [53].

Padron et al. [53] also experimented by varying both angular velocities and solution viscosity, and were able to establish a model of trajectories along the X and Z axis as seen in Figure 1.25.

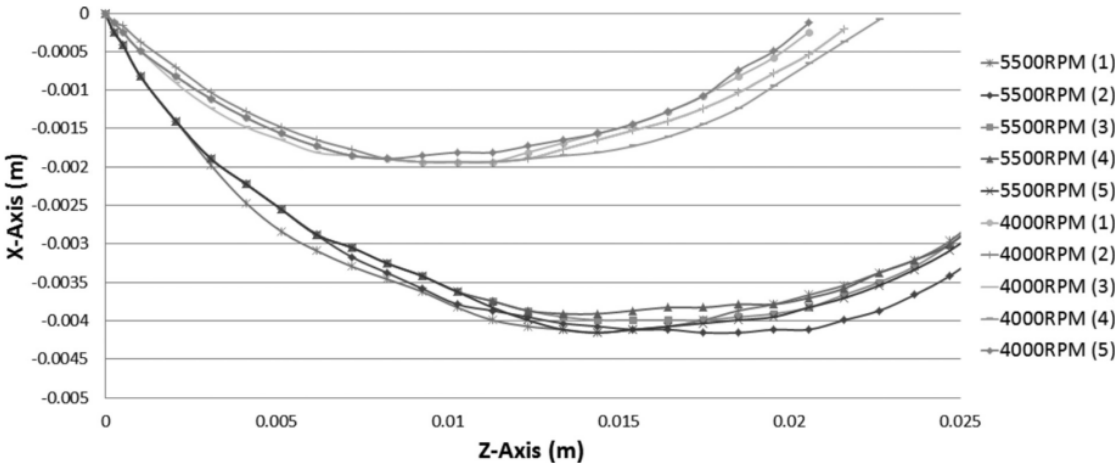

Figure 1.25: Variance of fibre trajectories under same conditions, showing effect of viscosity on fibre trajectory. 6 wt.% PEO solutions were used at two velocities to obtain trajectory data, where it was shown that higher rotational velocities ensured a tighter trajectory. Reproduced from Padron et al. [53].

Being able to accurately predict the final radius and trajectory for the RJS process is important in the long term as industrial applications for nanofibres become more refined. When the basic morphology can be predicted to a reasonably acceptable accuracy, the process will become more commercially viable. The current data available to achieve this would suggest that it is approaching the point to which this could be possible.

1.10 Adaptations within rotary jet spinning

As RJS is still a relatively new technique for manufacturing polymer nanofibres, there are different approaches in the design and construction of the equipment used. These variations are often based on a few key parameters which alter the spinneret size, collector distance and rotational velocity, with some changing the number of jet orifices and locations. Equation 8 shows the calculation variables used for centrifugal force, demonstrating that an equivalent force can be obtained by either altering the rotational velocity (ω), mass (M), or by altering the distance from the axes of rotation (r). In this equation, rotational velocity is the most sensitive parameter.

$$F_c = M\omega^2 r \tag{1.8}$$

Commercial versions of RJS hardware are available to purchase from companies such as FibeRio® Technology Co. in Texas, USA, and around a third of publications have used their flagship L-1000D Cyclone Forcespinning™ system to conduct research into nanofibre production. Alternatively, an extremely simple setup could involve nothing more than an inverted motor with a polymer vessel acting as a spinneret, surrounded by a collection device. In essence, a very simple setup - not very different from a candy floss machine - should you wish to conduct research on varying dimensional scales other than that which is available commercially. However, accuracy and repeatability would rely on the quality of equipment being used with safety being another key consideration.

Other adaptations of the process by which to make fibres through centrifugal force have involved experiments using nozzle-free approaches, such as the one used by Weitz et al. [203] in their study of poly(methyl methacrylate) (PMMA) solution behaviour on the surface of a spin coater. They successfully established a procedure to create discontinuous fibres ranging from 25 nm to 5 μm in diameter.

Methods that incorporate electrospinning, together with an element of RJS, have also been investigated. Angammana et al. [204] considered a charged rotary atomiser disc with polymer solution that would effectively eject fibres from the top of the rotational arc towards a charged collector plate above, resulting in nanofibre production. A similar technique was introduced by Chang et al. [205], where they combined electrospinning with RJS and termed it electrostatic-centrifugal spinning, with the view of removing the whipping instability experienced by electrospinning alone. It is said to be first introduced by their lab, and they investigated the effects on a viscoelastic jet and a single nanofibre through this technique. Much emphasis was placed on the viscoelastic behaviour of the jets. Badrossomay et al. [128], Ericksson et al. [129] and Wang et al. [110] have also produced good fibre alignment by combining both RJS and electrospinning, a feat which has not been achieved without this combination.

The benefit of the combined rotary jet and electrospinning system is to ensure that fibre alignment is maximised. If the fibre is moving towards the collector in electrospinning, a whipping motion is experienced, creating a non-oriented mat on the collector. By introducing RJS to this process, it greatly increases alignment, much in the same way that a rotating disc collector in electrospinning ensures fibre alignment on collection.

Pressure can also be used as an added element to improve RJS. If the spinneret is enclosed and pressurized, an additional force is introduced. This is exactly what Edirisinghe and co-workers did when spinning several materials from solution under a pressure of up to 300 kPa and 36,000 rpm, being the capability of their in-house built system [153, 165, 168, 170, 171, 206-210]. The benefits of this system include the use of a wider range of polymer viscosities due to added pressure forcing flow through the spinneret dies, rather than relying purely on centrifugal force generated by the rotation velocity. This system does not however produce fibres consistently in the nanoscale.

1.11 The future of rotary jet spinning

Rotary Jet Spinning has become prevalent in the last decade, with research related to this topic increasing exponentially since its inception. At present, the commercialisation of this technology for the non-woven industry is starting, with the introduction of larger industrial scale RJS machines capable of spinning one-meter wide continuous fibre mats. Other methods of nanofibre production such as needless electrospinning also offer large scale production, such as the Nanospider™ technology by Elmarco [7], as referenced previously. However, with up-scaled nanofibre production, it is only a matter of time until RJS starts to compete with other more established methods of polymer nanofibre production such as melt blowing, where unaligned non-woven mats and spunbound materials are made.

Due to the lower production costs and potentially greener credentials, a lower price to market should be achievable which could make this a potentially disruptive technology in the nanofibre race. However, it remains to be seen whether a broad range of materials will be considered for diverse applications, or if more traditional polymeric materials such as polypropylenes, polyamides or polyesters will take on specific product applications. Since biomedicine is a large contributor to the research bulk to date, it is possible that pharmaceutical/biomedical interests may become the lead user of this technology for the development of tissue recovery and/or drug delivery systems. Other applications at the forefront of this technology will be in fibre based electronic devices like flexible sensors, super capacitors or lithium ion batteries.

As with most technology, the more that is understood about the ability to manipulate a certain production method, the more attractive it is for investment within them. The current body of knowledge available on RJS would suggest that we can expect a step change to occur well within the next decade.

References

1. Yarin, A.L., B. Pourdeyhimi, and S. Ramakrishna, *Fundamentals and Applications of Micro and Nanofibers*. 2014: Cambridge University Press.
2. Bhardwaj, N. and S.C. Kundu, *Electrospinning: a fascinating fiber fabrication technique.* Biotechnol Adv, 2010. **28**(3): p. 325-47.
3. Graham, K., et al. *Polymeric Nanofibers in Air Filtration Applications*. in *Fifteenth Annual Technical Conference & Expo of the American Filtration & Separation Society*. 2002.
4. Paul, D.R. and L.M. Robeson, *Polymer nanotechnology: Nanocomposites*, in *Polymer*. 2008. p. 3187-3204.
5. Wichmann, M.H.G., K. Schulte, and H.D. Wagner, *On nanocomposite toughness.* Composites Science and Technology, 2008. **68**(1): p. 329-331.
6. Greenfeld, I. and H.D. Wagner, *Nanocomposite toughness, strength and stiffness: role of filler geometry.* 2015.
7. Elmarco.com. *Elmarco - Nano for Life*. 2015 [cited 2015 08/09/2015]; Available from: http://www.elmarco.com/gallery/nanofibers/.
8. Yao, J., C.W.M. Bastiaansen, and T. Peijs, *High Strength and High Modulus Electrospun Nanofibers.* Fibers, 2014. **2**(2): p. 158-186.
9. Huang, Z.-M., et al., *A review on polymer nanofibers by electrospinning and their applications in nanocomposites.* Composites Science and Technology, 2003. **63**(15): p. 2223-2253.
10. Greiner, A. and J.H. Wendorff, *Electrospinning: a fascinating method for the preparation of ultrathin fibers.* Angew Chem Int Ed Engl, 2007. **46**(30): p. 5670-703.
11. Shambaugh, R.L., *A Macroscopic View of the Melt-Blowing Process for Producing Microfibers.* Industrial & Engineering Chemistry Research, 1988. **27**(12): p. 2363-2372.
12. Han, W., G.S. Bhat, and X. Wang, *Investigation of Nanofiber Breakup in the Melt-Blowing Process.* Industrial & Engineering Chemistry Research, 2016. **55**(11): p. 3150-3156.
13. Durany, A., N. Anantharamaiah, and B. Pourdeyhimi, *Micro and nanofiber nonwovens produced by means of fibrillating/fracturing islands-in-the-sea fibers.* Journal of Engineered Fibers and Fabrics, 2008. **3**(3).
14. Anantharamaiah, N., S. Verenich, and B. Pourdeyhimi, *Durable Nonwoven Fabrics via Fracturing Bicomponent Islands-in-the-Sea Filaments.* Journal of Engineered Fibers and Fabrics, 2016. **3**(3): p. 1-9.
15. Zhang, Z., et al., *Fabrication and properties of poly(tetrafluoroethylene) nanofibres via sea-island spinning.* Polymer, 2017. **109**: p. 321-331.
16. Schönenberger, C., et al., *Template Synthesis of Nanowires in Porous Polycarbonate Membranes: Electrochemistry and Morphology.* The Journal of Physical Chemistry B, 1997. **101**(28): p. 5497-5505.
17. Lozano, K. and K. Sarkar, *Superfine fiber creating spinneret and uses thereof.* 2012. p. 1-20.

18. Zhang, X. and Y. Lu, *Centrifugal Spinning: An Alternative Approach to Fabricate Nanofibers at High Speed and Low Cost*. Polymer Reviews, 2014. **54**(4): p. 677-701.
19. Peno, E. and R. Lipton, *Apparatuses and methods for the simultaneous production of microfibers and nanofibers*. 2014, Fiberio Technology Corporation.
20. Peno, E. and R. Lipton, *Devices and methods for the production of coaxial microfibers and nanofibers*. 2014, FibeRio Technologies Corporation.
21. Peno, E., R. Lipton, and S. Kay, *Apparatuses having outlet elements and methods for the production of microfibers and nanofibers*. 2014, Fiberio Technology Corporation: US.
22. Peno, E., R. Lipton, and S. Kay, *Apparatuses and methods for the deposition of microfibers and nanofibers on a substrate*. 2014, Fiberio Technology Corporation.
23. Peno, E., R. Lipton, and S. Kay, *Multilayer apparatuses and methods for the production of microfibers and nanofibers*. 2014, Fiberio Technology Corporation.
24. Peno, E., R. Lipton, and S. Kay, *Split fiber producing devices and methods for the production of microfibers and nanofibers*. 2014, Fiberio Technology Corporation.
25. Peno, E., R. Lipton, and S. Kay, *Systems and methods for the production of microfibers and nanofibers using a fluid level sensor*. 2014, Fiberio Technology Corporation.
26. *European Patent Office*. [cited 2015 23 September]; Available from: http://www.epo.org/.
27. Ondarçuhu, T. and C. Joachim, *Drawing a single nanofibre over hundreds of microns.* Europhysics Letters (EPL), 1998. **42**(2): p. 215-220.
28. McDaniel, P.B., J.M. Deitzel, and J.W. Gillespie, *Structural Hierarchy and Surface Morphology of Highly Drawn Ultra High Molecular Weight Polyethylene Fibers Studied by Atomic Force Microscopy and Wide Angle X-Ray Diffraction.* Polymer, 2015.
29. Feng, L., et al., *Super-hydrophobic surface of aligned polyacrylonitrile nanofibers.* Angew Chem Int Ed Engl, 2002. **41**(7): p. 1221-3.
30. Wang, J. and D. Zhang, *One-Dimensional Nanostructured Polyaniline: Syntheses, Morphology Controlling, Formation Mechanisms, New Features, and Applications.* Advances in Polymer Technology, 2013. **32**(S1): p. E323-E368.
31. Ma, P.X. and R. Zhang, *Synthetic nano-scale fibrous extracellular matrix.* J Biomed Mater Res, 1999. **46**(1): p. 60-72.
32. Whitesides, G.M. and B. Grzybowski, *Self-assembly at all scales.* Science, 2002. **295**(5564): p. 2418-21.
33. Hartgerink, J.D., E. Beniash, and S.I. Stupp, *Self-assembly and mineralization of peptide-amphiphile nanofibers.* Science, 2001. **294**(5547): p. 1684-1688.
34. Zhang, S., *Fabrication of novel biomaterials through molecular self-assembly.* Nature Biotechnology, 2003. **21**(10): p. 1171-1178.
35. Fedorova, N. and B. Pourdeyhimi, *High strength nylon micro- and nanofiber based nonwovens via spunbonding.* Journal of Applied Polymer Science, 2007. **104**(5): p. 3434-3442.
36. Li, W.J., et al., *Electrospun nanofibrous structure: a novel scaffold for tissue engineering.* J Biomed Mater Res, 2002. **60**(4): p. 613-21.

37. Araujo, T.M., et al., *Electrospinning of a blend of a liquid crystalline polymer with poly(ethylene oxide): Vectran nanofiber mats and their mechanical properties.* J. Mater. Chem. C, 2013. **1**(2): p. 351-358.
38. Yao, J., et al., *Electrospinning of p-Aramid Fibers.* Macromolecular Materials and Engineering, 2015: p. n/a-n/a.
39. Bognitzki, M., et al., *Nanostructured fibers via electrospinning.* Advanced Materials, 2001. **13**(1): p. 70-+.
40. Li, D. and Y. Xia, *Fabrication of titania nanofibers by electrospinning.* Nano Letters, 2003. **3**(4): p. 555-560.
41. Yoshimoto, H., et al., *A biodegradable nanofiber scaffold by electrospinning and its potential for bone tissue engineering.* Biomaterials, 2003. **24**(12): p. 2077-82.
42. Ellison, C.J., et al., *Melt blown nanofibers: Fiber diameter distributions and onset of fiber breakup.* Polymer, 2007. **48**(11): p. 3306-3316.
43. Moreno, M.J., et al., *Development of a compliant and cytocompatible micro-fibrous polyethylene terephthalate vascular scaffold.* Journal of Biomedical Materials Research Part B-Applied Biomaterials, 2011. **97B**(2): p. 201-214.
44. Bresee, R.R. and W.-C. Ko, *Fiber formation during melt blowing.* Int. Nonwovens J, 2003. **12**(2): p. 21-28.
45. Nayak, R., et al., *Recent advances in nanofibre fabrication techniques.* Textile Research Journal, 2011. **82**: p. 129-147.
46. Zhou, H., T.B. Green, and Y.L. Joo, *The thermal effects on electrospinning of polylactic acid melts.* Polymer, 2006. **47**(21): p. 7497-7505.
47. Yu, M., et al., *Recent Advances in Needleless Electrospinning of Ultrathin Fibers: From Academia to Industrial Production.* Macromolecular Materials and Engineering, 2017: p. 1700002.
48. Brown, T.D., P.D. Dalton, and D.W. Hutmacher, *Melt electrospinning today: An opportune time for an emerging polymer process.* Progress in Polymer Science, 2016.
49. Stepanyan, R.R., et al., *Nanofiber diameter in electrospinning of polymer solutions: Model and experiment.* Polymer, 2016. **97**: p. 428-439.
50. Luo, C.J., et al., *Electrospinning versus fibre production methods: from specifics to technological convergence.* Chem Soc Rev, 2012. **41**(13): p. 4708-35.
51. Rutledge, G.C. and S.V. Fridrikh, *Formation of fibers by electrospinning.* Adv Drug Deliv Rev, 2007. **59**(14): p. 1384-91.
52. Son, W.K., et al., *The effects of solution properties and polyelectrolyte on electrospinning of ultrafine poly(ethylene oxide) fibers.* Polymer, 2004. **45**(9): p. 2959-2966.
53. Padron, S., et al., *Experimental study of nanofiber production through forcespinning.* Journal of Applied Physics, 2013. **113**(2): p. 9.
54. Hiremath, N. and G.S. Bhat, *Meltblown Polymeric Nanofibres for Medical Applications- An Overview.* Nanoscience Technology, 2015. **2**(1): p. 1-9.
55. Wang, D., G. Sun, and B.-S. Chiou, *A High-Throughput, Controllable, and Environmentally Benign Fabrication Process of Thermoplastic Nanofibers.* Macromolecular Materials and Engineering, 2007. **292**(4): p. 407-414.
56. *Fiber Engine FX series systems from FibeRio*. 2014 29/06/2017]; Available from: http://www.filtsep.com/view/40670/fiber-engine-fx-series-systems-from-fiberio/.

57. *Nanofiber production line NS 8S1600U*. 2017 29/06/2017]; Available from: http://www.elmarco.com/nanofiber-equipment/nanofiber-production-lines-ns8s1600u/.

58. *Equipment NW-101 MECC CO. LTD.* 2017 29/06/2017]; Available from: http://www.mecc-nano.com/equipment01.html.

59. *Industrial Electrospinning nanofiber machine | Inovenso, innovative engineering solutions*. 2017 29/06/2017]; Available from: http://inovenso.com/portfolio-view/nanospinner416/.

60. *SPIN Line by SPUR*. 2017 29/06/2017].

61. Badrossamay, M.R., et al., *Nanofiber assembly by rotary jet-spinning.* Nano Lett, 2010. **10**(6): p. 2257-61.

62. Altecor, A., Y. Mao, and K. Lozano, *Large-Scale Synthesis of Tin-Doped Indium Oxide Nanofibers Using Water as Solvent.* Functional Materials Letters, 2012. **05**(03): p. 1250020.

63. McEachin, Z. and K. Lozano, *Production and characterization of polycaprolactone nanofibers via forcespinning (TM) technology.* Journal of Applied Polymer Science, 2012. **126**(2): p. 473-479.

64. Padron, S., et al., *Production and characterization of hybrid BEH-PPV/PEO conjugated polymer nanofibers by forcespinning (TM).* Journal of Applied Polymer Science, 2012. **125**(5): p. 3610-3616.

65. Shanmuganathan, K., et al., *Solventless High Throughput Manufacturing of Poly(butylene terephthalate) Nanofibers.* Acs Macro Letters, 2012. **1**(8): p. 960-964.

66. Vazquez, B., H. Vasquez, and K. Lozano, *Preparation and characterization of polyvinylidene fluoride nanofibrous membranes by forcespinning (TM).* Polymer Engineering and Science, 2012. **52**(10): p. 2260-2265.

67. Lu, Y., et al., *Parameter study and characterization for polyacrylonitrile nanofibers fabricated via centrifugal spinning process.* European Polymer Journal, 2013. **49**(12): p. 3834-3845.

68. Amalorpava Mary, L., et al., *Centrifugal spun ultrafine fibrous web as a potential drug delivery vehicle.* Express Polymer Letters, 2013. **7**(3): p. 238-248.

69. Raghavan, B., H. Soto, and K. Lozano, *Fabrication of Melt Spun Polypropylene Nanofibers by Forcespinning.* Journal of Engineered Fibers and Fabrics, 2013. **8**(1): p. 52-60.

70. Rane, Y., et al., *Preparation of Superhydrophobic Teflon (R) AF 1600 Sub-Micron Fibers and Yarns Using the Forcespinning (TM) Technique.* Journal of Engineered Fibers and Fabrics, 2013. **8**(4): p. 88-95.

71. Ren, L., et al., *Large-scale and highly efficient synthesis of micro- and nano-fibers with controlled fiber morphology by centrifugal jet spinning for tissue regeneration.* Nanoscale, 2013. **5**(6): p. 2337-45.

72. Sebe, I., et al., *Polymer structure and antimicrobial activity of polyvinylpyrrolidone-based iodine nanofibers prepared with high-speed rotary spinning technique.* International Journal of Pharmaceutics, 2013. **458**(1): p. 99-103.

73. Golecki, H.M., et al., *Effect of Solvent Evaporation on Fiber Morphology in Rotary Jet Spinning.* Langmuir, 2014. **30**(44): p. 13369-13374.

74. O'Haire, T., et al., *Influence of nanotube dispersion and spinning conditions on nanofibre nanocomposites of polypropylene and multi-walled carbon nanotubes*

produced through Forcespinning (TM). Journal of Thermoplastic Composite Materials, 2014. **27**(2): p. 205-214.

75. Weng, B., et al., *Mass production of carbon nanotube reinforced poly(methyl methacrylate) nonwoven nanofiber mats.* Carbon, 2014. **75**: p. 217-226.
76. Zander, N.E., *Formation of melt and solution spun polycaprolactone fibers by centrifugal spinning.* Journal of Applied Polymer Science, 2015. **132**(2): p. 9.
77. Agubra, V.A., et al., *ForceSpinning of polyacrylonitrile for mass production of lithium-ion battery separators.* Journal of Applied Polymer Science, 2016. **133**(1): p. n/a-n/a.
78. Chen, H., et al., *Effective method for high-throughput manufacturing of ultrafine fibres via needleless centrifugal spinning.* Micro & Nano Letters, 2015. **10**(2): p. 81-84.
79. Krifa, M. and W. Yuan, *Morphology and pore size distribution of electrospun and centrifugal forcespun nylon 6 nanofiber membranes.* Textile Research Journal, 2015. **86**(12): p. 1294-1306.
80. Li, X., H. Chen, and B. Yang, *Centrifugally spun starch-based fibers from amylopectin rich starches.* Carbohydrate Polymers, 2015.
81. Salinas, A., M. Lizcano, and K. Lozano, *Synthesis of Beta-SiC Fine Fibers by the Forcespinning Method with Microwave Irradiation.* Journal of Ceramics, 2015. **2015**: p. 5.
82. Schabikowski, M., et al., *Rotary jet-spinning of hematite fibers.* Textile Research Journal, 2015. **85**(3): p. 316-324.
83. Valipouri, A., et al., *Experimental and numerical study on isolated and non-isolated jet behavior through centrifuge spinning system.* International Journal of Multiphase Flow, 2015. **69**: p. 93-101.
84. Weng, B., et al., *The production of carbon nanotube reinforced poly(vinyl) butyral nanofibers by the Forcespinning® method.* Polymer Engineering & Science, 2015. **55**(1): p. 81-87.
85. Yanilmaz, M. and X. Zhang, *Polymethylmethacrylate/Polyacrylonitrile Membranes via Centrifugal Spinning as Separator in Li-Ion Batteries.* Polymers, 2015. **7**(4): p. 629-643.
86. Liu, H.A., et al., *Electrospinning of poly(alkoxyphenylenevinylene) and methanofullerene nanofiber blends.* ACS Appl Mater Interfaces, 2009. **1**(9): p. 1958-65.
87. Tsou, S.-Y., et al., *Rheological aspect on electrospinning of polyamide 6 solutions.* European Polymer Journal, 2013. **49**(11): p. 3619-3629.
88. Smit, E., U. Buttner, and R.D. Sanderson, *Continuous yarns from electrospun fibers.* Polymer, 2005. **46**(8): p. 2419-2423.
89. Cozza, E.S., et al., *Nanostructured nanofibers based on PBT and POSS: Effect of POSS on the alignment and macromolecular orientation of the nanofibers.* European Polymer Journal, 2013. **49**(1): p. 33-40.
90. Ma, Z., et al., *Surface engineering of electrospun polyethylene terephthalate (PET) nanofibers towards development of a new material for blood vessel engineering.* Biomaterials, 2005. **26**(15): p. 2527-36.
91. Vaz, C.M., et al., *Design of scaffolds for blood vessel tissue engineering using a multi-layering electrospinning technique.* Acta Biomater, 2005. **1**(5): p. 575-82.

92. Yang, F., et al., *Electrospinning of nano/micro scale poly(L-lactic acid) aligned fibers and their potential in neural tissue engineering.* Biomaterials, 2005. **26**(15): p. 2603-10.
93. Bai, H., et al., *Composite nanofibers of conducting polymers and hydrophobic insulating polymers: Preparation and sensing applications.* Polymer, 2009. **50**(14): p. 3292-3301.
94. Cho, D., et al., *Structural properties and superhydrophobicity of electrospun polypropylene fibers from solution and melt.* Polymer, 2010. **51**(25): p. 6005-6012.
95. Aussawasathien, D., J. Dong, and L. Dai, *Electrospun polymer nanofiber sensors.* Synthetic Metals, 2005. **154**(1-3): p. 37-40.
96. Chen, L.-J., et al., *Synthesis and characterization of PVB/silica nanofibers by electrospinning process.* Polymer, 2009. **50**(15): p. 3516-3521.
97. *Nanofiber Market - Industry Trends And Analysis, Market Report - Technavio*. 2017, Technavio.
98. Pelipenko, J., P. Kocbek, and J. Kristl, *Critical attributes of nanofibers: preparation, drug loading, and tissue regeneration.* Int J Pharm, 2015. **484**(1-2): p. 57-74.
99. Langer, R. and J.P. Vacanti, *Tissue engineering.* Science, 1993. **260**(5110): p. 920-6.
100. Agarwal, S., J.H. Wendorff, and A. Greiner, *Progress in the field of electrospinning for tissue engineering applications.* Adv Mater, 2009. **21**(32-33): p. 3343-51.
101. Nagarajan, L. and N. Gayathri, *Production of Nanofibres using Rotary Jet Spinning Method for Tissue Engineering.* International Journal of Science and Research, 2016.
102. Zhang, X., et al., *Polymer-polymer composites for the design of strong and tough degradable biomaterials.* Materials Today Communications, 2016. **8**: p. 53-63.
103. Cai, L. and S.C. Heilshorn, *Designing ECM-mimetic materials using protein engineering.* Acta Biomater, 2014. **10**(4): p. 1751-60.
104. Buzgo, M., et al., *Emulsion centrifugal spinning for production of 3D drug releasing nanofibres with core/shell structure.* RSC Adv., 2017. **7**(3): p. 1215-1228.
105. Barnes, C.P., et al., *Nanofiber technology: designing the next generation of tissue engineering scaffolds.* Adv Drug Deliv Rev, 2007. **59**(14): p. 1413-33.
106. Rampichova, M., et al., *Platelet-functionalized three-dimensional poly-epsilon-caprolactone fibrous scaffold prepared using centrifugal spinning for delivery of growth factors.* Int J Nanomedicine, 2017. **12**: p. 347-361.
107. Zhu, J., J. Yang, and G. Sun, *Cibacron Blue F3GA functionalized poly(vinyl alcohol-co-ethylene) (PVA-co-PE) nanofibrous membranes as high efficient affinity adsorption materials.* Journal of Membrane Science, 2011. **385-386**: p. 269-276.
108. Ma, J., et al., *Biodegradable fibre scaffolds incorporating water-soluble drugs and proteins.* J Mater Sci Mater Med, 2015. **26**(7): p. 205.
109. Marano, S., et al., *Development of Micro-Fibrous Solid Dispersions of Poorly Water-Soluble Drugs in Sucrose using Temperature-Controlled Centrifugal Spinning.* Eur J Pharm Biopharm, 2016.
110. Wang, L., et al., *Mass and controlled fabrication of aligned PVP fibers for matrix type antibiotic drug delivery systems.* Chemical Engineering Journal, 2016. **307**: p. 661-669.

111. Mehetre, G., V. Pande, and P. Kendre, *An Overview of nanofibers as a Platform for Drug Delivery.* NDDS, 2015. **2015**(3).
112. Stachewicz, U., et al., *Manufacture of Void-Free Electrospun Polymer Nanofiber Composites with Optimized Mechanical Properties.* ACS Appl Mater Interfaces, 2012. **4**(5): p. 2577-82.
113. Zhang, H., et al., *Localized toughening of carbon/epoxy laminates using dissolvable thermoplastic interleaves and electrospun fibres.* Composites Part a-Applied Science and Manufacturing, 2015. **79**: p. 116-126.
114. Zhang, H., et al. *Damage sensing in fibre-reinforced composites using carbon nanotube networks by spray coating*. in *ECCM 2012 - Composites at Venice, Proceedings of the 15th European Conference on Composite Materials*. 2012.
115. Chen, Q., et al., *Nano-epoxy resins containing electrospun carbon nanofibers and the resulting hybrid multi-scale composites.* Composites Part B-Engineering, 2014. **58**: p. 43-53.
116. Tanami, G.A., E. Wachtel, and G. Marom, *Crystalline structure and thermodynamic analysis of ultra-low diameter VGCF-polypropylene nanocomposite monofilaments.* Polymer Composites, 2016. **37**(6): p. 1641-1649.
117. Choi, Y.K., et al., *Mechanical and physical properties of epoxy composites reinforced by vapor grown carbon nanofibers.* Carbon, 2005. **43**(10): p. 2199-2208.
118. Eichhorn, S.J., et al., *Review: current international research into cellulose nanofibres and nanocomposites.* Journal of Materials Science, 2009. **45**(1): p. 1-33.
119. Al-Saleh, M.H. and U. Sundararaj, *A review of vapor grown carbon nanofiber/polymer conductive composites.* Carbon, 2009. **47**(1): p. 2-22.
120. Hussain, F., et al., *Review article: Polymer-matrix nanocomposites, processing, manufacturing, and application: An overview.* Journal of Composite Materials, 2006. **40**(17): p. 1511-1575.
121. Peijs, T., *Electrospun Polymer Nanofibers and their Composites*, in *Comprehensive Composite Materials II*, C.H. Zweben and P.W.R. Beaumont, Editors. 2018, Elsevier Ltd. p. 162-200.
122. Chen, Q., et al., *Preparation and evaluation of nano-epoxy composite resins containing electrospun glass nanofibers.* Journal of Applied Polymer Science, 2012. **124**(1): p. 444-451.
123. Bafekrpour, E., et al., *Functionally graded carbon nanofiber/phenolic nanocomposites and their mechanical properties.* Composites Part A: Applied Science and Manufacturing, 2013. **54**: p. 124-134.
124. Kai, D., et al., *Mechanical properties and in vitro behavior of nanofiber–hydrogel composites for tissue engineering applications.* Nanotechnology, 2012. **23**(9): p. 095705.
125. Daelemans, L., et al., *Damage-Resistant Composites Using Electrospun Nanofibers: A Multiscale Analysis of the Toughening Mechanisms.* ACS Appl Mater Interfaces, 2016. **8**(18): p. 11806-18.
126. Papkov, D., et al., *Simultaneously strong and tough ultrafine continuous nanofibers.* ACS Nano, 2013. **7**(4): p. 3324-31.
127. Yao, J., et al., *High performance co-polyimide nanofiber reinforced composites.* Polymer, 2015. **76**: p. 46-51.
128. Badrossamay, M.R., et al., *Engineering hybrid polymer-protein super-aligned nanofibers via rotary jet spinning.* Biomaterials, 2014. **35**(10): p. 3188-3197.

129. Erickson, A.E., et al., *High-throughput and high-yield fabrication of uniaxially-aligned chitosan-based nanofibers by centrifugal electrospinning.* Carbohydrate Polymers, 2015. **134**: p. 467-474.
130. Sutherland, K., *Filters and Filtration Handbook*. Fifth ed. 2008, Oxford, UK: Elsevier.
131. Yoon, K., B.S. Hsiao, and B. Chu, *Functional nanofibers for environmental applications.* Journal of Materials Chemistry, 2008. **18**(44): p. 5326-5334.
132. Ahn, Y.C., et al., *Development of high efficiency nanofilters made of nanofibers.* Current Applied Physics, 2006. **6**(6): p. 1030-1035.
133. Podgorski, A., A. Balazy, and L. Gradon, *Application of nanofibers to improve the filtration efficiency of the most penetrating aerosol particles in fibrous filters.* Chemical Engineering Science, 2006. **61**(20): p. 6804-6815.
134. Virji, S., et al., *Polyaniline Nanofiber Gas Sensors: Examination of Response Mechanisms.* Nano Letters, 2004. **4**(3): p. 491-496.
135. Berson, S., et al., *Poly (3-hexylthiophene) fibers for photovoltaic applications.* Advanced Functional Materials, 2007. **17**(8): p. 1377-1384.
136. Wu, Q., et al., *Supercapacitors Based on Flexible Graphene/Polyaniline Nanofiber Composite Films.* Acs Nano, 2010. **4**(4): p. 1963-1970.
137. Zhang, K., et al., *Graphene/Polyaniline Nanofiber Composites as Supercapacitor Electrodes.* Chemistry of Materials, 2010. **22**(4): p. 1392-1401.
138. Agubra, V.A., et al., *A comparative study on the performance of binary SnO2/NiO/C and Sn/C composite nanofibers as alternative anode materials for lithium ion batteries.* Electrochimica Acta, 2017. **224**: p. 608-621.
139. Tsuchida, H., et al., *Radiation-induced colour changes in a spiropyran/BaFCl:Eu2+/polystyrene composite film and nonwoven fabric.* New J. Chem., 2016.
140. Liang, C., et al., *Hydrophilic nonwovens by Forcespinning™ of isotactic polypropylene blended with amphiphilic surfactants.* Fibers and Polymers, 2016. **17**(10): p. 1646-1656.
141. Ou, R., et al., *Robust Thermoresponsive Polymer Composite Membrane with Switchable Superhydrophilicity and Superhydrophobicity for Efficient Oil-Water Separation.* Environ Sci Technol, 2016.
142. Dotto, G.L., et al., *Chitosan/polyamide nanofibers prepared by Forcespinning® technology: A new adsorbent to remove anionic dyes from aqueous solutions.* Journal of Cleaner Production, 2017. **144**: p. 120-129.
143. Ramakrishna, S., et al., *Electrospun nanofibers: solving global issues.* Materials Today, 2006. **9**(3): p. 40-50.
144. Obregon, N., et al., *Effect of Polymer Concentration, Rotational Speed, and Solvent Mixture on Fiber Formation Using Forcespinning®.* Fibers, 2016. **4**(2): p. 20.
145. Weng, B., F. Xu, and K. Lozano, *Mass production of carbon nanotube-reinforced polyacrylonitrile fine composite fibers.* Journal of Applied Polymer Science, 2014. **131**(11): p. n/a-n/a.
146. Mîndru, T.B., et al., *Morphological aspects of polymer fiber mats obtained by air flow rotary-jet spinning.* Fibers and Polymers, 2013. **14**(9): p. 1526-1534.
147. Hammami, M.A., M. Krifa, and O. Harzallah, *Centrifugal force spinning of PA6 nanofibers – processability and morphology of solution-spun fibers.* The Journal of The Textile Institute, 2014. **105**(6): p. 637-647.

148. Krifa, M., M.A. Hammami, and H. Wu, *Occurrence and morphology of bead-on-string structures in centrifugal forcespun PA6 fibers.* Journal of the Textile Institute, 2015. **106**(3): p. 284-294.
149. Khan, S., et al., *Engineered regenerated bacterial cellulose scaffolds for application in in vitro tissue regeneration.* RSC Adv., 2015.
150. Agubra, V.A., et al., *Forcespinning: A new method for the mass production of Sn/C composite nanofiber anodes for lithium ion batteries.* Solid State Ionics, 2016. **286**: p. 72-82.
151. Mohan, S.D., G.R. Mitchell, and F.J. Davis, *Development of Molecular Anisotropy in Centrifugally Spun Fibers as Compared to Electrospun Fibers.* Macromolecular Materials and Engineering, 2016. **301**(11): p. 1313-1319.
152. Salinas, A., et al., *Production of beta-Silicon Carbide Nanofibers using the Forcespinning (R) Method.* Journal of Ceramic Science and Technology, 2016. **7**(3): p. 229-234.
153. Amir, A., et al., *Graphene nanoplatelets loaded polyurethane and phenolic resin fibres by combination of pressure and gyration.* Composites Science and Technology, 2016. **129**: p. 173-182.
154. Xu, W., et al., *Preparation and low-temperature gas-sensing properties of SnO2 ultra-fine fibers fabricated by a centrifugal spinning process.* Journal of Sol-Gel Science and Technology, 2016.
155. Nava, R., et al., *Centrifugal spinning: an alternative for large scale production of Silicon-Carbon composite nanofibers for lithium ion batteries anodes.* ACS Appl Mater Interfaces, 2016.
156. Agubra, V., et al., *Forcespinning of Microfibers and their Applications in Lithium-Ion and Sodium-Ion Batteries.* ECS Transactions, 2016. **72**(8): p. 57-65.
157. Chen, H., et al., *Electrostatic-assisted centrifugal spinning for continuous collection of submicron fibers.* Textile Research Journal, 2016.
158. Hou, T., et al., *Highly porous fibers prepared by centrifugal spinning.* Materials & Design, 2017. **114**: p. 303-311.
159. Deravi, L.F., et al., *Design and Fabrication of Fibrous Nanomaterials Using Pull Spinning.* Macromolecular Materials and Engineering, 2017: p. 1600404.
160. Dinkgreve, M., M.M. Denn, and D. Bonn, *"Everything flows?": elastic effects on startup flows of yield-stress fluids.* Rheologica Acta, 2017.
161. Dassios, K., *Modification of Carbon Fibre/Epoxy composites by polyvinylalcohol(PVA) based Electrospun Nanofibres.* Advanced Composite Letters, 2017.
162. van der Heijden, S., et al., *Novel composite materials with tunable delamination resistance using functionalizable electrospun SBS fibers.* Composite Structures, 2017. **159**: p. 12-20.
163. Riahi, D.N., *Modeling and computation of nonlinear rotating polymeric jets during forcespinning process.* International Journal of Non-Linear Mechanics, 2017. **92**: p. 1-7.
164. Upson, S.J., et al., *Centrifugally spun PHBV micro and nanofibres.* Materials Science and Engineering: C, 2017. **76**: p. 190-195.
165. Hong, X., S. Mahalingam, and M. Edirisinghe, *Simultaneous Application of Pressure-Infusion-Gyration to Generate Polymeric Nanofibers.* Macromolecular Materials and Engineering, 2017: p. 1600564.

166. Lin, X., et al., *Large scale fabrication of magnesium oxide fibers for high temperature thermal structure applications.* Ceramics International, 2016.
167. Zhang, Q., et al., *Advanced Fabrication of Chemically Bonded Graphene/TiO2 Continuous Fibers with Enhanced Broadband Photocatalytic Properties and Involved Mechanisms Exploration.* Sci Rep, 2016. **6**: p. 38066.
168. Xu, Z., et al., *Making Nonwoven Fibrous Poly(ε-caprolactone) Constructs for Antimicrobial and Tissue Engineering Applications by Pressurized Melt Gyration.* Macromolecular Materials and Engineering, 2016.
169. Mellado, P., et al., *A simple model for nanofiber formation by rotary jet-spinning.* Applied Physics Letters, 2011. **99**(20): p. 203107.
170. Mahalingam, S. and M. Edirisinghe, *Forming of polymer nanofibers by a pressurised gyration process.* Macromol Rapid Commun, 2013. **34**(14): p. 1134-9.
171. Mahalingam, S., G. Ren, and M. Edirisinghe, *Rheology and pressurised gyration of starch and starch-loaded poly(ethylene oxide).* Carbohydr Polym, 2014. **114**: p. 279-87.
172. Feng, C., et al., *Preparation, ferromagnetic and photocatalytic performance of NiO and hollow Co3O4 fibers through centrifugal-spinning technique.* Materials Research Bulletin, 2015.
173. Tan, E.P.S. and C.T. Lim, *Mechanical characterization of nanofibers - A review.* Composites Science and Technology, 2006. **66**(9): p. 1102-1111.
174. Tan, E., et al., *Tensile test of a single nanofiber using an atomic force microscope tip.* Applied Physics Letters, 2005. **86**(7): p. 073115.
175. Hang, F., et al., *In situ tensile testing of nanofibers by combining atomic force microscopy and scanning electron microscopy.* Nanotechnology, 2011. **22**(36): p. 365708.
176. Liu, L.-Q., et al., *Tensile Mechanics of Electrospun Multiwalled Nanotube/Poly(methyl methacrylate) Nanofibers.* Advanced Materials, 2007. **19**(9): p. 1228-1233.
177. Wang, W., et al., *Effective reinforcement in carbon nanotube-polymer composites.* Philos Trans A Math Phys Eng Sci, 2008. **366**(1870): p. 1613-26.
178. Hwang, K.Y., et al., *Mechanical characterization of nanofibers using a nanomanipulator and atomic force microscope cantilever in a scanning electron microscope.* Polymer Testing, 2010. **29**: p. 375-380.
179. Baker, S.R., et al., *Determining the mechanical properties of electrospun poly-ε-caprolactone (PCL) nanofibers using AFM and a novel fiber anchoring technique.* Materials Science and Engineering: C, 2016. **59**: p. 203-212.
180. Tan, E., S. Ng, and C. Lim, *Tensile testing of a single ultrafine polymeric fiber.* Biomaterials, 2005. **26**: p. 1453-6.
181. Arinstein, A., et al., *Effect of supramolecular structure on polymer nanofibre elasticity.* Nat Nanotechnol, 2007. **2**(1): p. 59-62.
182. Yao, J., et al., *High-performance electrospun co-polyimide nanofibers.* Polymer, 2015.
183. Daniels, H.E., *The Statistical Theory of the Strength of Bundles of Threads. I.* 1945.
184. Chen, F., et al., *Mechanical characterization of single high-strength electrospun polyimide nanofibres.* Journal of Physics D: Applied Physics, 2008. **41**(2): p. 025308.

185. Zhou, Y., et al., *Strip twisted electrospun nanofiber yarns: Structural effects on tensile properties.* Journal of Materials Research, 2012. **27**(03): p. 537-544.
186. Decent, S.P., et al., *The trajectory and stability of a spiralling liquid jet: Viscous theory.* Applied Mathematical Modelling, 2009. **33**(12): p. 4283-4302.
187. Părău, E.I., et al., *Nonlinear viscous liquid jets from a rotating orifice.* Journal of Engineering Mathematics, 2006. **57**(2): p. 159-179.
188. McKinley, G.H., *Visco-Elasto-Capillary Thinning and Break-up of Complex Fluids.* 2005.
189. McKinley, G.H. and T. Sridhar, *Filament-Stretching Rheometry of Complex Fluids.* Annual Review of Fluid Mechanics, 2002. **34**(1): p. 375-415.
190. Tirtaatmadja, V., G.H. McKinley, and J.J. Cooper-White, *Drop formation and breakup of low viscosity elastic fluids: Effects of molecular weight and concentration.* Physics of Fluids, 2006. **18**(4): p. 043101.
191. Wagner, C., L. Bourouiba, and G.H. McKinley, *An analytic solution for capillary thinning and breakup of FENE-P fluids.* Journal of Non-Newtonian Fluid Mechanics, 2015. **218**: p. 53-61.
192. Thompson, C.J., et al., *Effects of parameters on nanofiber diameter determined from electrospinning model.* Polymer, 2007. **48**(23): p. 6913-6922.
193. Wallwork, I.M., et al., *The trajectory and stability of a spiralling liquid jet. Part 1. Inviscid theory.* Journal of Fluid Mechanics, 2002. **459**: p. 43-65.
194. Valipouri, A., et al., *Numerical Study on the Jet Dynamic through Centrifuge Spinning : Influence of Angular Velocity.* Journal of Textiles and Polymers, 2015. **3**: p. 20-25.
195. Shenoy, S.L., et al., *Role of chain entanglements on fiber formation during electrospinning of polymer solutions: good solvent, non-specific polymer–polymer interaction limit.* Polymer, 2005. **46**(10): p. 3372-3384.
196. Colby, R.H., L.J. Fetters, and W.W. Graessley, *The melt viscosity-molecular weight relationship for linear polymers.* Macromolecules, 1987. **20**(9): p. 2226-2237.
197. Thomas, D.K. and T.A.J. Thomas, *Viscosity–concentration relationships in solutions of high polymers.* Journal of Applied Polymer Science, 1960. **3**(8): p. 129-131.
198. Oliveira, M.S.N., R. Yeh, and G.H. McKinley, *Iterated stretching, extensional rheology and formation of beads-on-a-string structures in polymer solutions.* Journal of Non-Newtonian Fluid Mechanics, 2006. **137**(1-3): p. 137-148.
199. Padron, S., D.I. Caruntu, and K. Lozano, *On 2d Forcespinning (Tm) Modeling.* Proceedings of the Asme International Mechanical Engineering Congress and Exposition, 2011, Vol 7, Pts A and B, 2012: p. 821-830.
200. Gowariker, V., et al., *The Fertilizer Encyclopedia*. 2008.
201. Pipkin, A.C., *Lectures on Viscoelasticity Theory*. 1986: Springer New York.
202. Parthasarathy, M. and D.J. Klingenberg, *Large amplitude oscillatory shear of ER suspensions.* Journal of Non-Newtonian Fluid Mechanics, 1999. **81**(1-2): p. 83-104.
203. Weitz, R.T., et al., *Polymer nanofibers via nozzle-free centrifugal spinning.* Nano Letters, 2008. **8**(4): p. 1187-1191.

204. Angammana, C. and S. Jayaram. *A study of free surface electrospinning process to enhance and optimize the nanofibre production*. in *Proceedings of the 2012 Electrostatics Joint Conference June. S*. 2012.
205. Chang, W.-M., C.-C. Wang, and C.-Y. Chen, *The combination of electrospinning and forcespinning: Effects on a viscoelastic jet and a single nanofiber.* Chemical Engineering Journal, 2014. **244**: p. 540-551.
206. Raimi-Abraham, B., et al., *Generation of poly(N-vinylpyrrolidone) nanofibres using pressurised gyration.* Mater Sci Eng C Mater Biol Appl, 2014. **39**: p. 168-76.
207. Xu, Z., et al., *Physio-chemical and antibacterial characteristics of pressure spun nylon nanofibres embedded with functional silver nanoparticles.* Mater Sci Eng C Mater Biol Appl, 2015. **56**: p. 195-204.
208. Brako, F., et al., *Making nanofibres of mucoadhesive polymer blends for vaginal therapies.* European Polymer Journal, 2015. **70**: p. 186-196.
209. Zhang, S., et al., *Coupling Infusion and Gyration for the Nanoscale Assembly of Functional Polymer Nanofibers Integrated with Genetically Engineered Proteins.* Macromol Rapid Commun, 2015. **36**(14): p. 1322-8.
210. Mahalingam, S., et al., *Facile one-pot formation of ceramic fibres from preceramic polymers by pressurised gyration.* Ceramics International, 2015. **41**(4): p. 6067-6073.

2

A Comparison between Rotary Jet Spinning and Electrospinning

2.1 Introduction

A review of the current rotary jet spinning literature has been covered in chapter 1, which included a list of competing nanofibre production methods. One such highlighted method is electrospinning, which on comparison of the various production methods, reported fibre diameters closest to rotary jet spinning. In this chapter, we will investigate the direct comparison of producing polymeric fibres from both production methods, with the aim of finding distinct differences in the fibre morphology and processability.

Electrospinning is a process that is somewhat different from rotary jet spinning, in that it does not use any mechanical forces to expel or extrude a solution to produce a fibre. Instead it relies on a high electrostatic charge that is applied between a polymer solution, which is slowly ejected from a needle tip, and a counter electrode to collect the fibre. The attraction of the fibre that is being drawn from the capillary tip depends on a sufficiently high dielectric constant of the solution.

Until now, no direct comparison has been made between rotary jet spinning and electrospinning. In this study, a direct comparison of both spinning processes using one specific polymeric material was carried out under the same laboratory conditions. For this we investigated nanofibre production of polyamide 6 (PA6) and compared processability and fibre diameters for both methods, along with crystallinity of the resulting fibres.

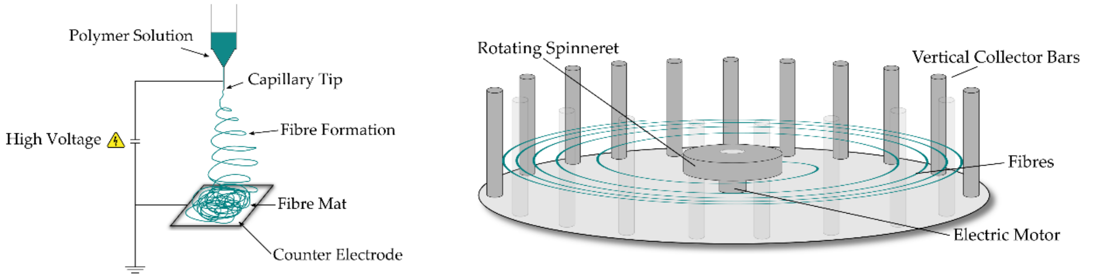

(a) (b)

Figure 2.1: Schematics of electrospinning (a) and rotary jet spinning (b), identifying key components from each technique in the production of nanofibres. The key difference is in the high voltage required by electrospinning to attract a fibre by drawing it from an oppositely charged capillary tip, whereas rotary jet spinning uses a mechanical force to eject polymer fibres from a fast-moving spinneret.

In rotary jet spinning, there are several variables which can be tuned to produce the required fibre properties, but not all of them have an influence on fibre diameter or bead formation. Processing parameters that have been shown to affect fibre diameter are the concentration of the polymer solution and needle size [1]. In their study, Krifa et al. evaluated the beads on a string phenomenon using PA6 solutions and performed an analysis of variance (ANOVA) to calculate the significance of these variables on the reduction of fibre beading. Early tests by this author are in agreement and have shown the smallest diameters to not depend on rotational velocities, but instead depend more so on the solution concentration and hence rheological properties of the spinning solutions.

The rate at which nanofibres can be produced varies according to the method and production variables, but can be summarised by concluding that electrospinning is as much as 50 times slower at producing nanofibres compared to rotary jet spinning [2]. Industrial electrospinning machines such as Nanospinner 416 by Inovenso (Turkey) are capable of producing 210 gh^{-1} [3], whereas an industrial rotary jet spinning device, the FX2200 by FibeRio (USA), can produce up to 12000 gh^{-1} [4] from a continuously produced 2.2 m wide nonwoven.

Lab-scale versions of these devices such as those used in this research usually have 1 or 2 needles. Electrospinning production rates versus rotary jet spinning in these research sized versions are still orders of magnitude lower, with lab-scale devices producing typically up to 0.11 gh^{-1} for electrospinning, and up to 60 gh^{-1} per orifice for rotary jet spinning [5].

It is with this benefit of increased production output that a direct comparison of the same material will be trialled to evaluate the fundamental differences and benefits that come from rotary jet spinning. For example, it might be envisaged that some loss in fibre quality will be observed due to the rapid fibre production rates in rotary jet spinning, compared to that of a more established and controlled process like electrospinning.

2.2 Experimental

2.2.1 Materials

For the polyamide 6 (PA6) grade chosen, our common control parameter was the polymer concentration in solution (viscosity), which was previously discussed as being a significantly influential spinning parameter. In our experiments, the electrospinning control parameters included the applied voltage and solution feed rate, whereas rotary jet spinning only included rotational velocity. The collector distance in both experiments was set to 10 cm.

To achieve directly comparable results, an identical polymer grade was used in both electrospinning and rotary jet spinning. PA6 pellets were acquired from Lanxess (Durethan B31F) (Mw unavailable), and Formic Acid (>98%) was purchased from Sigma Aldrich. All materials were used as received.

Polymer concentrations in solution were chosen to produce an array of results from non-fibre producing droplets and beading behaviour through to complete blockage and no fibre production at all. The solutions chosen ranged from 1 wt.% to 30 wt.% polymer concentrations in multiples of 2.5 wt.%.

Prior to solution preparation, the PA6 was dried at 80°C for 4 hrs to remove any residual moisture as per manufacturers' guidelines. Once dried, the solution concentrations were prepared by mixing together the formic acid and PA6 at ambient temperature using a stirring plate and magnetic stirrers. The solutions were stirred for a minimum of 72 hrs to allow complete dissolution, after which rheological testing was conducted using a TA Instruments rheometer (Discovery Hybrid Rheometer 3) fitted with a 40 mm plate-plate attachment to evaluate the viscosity at room temperature. A flow ramp test was initially conducted between 0 and 10,000 μNm over a duration of 600 s to establish the sample responses, after which the values were noted and used to perform a flow sweep. Flow sweeps were conducted between 10% of the initial flow ramp torque reading and 100% of the final torque reading, measuring 5 points per decade on a Log scale. Final values produced include all relevant readings for viscosity/shear rates measurable using this system. This method was used in all subsequent viscosity measurements throughout this research.

2.2.2 Fibre production

Electrospinning was conducted using an in-house built setup for all solution samples. The high voltage was produced using a Glassman High Voltage series FC which produced the 15-25 kV DC required, along with a Kent Genie syringe pump which facilitated the polymer solution delivery. Parameters were adjusted to find the most appropriate values for each solution sample for high fibre yield without visible droplets. A needle with an internal diameter of 600 μm was placed 10 cm from the collector plate, with applied voltage and volumetric feed rates varied according to Table 2.1.

Rotary jet spinning was performed using a FibeRio Cyclone L-1000D lab-scale device. A solution spinning setup was installed with a radial collector used to "catch" the fibres as they were spun. The solution spinneret contains two needles (160 μm internal diameter) to spin the fibres, with collector bars placed at 10 cm from the needle outlet. Variations of the angular velocity were trialled to select the most appropriate values for fibre spinning and are shown in Table 2.1.

Table 2.1: Variation in processing parameters used in electrospinning and rotary jet spinning. The values highlighted in bold represent the best combination of parameters to produce fibres for the specified solution.

		Electrospinning		**Rotary Jet Spinning**
PA6 concentration (wt.%)	**Viscosity (Pa.s)**	**Flow rate (ml/hr)**	**Applied voltage (kV)**	**Angular velocity (RPM - Thousands)**
1.0	0.005	0.1, 0.15, 0.2	15, 20, 25	2, 4, 6, 8, 10
2.5	0.010	0.1, 0.15, 0.2	15, 20, 25	2, 4, 6, 8, 10
5.0	0.028	0.1, 0.15, 0.2	15, 20, 25	2, 4, 6, 8, 10
7.5	0.068	0.1, 0.15, 0.2	15, 20, 25	2, 4, 6, 8, 10
10.0	0.112	0.1, 0.15, 0.2	15, 20, 25	2, 4, 6, 8, 10
12.5	0.199	0.1, 0.15, 0.2	15, 20, 25	2, 4, 6, 8, 10
15.0	0.614	0.1, 0.15, 0.2	15, 20, 25	2, 4, 6, 8, 10
17.5	1.11	0.1, 0.15, 0.2	15, 20, 25	2, 4, 6, 8, 10
20.0	2.09	0.1, 0.15, 0.2	15, 20, 25	2, 4, 6, 8, 10
22.5	3.30	0.1, 0.15, 0.2	15, 20, 25	2, 4, 6, 8, 10
25.0	5.59	0.1, 0.15, 0.2	15, 20, 25	2, 4, 6, 8, 10
27.5	10.3	0.1, 0.15, 0.2	15, 20, 25	2, 4, 6, 8, 10
30.0	27.7	0.1, 0.15, 0.2	15, 20, 25	2, 4, 6, 8, 10

2.3 Results

2.3.1 Solution characterization

The viscosity of the solutions shown in Figure 2.2 shows overwhelming Newtonian flow behaviour, with values ranging from 4.6 mPa.s to 27.7 Pa.s for 1 wt.% and 30 wt.% respectively. The solutions exhibit a steep increase in viscosity at a polymer concentration of 7.5 wt.%, where molecular chain entanglement (Me) starts to increase, and sufficient chain overlap develops to introduce viscoelastic effects in what has been termed the concentrated regime by Tsou et al. [6, 7].

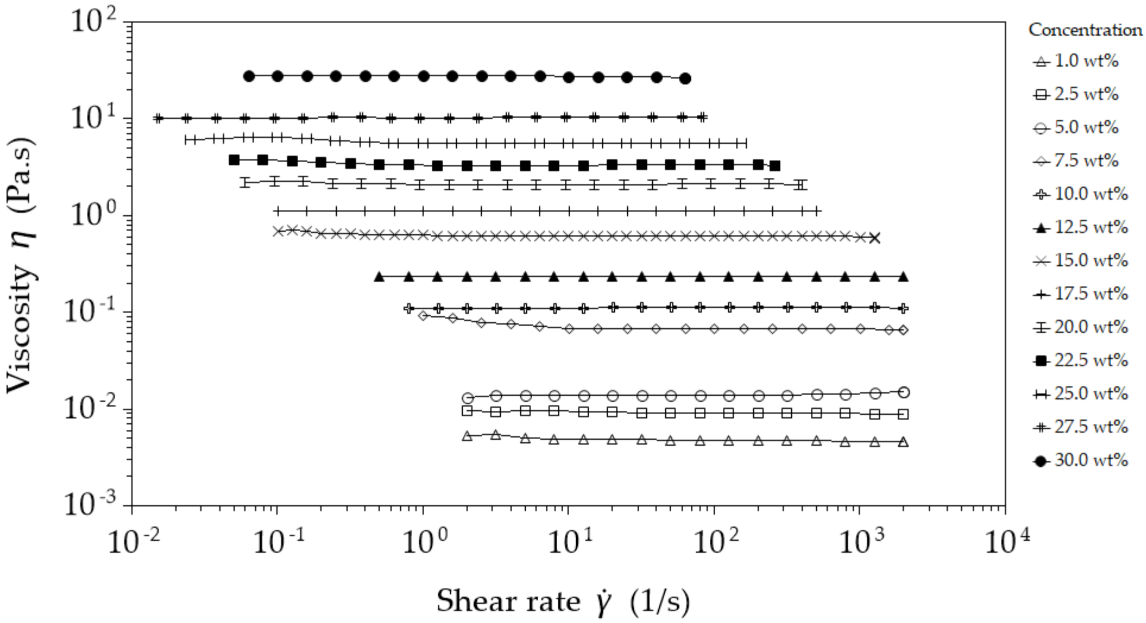

Figure 2.2: Viscosity data from plate-plate rheometry, showing the variation in Newtonian flow behaviour for polymer concentrations ranging from 1 wt.% to 30 wt.%.

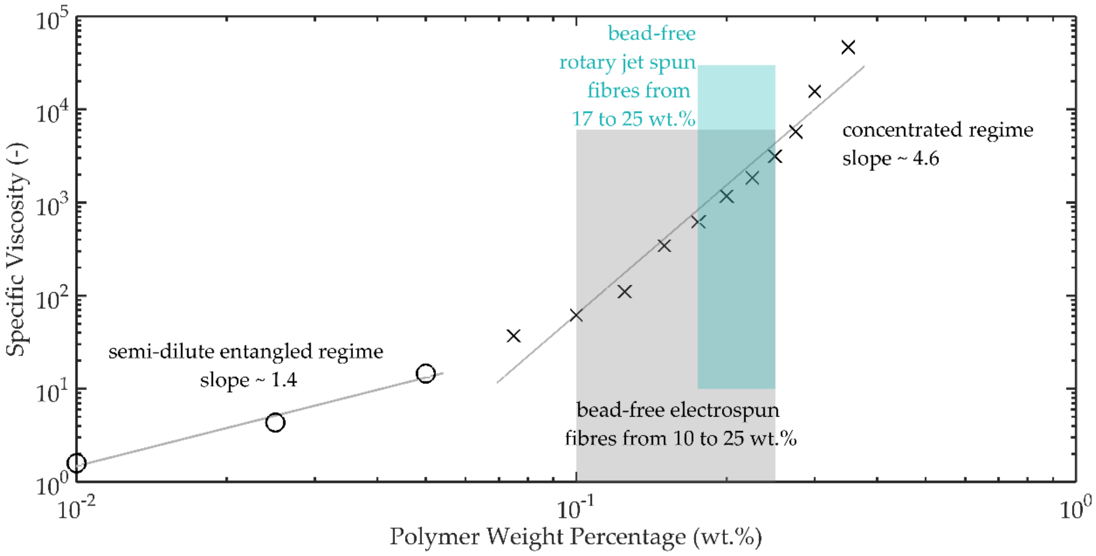

Figure 2.3: Plot of specific viscosity versus PA6 weight percentage, showing the transition from semi-dilute entangled regime to concentrated entangled regime, where fibre spinning starts in electrospinning (from 7.5 wt.%) and rotary jet spinning (from 17.5 wt%).

According to Tsou, the concentration of the polymer within the solvent will produce three distinct phases of rheological behaviour. From their work it can be shown that these phases are (a) semi-dilute disentangled regime, (b) semi-dilute entangled regime and (c) concentrated entangled regime. In the solutions prepared for this study and shown in Figure 2.3, we have the latter two regimes. It is in these regimes that fibres can start to be spun via both electrospinning and rotary jet spinning.

The surface tension of three solution concentrations was measured by pendant drop analysis using a Kruss DSA100 to evaluate the variation of surface tension with concentration. The chosen samples were 15 wt.%, 20 wt.% and 25 wt.%. The surface tension of formic acid is known to be 37.7 $mN.m^{-1}$, however with the inclusion of PA6, a small reduction in the surface tension was found. The three PA6 solution samples measured on average 34.1±0.3 $mN.m^{-1}$.

2.3.2 Fibre characterization

Samples were collected on aluminium foil and oven dried at 70 °C until their weight had plateaued to remove any residual formic acid from the fibres. Once dried, the fibre morphology was investigated using a scanning electron microscope (Jeol JSM-6300F), where multiple images at set magnifications were obtained.

At the lowest viscosities, both spinning methods did not produce fibres, but instead produced droplets of solution containing PA6 as seen in Figure 2.6. Upon deposition on the collector surface, the low polymer concentration solutions produced a coating following the evaporation of formic acid. Electrospinning produced continuous fibres from 7.5 wt% to 25 wt%, whereas rotary jet spinning only produced fibres from 17.5 wt% to 25 wt%, after which no fibres were produced from either method due to nozzle blockage.

Fibre diameters were measured in batches of 100 sample measurements using ImageJ software, and compared as shown in Figure 2.4. The standard deviations of the fibre diameters are larger in the rotary jet spun samples compared to the electrospun samples, as can be seen from the histograms in Figure 2.5. The increased standard deviation from the rotary jet spun fibres is common in this process due to the uncontrolled and chaotic deposition of the fibres.

The deposition process in rotary jet spinning is chaotic due to the spinning reservoir creating significant amounts of air turbulence from the fast-moving spinning head, which the fibres are required to negotiate before coming to rest. This leads to a larger standard deviation of diameters due to the way in which the fibres settle on one another in the current laboratory setup, which utilised a radial collector as illustrated in Figure 2.1. Conversely, the fibre deposition in electrospinning is done systematically by a constant electrostatic force without much interference from air turbulence, which resulted in the fibre deposition attaining an equilibrium, delivering relatively similar fibre diameters throughout deposition as shown in Table 2.2.

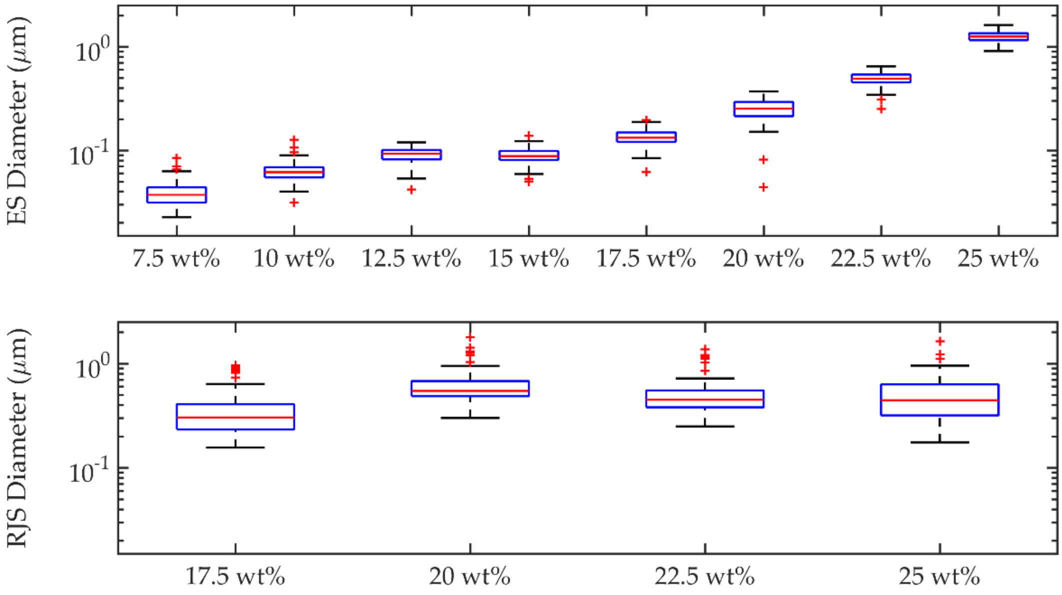

Figure 2.4: PA6 fibre diameters from electrospinning (top) and rotary jet spinning (bottom), showing the diameters of fibres produced in relation to solution concentration. The range of solutions capable of fibre production is lower for rotary jet spinning than for electrospinning due to the rate of solution evaporation within the process, which results in electrospinning producing fibres from effectively lower polymer concentrations.

Table 2.2: Range of fibre diameters from both electrospinning and rotary jet spinning, showing minimum, maximum and range of the fibre diameters. Electrospinning produced a lower variance in measured fibre diameter compared with rotary jet spinning.

Electrospinning fibre diameter ranges (μm)								
wt%	7.5	10	12.5	15	17.5	20	22.5	25
d_{min}	0.023	0.031	0.042	0.050	0.062	0.044	0.250	0.905
d_{max}	0.084	0.126	0.119	0.138	0.196	0.370	0.644	1.614
d_{range}	0.061	0.095	0.077	0.088	0.134	0.325	0.395	0.709

Rotary jet spinning fibre diameter ranges (μm)				
wt%	17.5	20	22.5	25
d_{min}	0.156	0.300	0.250	0.175
d_{max}	0.959	1.786	1.362	1.631
d_{range}	0.803	1.486	1.113	1.456

Figure 2.5 shows SEM images and fibre diameter data from the 22.5 wt.% spinning solution used for both methods. In the histograms, the curve clearly shows a larger standard deviation in rotary jet spun fibre diameters. This larger standard deviation in diameters was seen across all rotary jet spun samples produced compared with those from electrospinning.

As shown in Figure 2.6, the fibres in the rotary jet spun samples were much less compact and often collected in such a way that resulted in a reduction in the collector distance as the fibres formed a 3D network of attachments. A reduction in the collector distance due to this 3D network seemed to slowly increase the fibre diameters as they had less space to be drawn before becoming stationary. Given enough time, this reduces to no gap at all where the rotating needles will catch the previously formed nanofibres and pull them from the radial collector. Zander et al. have shown a slight increase in diameter with a reduction in collector distance to illustrate this point somewhat [8].

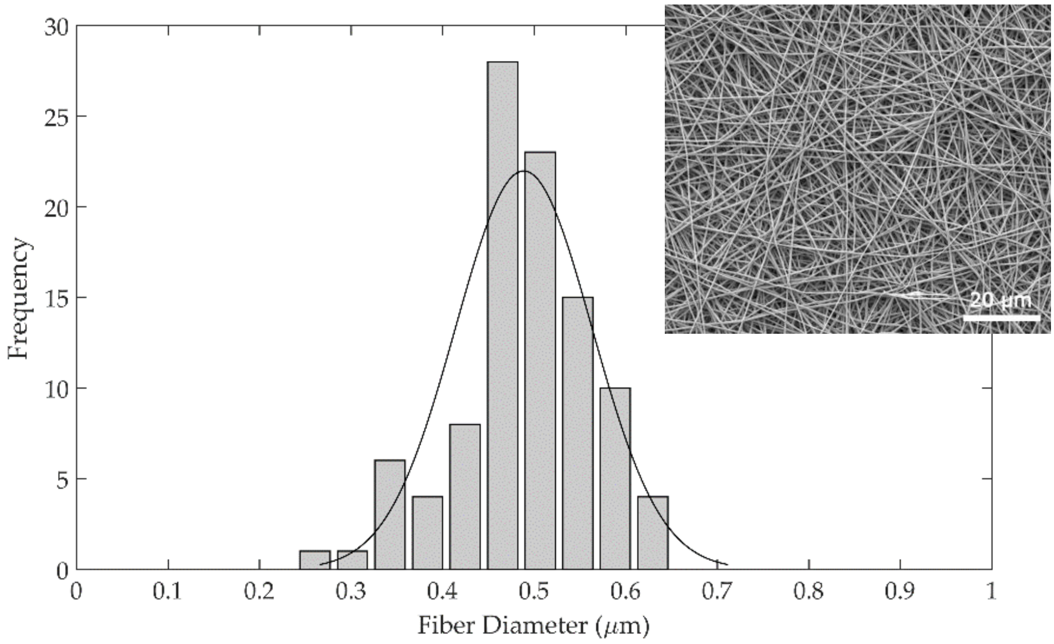

(a, b - inset)

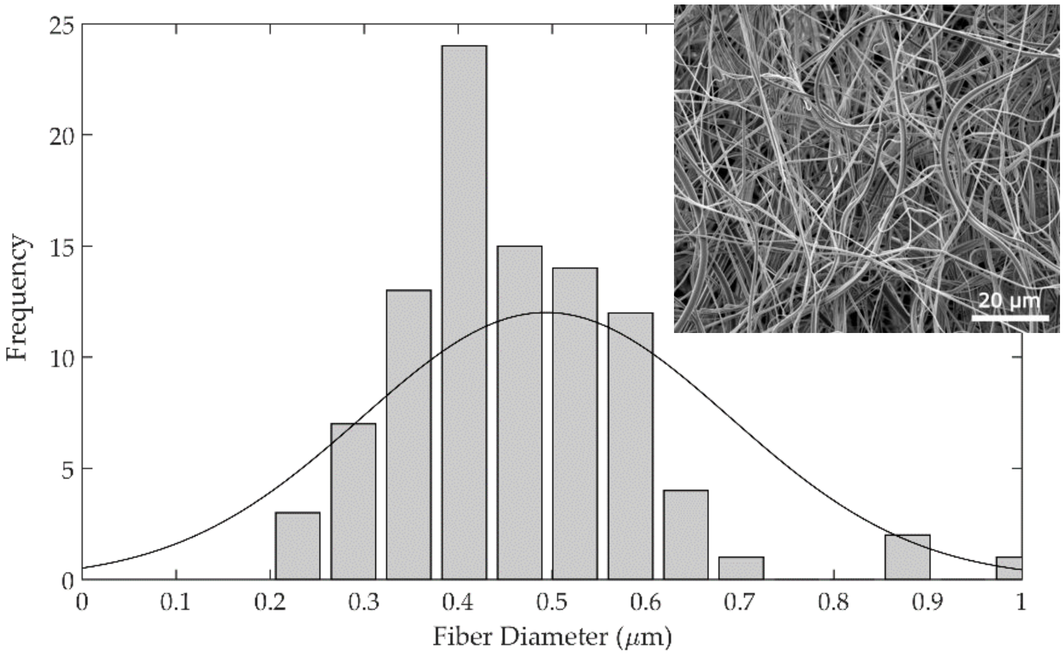

(c, d - inset)

Figure 2.5: Nanofibre histograms and SEM images from 22.5 wt.% PA6/formic acid solution using (a,b) electrospinning and (c,d) rotary jet spinning, showing a larger standard deviation for rotary jet spun fibres. The rapid production of rotary jet spinning in the lab scale device produces a more 3-dimensional deposition of fibres compared with a typical 2-dimensional morphology of electrospinning.

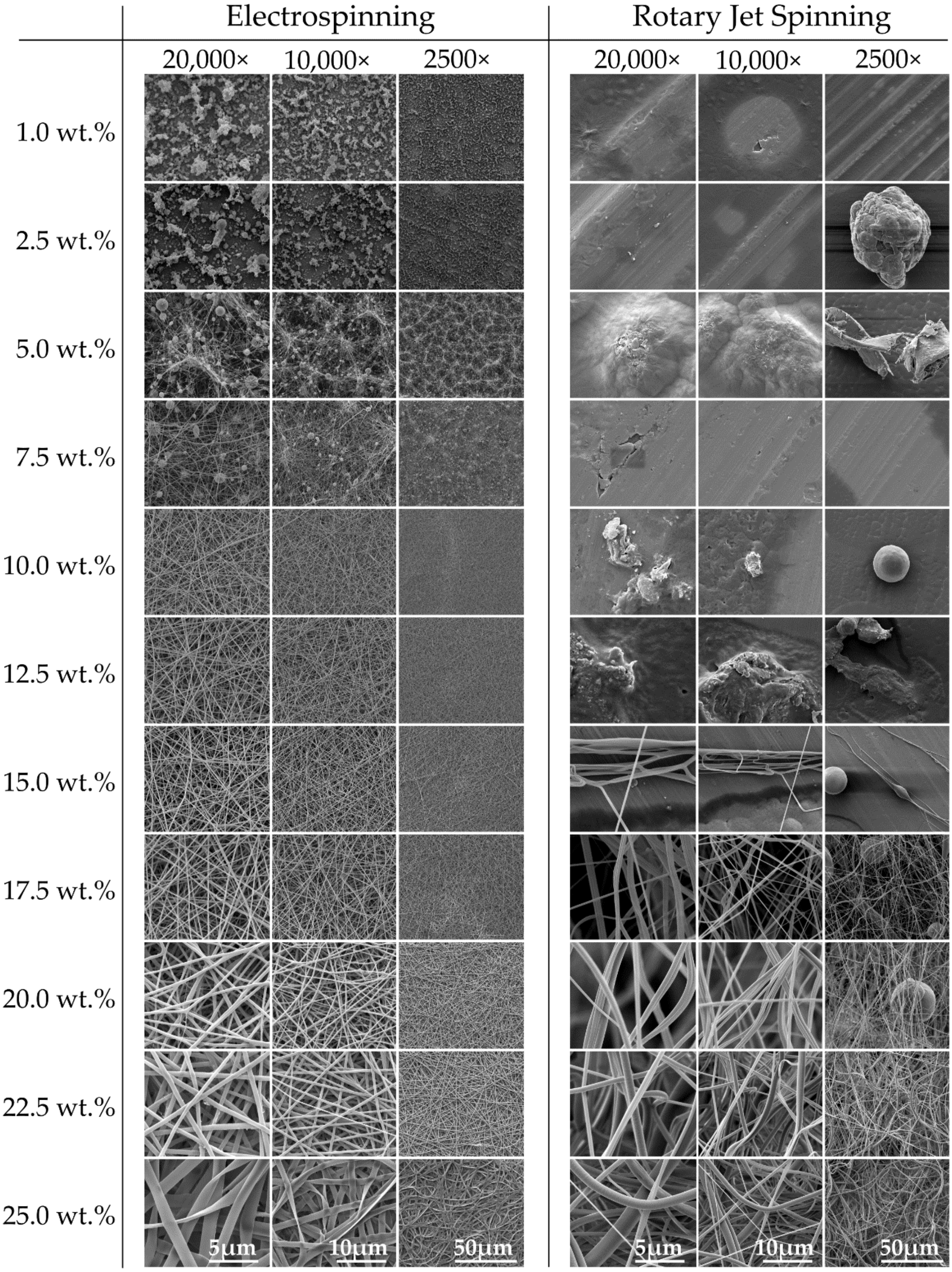

Figure 2.6: Scanning Electron Microscopy (SEM) of PA6 fibres produced from electrospinning (left) and rotary jet spinning (right). The images show the variation in fibre morphology between the two methods, with electrospinning producing less beaded fibres, including the benefit of fibre production over a wider viscosity range.

Differential scanning calorimetry (DSC) was performed using a TA Instruments DSC 25 for evaluation of fibre crystallinity. Samples were heated from 30 °C to 320 °C at 10 °C min^{-1}, held isothermally for 5 min before cooling at 10 °C min^{-1} to 30 °C. Figure 2.7 shows a comparison of DSC heat traces from the initial thermal ramp for 22.5 wt.% solution spun fibres and bulk PA6.

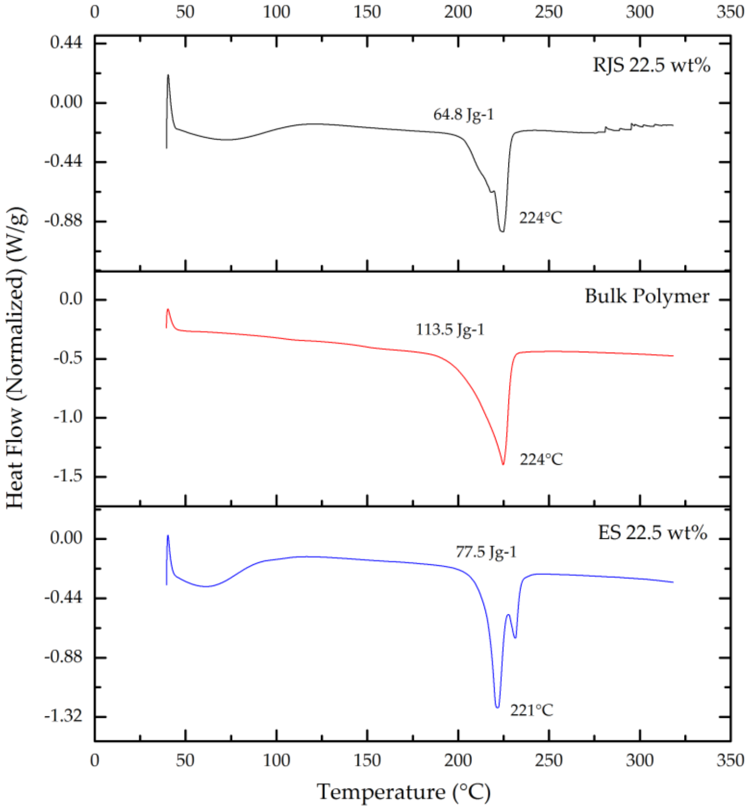

Figure 2.7: Differential scanning calorimetry (DSC) heating traces of PA6 fibres from rotary jet spinning, electrospinning and the bulk polymer, showing identical melting peak temperatures for PA6 bulk and rotary jet spinning. The bulk polymer typically contains slower forming α-form crystal structures whereas the faster forming γ-form crystals are present in the as-spun fibres due to the rapid evaporation of solvent from the spinning process.

Sample crystallinity (X_c) was evaluated using equation 2.1, where the observed enthalpy (H_f^{obs}) could be calculated by integrating the peak values from the DSC heat traces. The enthalpy of fusion ($H_f{}^o$) is taken to be 230 J g^{-1} for 100 % crystalline PA6 as per the suggested value by Wunderlich [9]. With this reference value, the crystallinity of all samples could be compared from the bulk polymer to the electrospun and rotary jet spun fibres.

$$X_c = \Delta H_f^{obs}/\Delta H_f^{o} \tag{2.1}$$

Table 2.3: Crystallinity comparison between electrospun fibres, rotary jet spun fibres and the bulk polymer, showing reduced crystallinity in fibre samples compared to the bulk polymer.

Polymer wt.%	**Electrospinning**	**Rotary Jet Spinning**	**PA6 Bulk Polymer**
10.0	32%	No fibre	-
12.5	35%	No fibre	-
15.0	37%	No fibre	-
17.5	35%	30%	-
20.0	29%	32%	-
22.5	33%	28%	-
25.0	31%	29%	-
100.0	-	-	44%
Average	**33%**	**30%**	**44%**

From Table 2.3 , it is clear the percentage of crystallinity from produced nanofibres is lower than that of the bulk polymer, highlighting a crystallinity difference of over 10% after fibre processing. This difference in crystallinity is an outcome of the method by which the crystal growth occurs during the bulk processing of PA6 pellets, where slower melt cooling promotes increased α-form crystal growth, versus the rapid solution evaporation that occurs in fibre formation where rapid γ-form crystal growth can produce a polymer with much less of a crystal structure than before [10].

2.4 Discussion

In this study, we set out to evaluate the difference in fibre morphology, crystallinity and production rates between electrospinning and rotary jet spinning. In the case of electrospinning, well-formed fibres were produced without beading between a polymer in solution range of 10 wt.% to 22.5 wt.%, where at 25 wt.% the fibres became ribbon-like. In contrast to this, the rotary jet spun samples produced fibres from 17.5 wt.% to 25 wt.% polymer concentrations in solution, although all but the 25 wt.% fibres showed some level of beading. Electrospun fibre diameters increased throughout, overlapping with rotary jet spun fibres at 22.5 wt.% (3.3 Pa.s).

Above 22.5 wt.% polymer concentrations in solution, the rotary jet spun fibre diameters remained below 1 μm, whereas in the case of electrospinning the fibre diameter almost doubled to 1.3 μm. This would indicate a significant change in the ability of the electrostatic field to attract the polymer solution from the capillary tip in which it no longer produces a cylindrical fibre. The benefit of the solution leaving the rotary jet needle is that it does not have to overcome any electrostatic charge, as it relies solely on centrifugal force and hydrostatic force to expel it. Using a 30 Ga (Internal diameter 160 μm) needle reduced the solution viscosity range that is capable of being spun, which resulted in a blockage of solution concentrations greater than 25wt.%.

Observations between the spinning methods accounts for some of the fibre diameter variations measured. The range of solution concentrations which can form fibres in electrospinning was shown to be larger, possibly due to the slower volumetric flow rate which allows the solvent to evaporate over a longer period of time during the spinning process. By having a lower volumetric flow rate, electrospinning ensures that the solvent is exposed to the air for longer from the point of solution ejection to polymer fibre collection, compared with rotary jet spinning. This speed differential in electrospinning increases its potential to produce fibres from lower polymer concentrations due to the change in viscosity occurring from evaporation of the solvent whilst the polymer solution is suspended from the capillary tip. The actual viscosity of the polymer solution jet at point of fibre elongation in electrospinning could be similar to that of RJS, which would account for the reduction in polymer solution concentrations that are able to be successfully electrospun.

Evaporation rates of the solvent during fibre formation would therefore be a significant contributor to the overall fibre diameter in both processes. During rotary jet spinning, the needle tip is moving at velocities between 40-75 m/s, where the evaporation rate is higher compared to electrospinning, due to the faster moving air over the fibre surface.

This variation in fibre diameters points to a production capability distinction. Smaller fibre diameters are capable of being produced from an electrospinning lab set-up to a point at which rotary jet spinning will produce a smaller diameter fibre - in the current system this is at 22.5 wt.% polymer in solution concentration. This key distinction would lead to either a choice for speed or fibre diameter in which rotary jet spinning would be favourable in terms of speed, while electrospinning would be favoured in terms of fibre diameter and uniformity of fibres produced. With electrospinning producing fibre at a rate of up to 50 times slower than rotary jet spinning, it is prudent to evaluate the requirements of a smaller diameter fibre over the time required to produce it. Electrospinning and rotary jet spinning apparatus, when scaled to industrial size units, could potentially see an alternative evidence as to the specific fibre morphology, but this is data not available in this study which is conducted using lab-scale devices.

The crystallinity of the samples was evaluated using DSC, which is one the easiest and most widely used methods of determining crystallinity [11]. Heat enthalpy of 100 % crystalline PA6 was used to calculate the degree of crystallinity in the fibres based on the integration of the heat enthalpy peaks in the samples. Surprisingly, very little difference is seen between the electrospun samples with an average of 33 % crystallinity versus those of the rotary jet spun fibres at an average of 30 %. The bulk polymer had a crystallinity of 49 %, which is in the region of what is expected for a semi-crystalline PA6.

Nylon 6 consists of two crystal forms, namely α-and γ-forms. The percentages of each form that contribute to the crystalline phase of the polymer depend on the rapidity and processing conditions of their formation. α-Form crystals are typically associated with slow crystallization and are formed from extended nylon 6 chains, whereas γ-form crystals are produced from rapid crystallization from pleated nylon 6 chains [10]. The total crystallization percentage of each process, including that of the bulk polymer, can therefore be attributed to the speed of crystallization as well as the processing conditions. The speed of crystallisation is influenced by factors such as temperature gradient and solvent evaporation rates, which between our comparative processes each undergo similar temperature gradients, however the rate of solvent evaporation is very different. In our study, the solution formed nanofibres from electrospinning and rotary jet spinning could have more γ-form crystal structures than α-form structures, and vice-versa for the slower crystal forming method of bulk melt processed nylon 6 pellets. Electrospun fibres could potentially contain more α-form crystal structures compared to rotary jet spun fibres due to the slower crystal structure formation time versus rotary jet spinning, which is known to produce fibres much more rapidly. This increased quantity of both types of crystal structures in electrospun fibres would result in a higher enthalpy, which is seen in Figure 2.7.

The degree of crystallinity will have effects on mechanical properties such as the modulus and fracture toughness of these fibres [12], however these measurements was not the focus of this study. Crystallinity within the fibre can also have a dependence on the age of the solvent due to the continued degradation of the polymer chains in the formic acid over time. A study by Nam et al. [13], for example, has shown that electrospun PA6 fibres had differing quantities of crystallinity from the same solvent after four consecutive weeks of trial. However, all samples in the current study were used within a week of each other.

2.5 Conclusions

In this comparative study we have set out to establish a direct comparison of creating polymer nanofibres by electrospinning and a relatively new technique called rotary jet spinning. With rotary jet spinning being a significantly faster method of creating fibres in the nanoscale, it could prove a very useful technique to exploit for industrial purposes. Fibres were formed from both methods from PA6 solutions in formic acid, and characterised based on their dimensions, spinnability and crystallinity.

Results showed that although rotary jet spinning can produce fibres faster than electrospinning, the morphology of those fibres was very different in average diameter over the whole spectrum of solution concentrations trialled. Up to a polymer in solution concentration of 22.5 wt.%, electrospun fibres had slightly smaller diameters which ranged from 39±11 nm to 488±74 nm, after which point rotary jet spinning produced fibres that measured the smallest diameter at an equivalent polymer solution concentration of 25 wt.% compared with that of electrospinning. Rotary jet spun fibres produced fibres in a narrower concentration range with fibre diameters ranging between 353±180 and 498±248 nm.

The crystallinity of the fibres measured showed that the change in crystallinity from bulk polymer was similar for both fibre production methods, with the bulk polymer having a crystallinity of 49 %, reducing to 33 % and 30 % for electrospinning and rotary jet spinning, respectively.

References

1. Krifa, M., M.A. Hammami, and H. Wu, *Occurrence and morphology of bead-on-string structures in centrifugal forcespun PA6 fibers.* Journal of the Textile Institute, 2015. **106**(3): p. 284-294.
2. Rogalski, J.J., C.W.M. Bastiaansen, and T. Peijs, *Rotary jet spinning review – a potential high yield future for polymer nanofibers.* Nanocomposites, 2017. **3**(4): p. 97-121.
3. *Industrial Electrospinning nanofiber machine | Inovenso, innovative engineering solutions*. 2017 29/06/2017]; Available from: http://inovenso.com/portfolio-view/nanospinner416/.
4. *Fiber Engine FX series systems from FibeRio*. 2014 29/06/2017]; Available from: http://www.filtsep.com/view/40670/fiber-engine-fx-series-systems-from-fiberio/.
5. Padron, S., et al., *Experimental study of nanofiber production through forcespinning.* Journal of Applied Physics, 2013. **113**(2): p. 9.
6. Tsou, S.Y., H.S. Lin, and C. Wang, *Studies on the electrospun Nylon 6 nanofibers from polyelectrolyte solutions: 1. Effects of solution concentration and temperature.* Polymer, 2011. **52**(14): p. 3127-3136.
7. Tsou, S.-Y., et al., *Rheological aspect on electrospinning of polyamide 6 solutions.* European Polymer Journal, 2013. **49**(11): p. 3619-3629.
8. Zander, N.E., *Formation of melt and solution spun polycaprolactone fibers by centrifugal spinning.* Journal of Applied Polymer Science, 2015. **132**(2): p. 9.
9. Wunderlich, B., *Equilibrium Melting*, in *Macromolecular Physics*. 1980, Academic Press: San Diego. p. 1-127.
10. Liu, Y., et al., *Crystalline Morphology and Polymorphic Phase Transitions in Electrospun Nylon 6 Nanofibers.* Macromolecules, 2007. **40**(17): p. 6283-6290.
11. Millot, C., et al., *Assessment of polyamide-6 crystallinity by DSC.* Journal of Thermal Analysis and Calorimetry, 2015. **122**(1): p. 307-314.
12. Bessell, T.J., D. Hull, and J.B. Shortall, *The effect of polymerization conditions and crystallinity on the mechanical properties and fracture of spherulitic nylon 6.* Journal of Materials Science, 1975. **10**(7): p. 1127-1136.
13. Nam, K.-T., et al., *Solvent degradation of nylon-6 and its effect on fiber morphology of electrospun mats.* Polymer Degradation and Stability, 2011. **96**(11): p. 1984-1988.

3

High Modulus Nanofibres by Rotary Jet Spinning

3.1 Introduction

Modern material scientists are forever attempting to tune the capabilities of the materials that are being used in our daily lives to improve them in one aspect or another. Fibre of all sizes are in constant use in our daily lives, with a multitude of mechanical and physical property variations. One such property that is often coveted is the tensile strength or tensile modulus of fibres when used in applications that require high performance materials. Thus far, rotary jet spinning has produced limited success regarding mechanical property characterisation for the purposes of high modulus fibre production.

High modulus polymeric fibres perform best when loads are applied in the fibre direction and/or the direction of chain orientation and extension, which in microfibres is relatively easy to achieve through traditional spinning and drawing methods. There is however a difficulty associated with the scale of nanofibres which inhibits the ease of post processing to align chains given current techniques such as cold-drawing (i.e. mechanical stretching or drawing below the polymer melting temperature). It is however possible to achieve high mechanical properties in polymer nanofibres, which was demonstrated from co-polyimide fibres that were produced from polyamic acid (PAA) solution via electrospinning [1, 2].

Traditionally, achieving a high modulus fibre relies on one of three principles. Firstly, fibres can achieve a high modulus directly from high elongational flow, which can induce chain orientation when using lyotropic rigid rod molecules such as in the case of poly(phenylene terephthalamide) (PPTA) for the creation of Kevlar® or Twaron® fibres [3]. Secondly, through post-drawing of the as-spun fibres based on flexible chain molecules like polyethylene, as in the case of Dyneema® or Spectra® fibres, to initiate molecular orientation and chain extension within the molecular network of the fibre [4]. Lastly, high modulus fibres can be achieved through chemical treatment methods as in the case of polyimide fibres, where chain extension is achieved through a combination of spinning conditions and specific imidization procedures [2, 5, 6]. Here, we are investigating the creation of high modulus co-polyimide nanofibres by RJS followed by a chemical treatment as a path to potentially achieve a high modulus fibre. The objective is to compare the properties of these RJS co-polyimide fibres with those prepared by electrospinning (ES), based on published data.

Producing nanofibres by means of RJS or ES requires polymers to be processed via either solutions or melts as is common with most fibre production methods. Due to the insolubility of some polymers however, it is sometimes necessary to use harmful solvents when preparing solutions for fibre spinning. Some of these solvents, such as 100% anhydrous sulfuric acid for PPTA solutions, are particularly corrosive and toxic, but can produce high modulus fibres.

In contrast to rigid polymers where a high modulus can be almost guaranteed from the as-spun fibre, other polymers such as polyethylene are required to undergo a post drawing process in the solid state just below the melting temperature of the as-spun fibres to increase their mechanical properties by initiating chain alignment. This is easily achievable when a continuous fibre spinning line is working at the micron scale, but rather difficult with current spinning technologies at the nanoscale. ES and RJS fibres typically have a diameter below 500 nm and are not produced in a way that easily facilitates post drawing to increase their mechanical properties.

Selecting a polyimide which could exhibit favourable properties for fibre production was the subject of a recent study by Chen et al. [1] where they investigated the options of various combinations of monomers as well as co-polymerisation of monomer blocks. In their study, they found that electrospun co-polyimide nanofibre ribbons exhibited both high modulus and strength versus homo-polyimide fibres which only showed a high modulus. 3,3′,4,4′-biphenyl-tetracarboxylic dianhydride (BPDA), p-phenylenediamine (PDA) and 4,4′-oxydianiline (ODA) were the 3 monomers used in their study, and by altering the ratio of the flexible ODA and rigid PDA moieties, they were able to create an intermediate polymer called polyamic acid (PAA), where strong hydrogen bonding between PAA and solvent ensured solubility – a quality required for solution-based fibre spinning. These fibres were electrospun into aligned fibre bundles by collection on a rotating disc, before undergoing sample characterisation. Imidization was subsequently conducted to carry out the ring closure, creating a co-polyimide fibre.

Yao et al. [2, 7] expanded on this study, producing co-polyimide nanofibres which exhibited very high strength and stiffness. In their paper, an elastic modulus of a single fibre was calculated to be 59 GPa, close to that of commercial high-performance fibres like Kevlar 29 (70 GPa [8]). This was achieved through both direct testing of aligned bundles of up to 30 nanofibres in a micro-tensile tester, and indirectly in composite laminates using micromechanical theory to back-calculate the properties of the individual fibre.

Few RJS publications report on mechanical properties, with those that have, measuring values as low as 22% of the bulk modulus for polytetrafluoroethylene (PTFE) (348 MPa versus 1.6 GPa) [9] in a yarn twisting tensile test, and a modulus of 126 MPa for poly(3-hydroxybutyrate-co-3-hydroxyvalerate) (PHBV) [10] in a tensile test of a nonwoven nanofibre mat. Both fibres cannot claim to be "high modulus", but this shows the limitation of the current understanding of mechanical properties of the fibres produced from RJS.

The alignment of nanofibres from direct RJS collection methods is not possible at present due to the nature of the deposition technique. Fast spinning RJS nozzles create significant amounts of turbulence and therefore influence the flight path of depositing nanofibres which results in a random deposition orientation. Conversely, electrospinning can employ rotating disc collectors to “catch” the fibre as they progress towards the collector, aligning the fibres on contact [4]. Combining the two technologies of RJS and ES has moved towards aligning RJS fibres as recent successful studies have shown [11, 12]. On the other hand, with these methods, the alignment of polymer chains within the fibres remains rather poor.

The measurement of Young’s modulus from individual polymer nanofibres is a challenge due to their size as discussed in Chapter 1. Because of this, problems exist in their mechanical performance measurements, with reported values of single nanofibre modulus remaining very limited. Primarily, these issues are due to the ability to manipulate them effectively as well as finding suitable modes of observation. Methods such as atomic force microscopy (AFM) cantilever bending [13-15] or nano-tensile testing [2, 16, 17] have been attempted in the past with single and bundled nanofibres respectively. Specific issues include the availability of accurate and sensitive force transducers with high enough resolution to measure single nanofibres [18]. All methods available do however require intricate test rigs and pin-point accuracy from the operator during testing so as not to damage the fibre pre-test by way of applying a pre-tension to the fibre, or as in the case of AFM assisted testing where radiation damage of the fibre is possible.

3.2 Experimental

3.2.1 Materials

3, 3’, 4, 4’-Biphenyltetracarboxylic dianhydride (BPDA), 4,4’-Oxydianiline (ODA), p-Phenylenediamine (BPA) and N,N-Dimethylformamide (DMF, 99.8%, anhydrous) solvent was supplied by Sigma Aldrich. The two-component low viscosity epoxy resin PX771C (bisphenol A diglycidyl ether, DGEBA) and HX932C (aromatic amine) were supplied by Robnor Resinlab (UK) and mixed at a weight ratio of 100:24.

3.2.2 Synthesis of co-polyimide polyamic acid

5.884 g (0.02 mol) BPDA, 1.081 g (0.01 mol) PDA and 2.002 g (0.01 mol) ODA (mole ratio of 2:1:1) were mixed together in 40.504 g of DMF using a three-neck flask, which was continuously ventilated with nitrogen. Intense mechanical stirring was applied during the polycondensation process at a low temperature (±0 °C) for approximately 2 hrs. A 20.7 wt.% solution of polyamic acid (PAA) in DMF was obtained for use in fibre production.

3.2.3 Rotary jet spinning

A FibeRio L1000-D Cyclone Forcespinning™ system (Figure 3.1) was used to conduct the rotary jet spinning, with all samples being spun at room temperature. To produce the fibres, approximately 1 ml of polyamic acid (PAA) solution was inserted into the spinneret fitted with two 30 Gauge (internal diameter of 0.16 mm), 12 mm long blunt tip needles to produce the fibres. Fibre collection consisted of a ducted fan collector box which was covered with a spunbound polypropylene mat to allow enough airflow to carry the fibres onto the surface. This was placed 16 cm away from the tip of the needle. A rotational velocity of 5500 rpm was used for all spinning trials, as this was deemed to produce the neatest fibre deposition from previous trials. Spinning was conducted for 18 min for each 90° turn of the fan box, ensuring equal coverage of the mat over multiple turns. After spinning, the mats were subsequently dried at 80 °C for 2 hrs to remove excess solvent, before storing in a freezer for characterization and imidization.

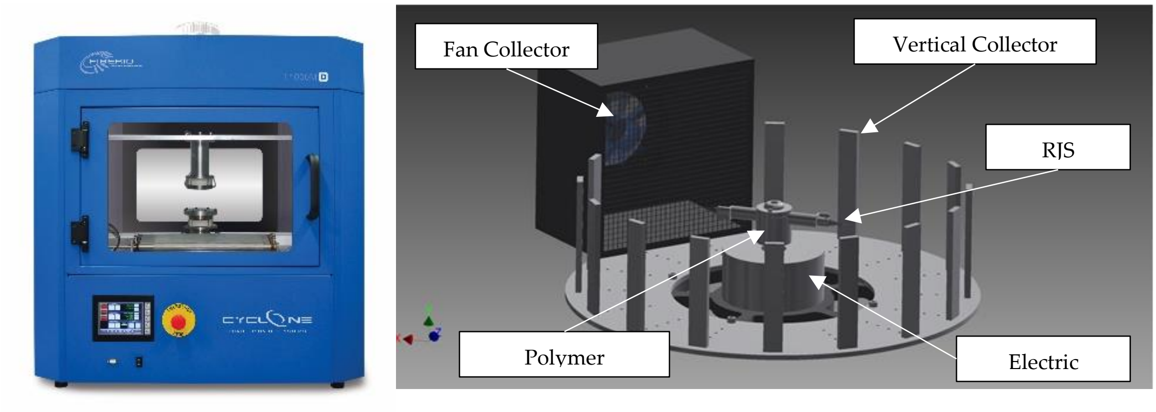

Figure 3.1: FibeRio L1000-D Rotary Jet Spinning Machine used (left), with schematic of fibre collection system (right).

3.2.4 Heat treatment imidization

The processing of a co-polyimide (co-PI) from a precursor polyamic acid (PAA) involves the simultaneous imidization, evaporation of residual solvent and crystallisation. The as-spun PAA fibres were processed into co-PI using the following heat treatment procedure in a nitrogen atmosphere. 1) Heating to 240 °C at 10 °C/min, annealing for 2 hrs, 2) Heating to 380 °C at 1.5 °C/min, annealing for 1 hr, 3) Cooling down to room temperature (RT). After processing, the chemical structure will change from a ring-open structure to a closed ring structure, providing greater mechanical properties, chemical resistance and thermal resistance.

3.2.5 Composite lay-up

To produce a composite, 15 Plies of nonwoven polyimide nanofibre mats (60 mm x 80 mm x 0.04 mm) were stacked after the application of epoxy to each ply in turn. Once all layers had been placed, a 4 kg weight was used to compress the composite whilst curing for 12 hrs in a vacuum oven at 120 °C. This resulted in a near void-free layered nanocomposite with a fibre loading of 7 wt.%.

3.2.6 Characterisation

Rheological characterisation of the polyamic acid was conducted with a TA Instruments DHR-3 Rheometer, using a 40 mm Peltier plate attachment. The morphology of the nanofibres was investigated using a scanning electron microscope adjusted to 5 kV (SEM, Jeol JSM-6300F), followed by fibre diameter analysis using ImageJ software. All samples were Au-coated for 30 s before SEM imaging to prevent charging.

Thermogravimetric analysis (TGA) was conducted on a TA Instruments Q500 under a N_2 atmosphere from RT to 600 °C at 10 °C/min. Differential scanning calorimetry (DSC) tests were also conducted using a TA Instruments DSC25, ramping at a rate of 10 °C/min from RT to 500°C. Fourier transform infrared (FTIR) characterisation was conducted to confirm the chemical structure of the fibres before and after imidization using a Brüker Tensor 27 instrument.

Tensile tests were conducted on the co-polyimide nanofibre reinforced epoxy composite using an Instron 5566 (100 N load cell) at an extension rate of 1 mm/min.

3.3 Results

3.3.1 Synthesis of BPO polyamic acid

The polycondensation process of the monomers BPDA, PDA and ODA in organic solvent is effective and rapid. The synthesis is therefore performed at low temperatures to inhibit side reactions. Several concentrations were produced for rheological characterisation, however the 20.7 wt.% solution of polyamic acid (PAA) in DMF was used for fibre production and subsequent analysis.

Figure 3.2 shows the chemical structure of the monomers used in the polycondensation reaction to produce the PAA. After synthesis of the PAA, spinning was performed, and the fibres were imidized to produce a co-polyimide fibre.

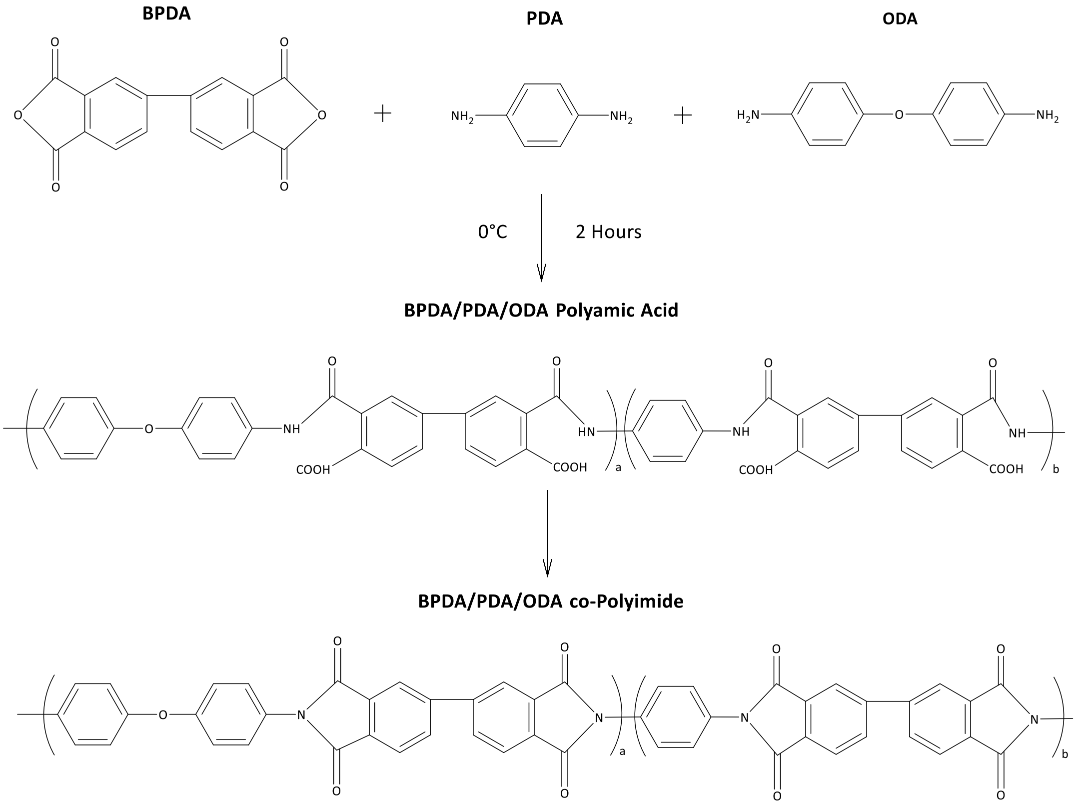

Figure 3.2: Low temperature polycondensation process from BPDA, PDA and ODA monomers to poly(amid acid) with dimethylformamide (DMF) as solvent, and subsequent imidization processing to produce co-polyimide.

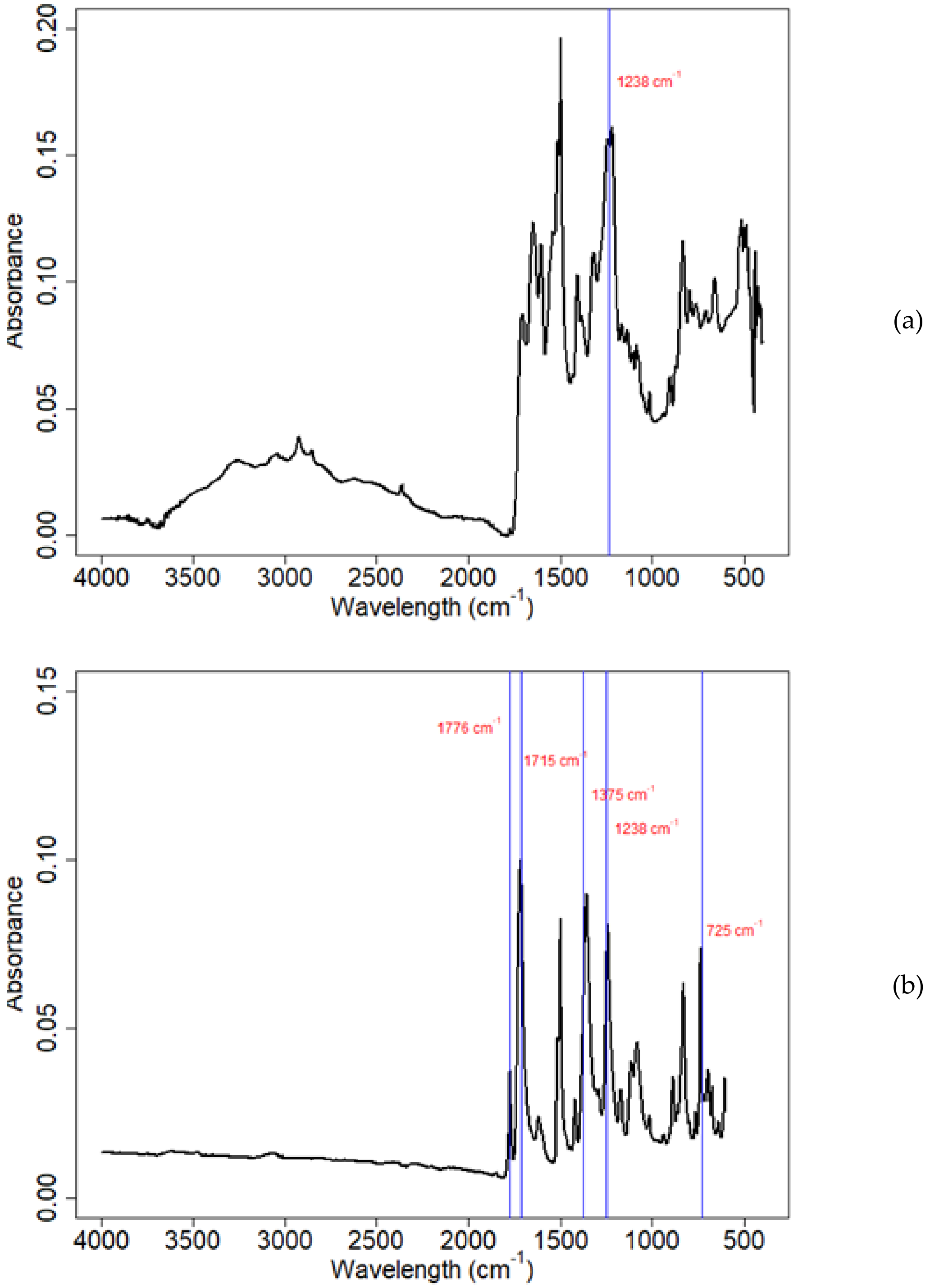

Figure 3.3: FTIR spectra of a) polyamic acid fibres and b) co-polyimide fibres, showing the characteristic change to the chemical structure from the appearance of new wavelength peaks at 725 cm^{-1}, 1375 cm^{-1}, 1715 cm^{-1} and 1776 cm^{-1}, confirming imidization. Moisture effects visible in (a) between 3800 cm^{-1} and 1800 cm^{-1}.

FTIR was used to analyse the success of the PAA synthesis and subsequent imidization process. In Figure 3.3 it is shown that the broad absorbance peak at 2900-3600 cm^{-1} has disappeared after imidization, which is attributed to the stretching vibration of the carboxyl groups and amide groups of the polyamic acid. The peak at 1375 cm^{-1} is attributed to the stretching vibration of the -C-N- in the imide ring, whereas both the peaks at 1776 cm^{-1} and 1715 cm^{-1} are an indication of the stretching vibration of the C=O in the imide. It can also be noted that the absorption peak at 1238 cm^{-1}, which appears in both spectrums is attributed to the stretching of the -C-O-, which is a confirmation of the existence of flexible ODA units in the copolymerised molecular chain. These results indicate that the BPDA/PDA/ODA polyamic acid has been completely transformed to BPDA/PDA/ODA co-polyimide [1].

Solutions of varying polymer weight concentration were produced to evaluate the viscosity ranges that could be used, with Figure 3.4 showing the shear viscosity curves for each solution. Solutions PI001 to PI005 varied from 20 wt.% to 30 wt.%, however the final solutions used for fibre production were 20.7 wt.% due to their ability to produce bead free fibres. Although samples PI004 and PI005 are both 20.7 wt.%, the viscosity variation is attributed to the total time allowed for the polycondensation reaction to complete.

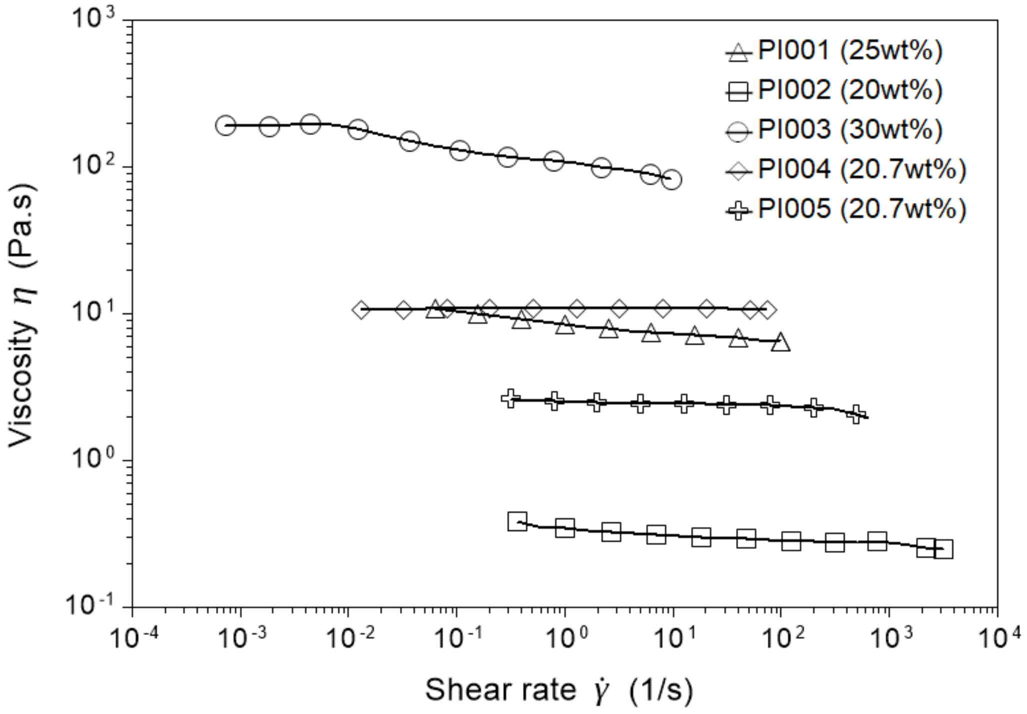

Figure 3.4: Viscosity of polyamic acid solutions at shear rates typical for RJS, showing viscosity vs. shear rate for multiple polyamic acid solutions.

3.3.2 Rotary jet spinning of PAA, imidization and characterization

Morphological characterisation was required to ascertain the fibre alignment and average fibre diameter. SEM imaging and subsequent analysis was conducted on 100 random fibres both before and after imidization, which yielded an average diameter just below 300 nm in each case. SEM images from before and after imidization are shown in Figure 3.5, along with fibre diameter histograms. Larger fibre diameters were disregarded due to the RJS start-up effects, as previous studies have shown that during the initial few seconds of RJS, fibres are produced that can be significantly larger than those produced after the process has become stable (typically ~30 sec) [19].

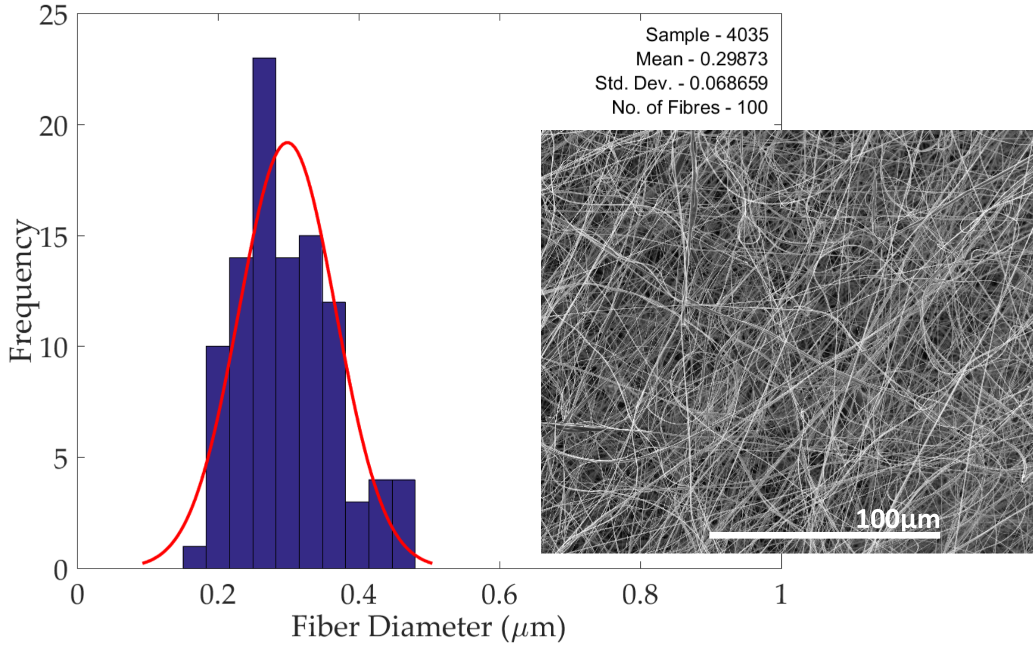

(a, b – inset)

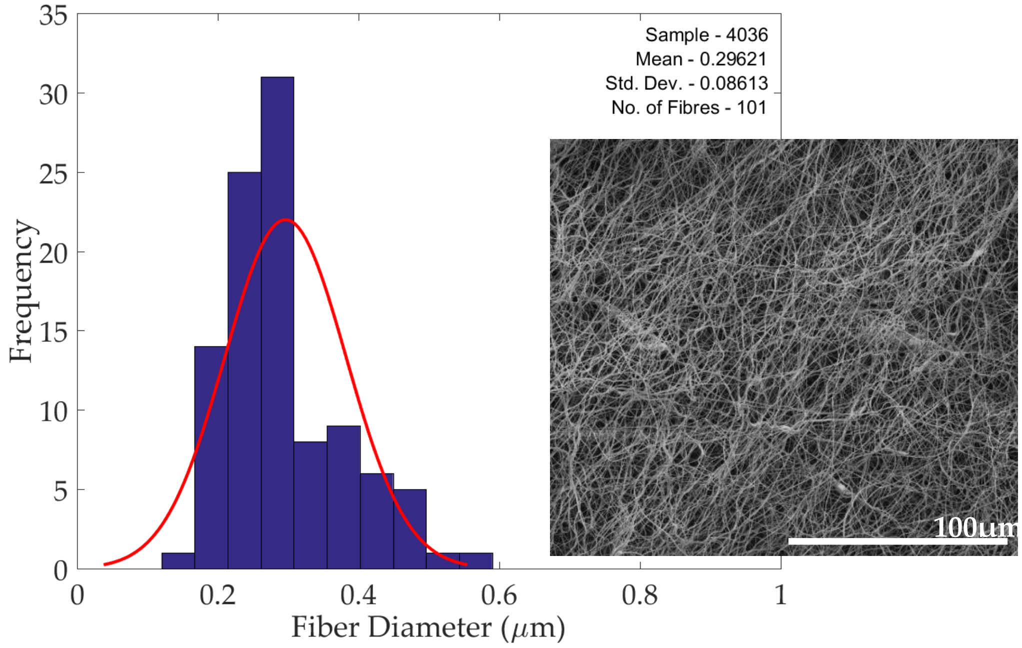

(c, d – inset)

Figure 3.5: Scanning electron microscopy images and fibre size distributions of (a,b) polyamic acid fibres and (c,d) co-polyimide fibres, showing the morphology before and after imidization.

To establish the orientation of the fibres, 500 co-polyimide fibres were analysed for their orientation, showing almost no orientation at all as illustrated in Figure 3.6.

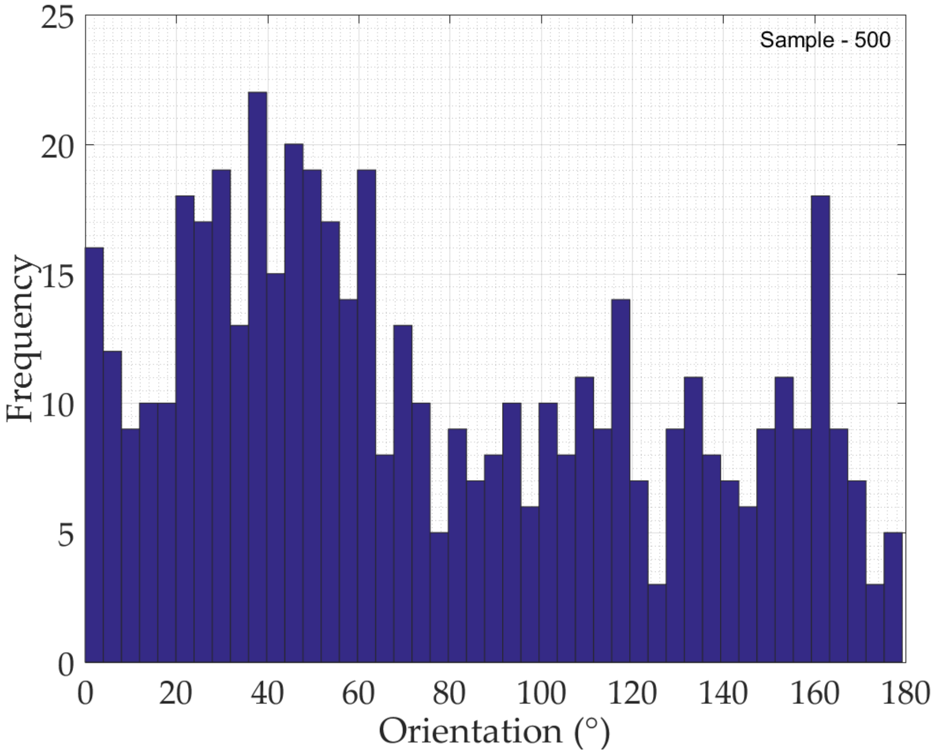

Figure 3.6: Orientation of co-polyimide fibres after imidization showing no fibre alignment, resulting in a randomly oriented fibre mat for use in composite mechanical testing.

3.3.3 Thermal analysis

Thermogravimetric Analysis (TGA) was performed to evaluate the change in decomposition temperature of the samples before and after imidization. It was found that the decomposition temperature increased from 119 °C for polyamic acid fibres to over 400 °C in the co-polyimide fibre as shown in Figure 3.7. Differential scanning calorimetry (DSC) analysis showed no melting enthalpy peaks in the range of testing, with pre-imidized fibres tested to 100 °C and post-imidized fibres tested to 500 °C.

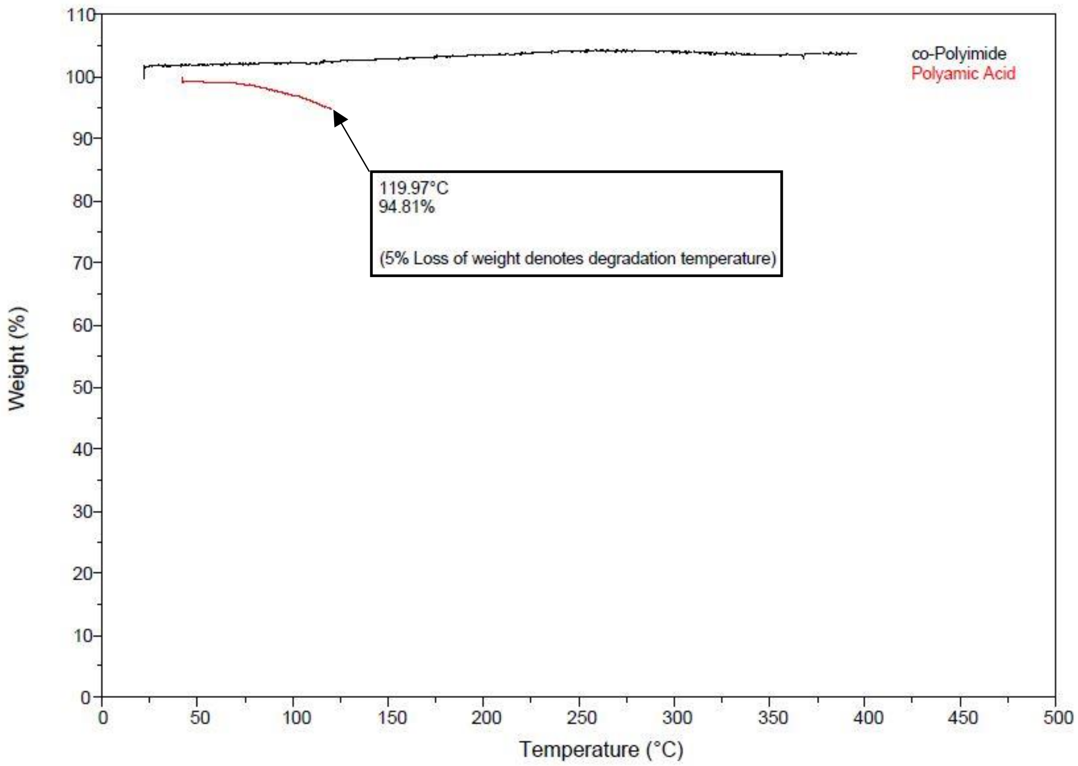

Figure 3.7: Thermogravimetric analysis (TGA) curves comparing the thermal degradation temperatures of the as-spun polyamic acid fibres (PAA) versus those of the imidized co-Polyimide (co-PI) fibres. Thermal degradation occurred at 120°C in PAA fibres, whereas no thermal degradation was detected in the co-PI fibres up to the measured range of 400°C.

3.3.4 Mechanical properties

The polymer composite was produced using a hand lay-up method, where individual mats of nanofibres were impregnated with epoxy resin before being stacked on top of each other as shown in Figure 3.9a. In the current research we have opted for a simplistic approach to mechanical characterisation of polymer nanofibres by creating a nanofibre composite and using the generalised rule of mixtures (gROM) to back-calculate the Young's modulus of the fibre as shown in equation 3.1:

$$E_c = \eta_L \eta_0 E_f V_f + E_m(1 - V_f) \qquad (3.1)$$

where η_L is the length correction factor - taken as 1 since fibres are continuous. η_0 is the fibre orientation distribution factor (varied between 0.2 for 3D and 0.375 for 2D orientations), E_m is the elastic modulus of the epoxy matrix (3.3 GPa flexural modulus as reported by manufacturer), V_f is the fibre volume fraction (7 vol%), and E_f is the fibre modulus. Using this approach, the fibre modulus can be back-calculated, with the values listed in Table 3.1. Limitations of this method include certain assumptions that need to be made which in most instances are not correct. These include assumptions that the fibres are bonded perfectly and continuously with the matrix, and that each fibre is under the same tension throughout the sample to ensure no localised stresses in certain fibres versus others.

Table 3.1: Back-calculated fibre moduli for different co-polyimide/epoxy composites samples prepared and tested assuming either a 3D or 2D random fibre orientation in the composite.

Sample No.	**Composite**		**Back calculated single fibre modulus (GPa)**	
	Width (mm)	**Thickness (mm)**	3D $\eta_0 = 0.2$	2D $\eta_0 = 0.375$
1	4.86	0.20	41.0	21.9
2	4.92	0.28	111.1	59.3
3	5.00	0.30	21.3	11.3
4	5.22	0.32	31.7	16.9
5	5.14	0.32	47.7	25.4
		Average	**50.6**	**27.0**

Individual samples were tested to failure as shown in Table 3.2 and Figure 3.8, with those that failed close to or within 2 mm of the clamps being disregarded. Using the generalised rule of mixtures to calculate the fibre modulus relies significantly on the orientation distribution factor, which varies from $\eta_0 = 0.375$ in 2D (in-plane) random fibre mats, as expected for nonwoven mats, to $\eta_0 = 0.2$ in a full 3D random fibre orientation. It can be expected that within these 2D fibre mats some fibres will experience out-of-plane orientations, which significantly affects the orientation distribution factor. The average Young's modulus of a single fibre was therefore calculated to be between 27 GPa when assuming a $\eta_0 = 0.375$ (3D), increasing to 51 GPa when assuming a $\eta_0 = 0.2$ (2D). From the SEM images shown in Figure 3.9, the fibre orientations in the composite are somewhere in-between 2D and 3D random. A realistic modulus of RJS co-polyimide nanofibres is therefore expected to be somewhere around 40 - 45 GPa.

Table 3.2: Tensile test data results from all composite samples available, demonstrating the variability in mechanical testing of nanofibre reinforced epoxy composites.

Sample No.	**Strain at break (%)**	**Ultimate tensile stress (MPa)**	**Young's modulus (GPa)**
1	3.9	11.2	3.54
2	5.1	12.3	4.29
3	6.1	11.6	3.29
4	1.3	4.4	7.48
5	5.3	11.9	3.35

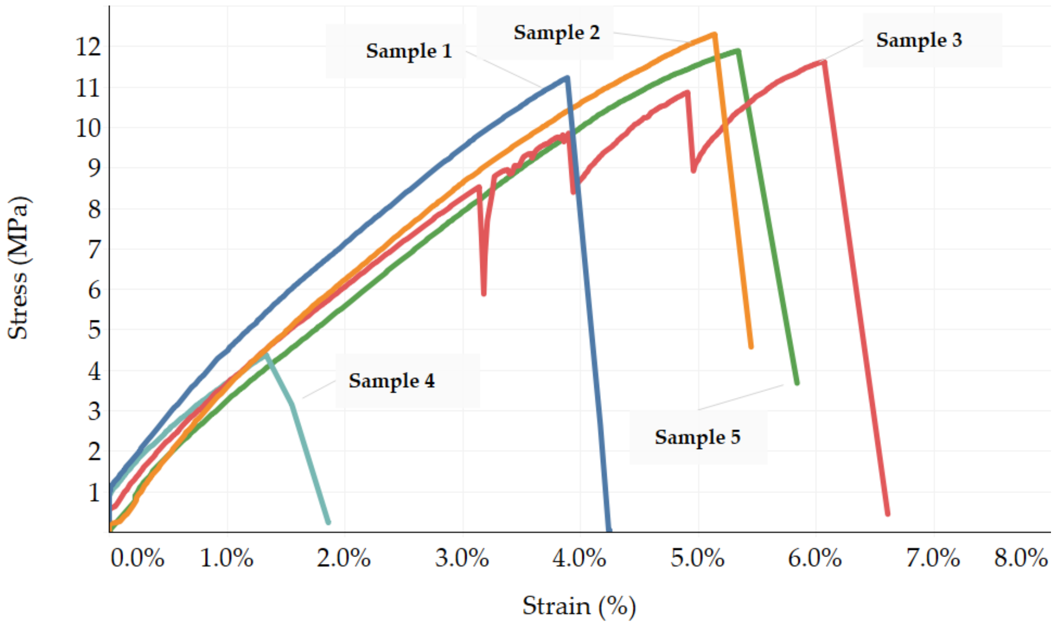

Figure 3.8: Stress-strain curves of composite samples, showing failure strains between 1 and 7%. Some debonding and crack propagation is evident in sample 3 (saw tooth line) before ultimate failure at 6% strain.

The study by Yao et al. [2] using electrospun BPO co-Polyimide, where bundles of ±30 nanofibres were tensile tested, resulted in a single fibre Young's modulus of 59 GPa, similar to the values indirectly measured and calculated here from the current composite data. The increased Young's modulus for fibres obtained from electrospinning could be attributed to an increased M_w during the polyamic acid solution preparation, and therefore increased mechanical properties from higher M_w. In their study, the polyamic acid produced by Yao et al. [2] underwent a polycondensation process over a period of up to 20 hours. An increase in polycondensation reaction time would result in a higher M_w over the polyamic acid produced in this study.

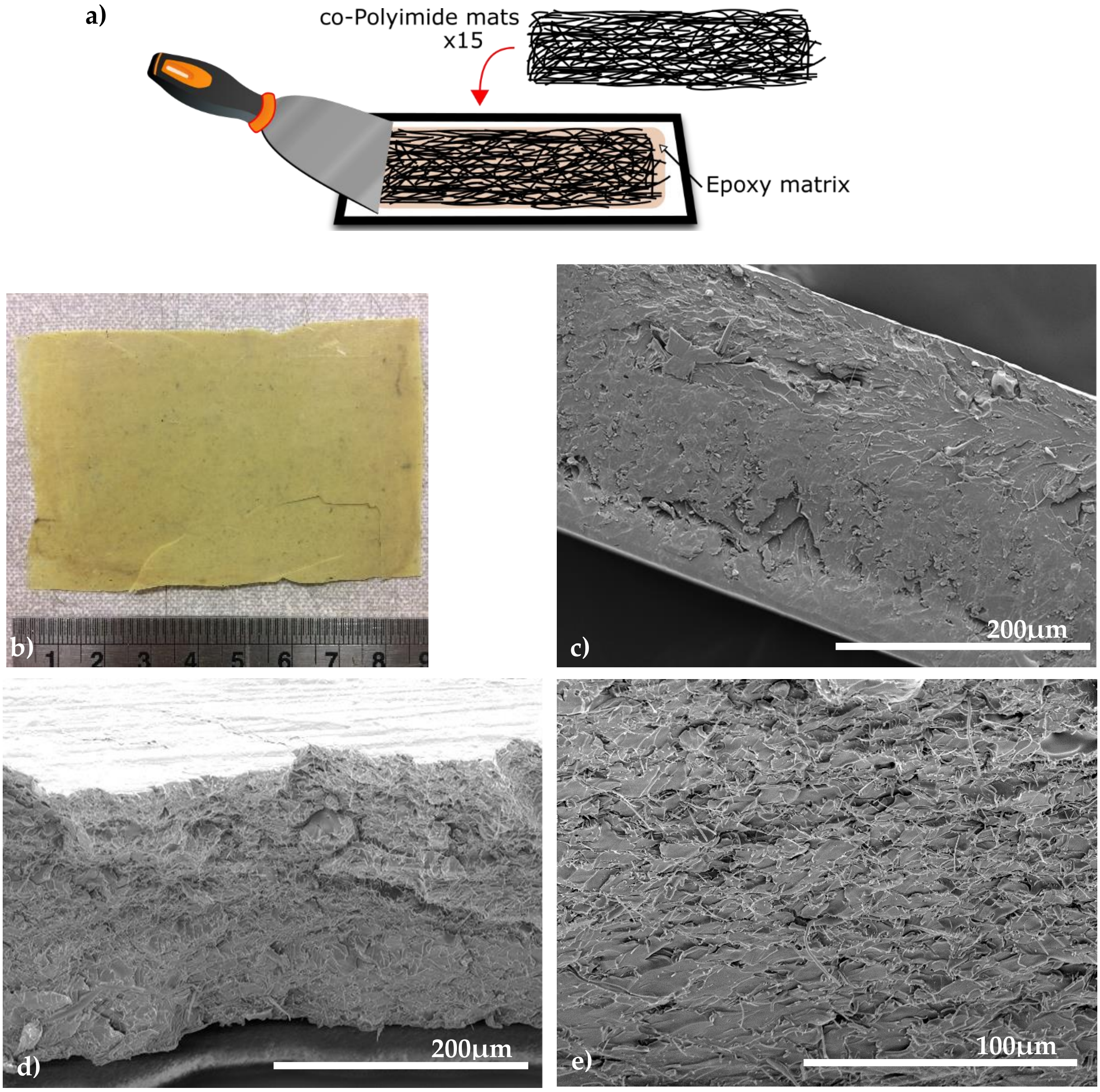

Figure 3.9: Schematic of the manufacturing process and SEM imaging of nanofibre reinforced epoxy composite. (a) Lay-up of co-polyimide nanofibre mats prior to curing. (b) The nanofibre reinforced epoxy composite (c) Cut edge of the composite, showing the fully impregnated side profile before tensile testing, (d,e) Images showing the edge of a fractured sample following tensile testing with some evidence of fibre pull-out and out-of-plane fibre orientations.

3.4 Discussion

The creation of high strength and modulus fibres has been in constant development, with highlights such as the introduction of commercial high strength polymeric fibres in the mid to late 20th century. The increase in mechanical properties has allowed fibres to compete with traditional materials such as steel, while offering significantly increased mechanical strength to weight ratios. These advances have primarily occurred in microfibres where industrial scaling has long since been achieved. However, although numerous studies have been devoted to the production of polymer nanofibres over the last two decades, large scale production of high performance nanofibres has yet to be achieved commercially.

As previously described, the manufacturing techniques available for nanofibre production are not all capable of up-scaling. The aim of rotary jet spinning is to bridge the gap between the requirement for further nanoscale fibres and up-scaling capabilities. Methods of nanofibre production do not lend themselves easily to physical manipulation for the prospect of increasing mechanical properties, and therefore make techniques such as cold drawing a near impossibility due to their small size. Investigating methods of producing high modulus fibres via rotary jet spinning was therefore embarked upon in this study.

Using rotary jet spinning as the basis for nanofibre production, it was our goal to evaluate the mechanical properties of these fibres in comparison to existing nanofibre production techniques where the same polymer had been used. As physical fibre manipulation such as drawing was not a possibility during or after our production process, we resorted to increasing the mechanical properties by submitting the as-spun polyamic acid fibres to an imidization treatment which converted them to co-polyimide fibres. It is this process which introduces chain extension and increases their mechanical properties, and which allowed us to obtain a back-calculated fibre modulus of around 40-45 GPa. This modulus is comparable to co-polyimide nanofibres produced from electrospinning, demonstrating that there is only a small variation in mechanical properties of fibres produced by electrospinning versus rotary jet spinning.

The largest comparative difference is, however, the production output of the two processes with lab-scale electrospinning being around 50 times slower than rotary jet spinning [20]. The most significant penalty for the increase in production speed with rotary jet spinning is however the inability to align the fibres. Fibre alignment plays a vital role in nanofibre applications that require good mechanical properties. With rotary jet spinning we were unable to align the fibres and could therefore only evaluate them for their mechanical properties through indirect composite testing. This inability to align the fibres directly in production will be a requirement of future work, which will undoubtedly see a great future interest in the fibre spinning process.

High strength and modulus nanofibres from rotary jet spinning remains an under-researched area, which was therefore a key focus in this Thesis. Creating as-spun fibres by rotary jet spinning that exhibit exceptional mechanical properties has not been reported anywhere to date. It was therefore necessary to evaluate an alternative process of increasing the mechanical strength, which resulted in the use of a multi-step system to achieve the desired outcome.

For successful fibre production, the rotary jet spinning process required a solution which had a low enough shear viscosity that would enable the production of nanofibres from rotary jet spinning. Once this necessary viscosity was achieved, the fibres were successfully produced and converted from a low mechanical strength polyamic acid fibre to a higher mechanical strength co-Polyimide fibre by the process of imidization as shown by the change in chemical structure in Figure 3.2. The multiple steps to create the co-Polyimide fibres are not too dissimilar to the production of carbon fibres from polyacrylonitrile (PAN) in their requirement for a high temperature post treatment after spinning.

Applications requiring unidirectional fibre alignment will however benefit from further research into the fibre collection methods to further guarantee increased fibre alignment.

3.5 Conclusions

In this work, we have set out to ascertain the ability for rotary jet spinning to produce nanofibres that possess high mechanical properties. In an attempt to produce a co-polyimide fibre from polyamic acid solution in DMF, we successfully produced nanofibres of around 300 nm in diameter, which are equivalent to those achieved in electrospinning. Imidization of the polyamic acid fibres was successfully conducted for the conversion to co-polyimide fibres, after which they were then mechanically tested within a composite by embedding multiple layers into an epoxy matrix. Tensile tests and subsequent back-calculation of the fibre modulus using the generalised rule of mixtures resulted in a co-polyimide fibre modulus between 30 and 50 GPa, depending on the 2D or 3D fibre orientation factor used. This value of single co-polyimide nanofibre modulus corresponds well with those already reported from electrospinning trials of the same polymer. The method of rotary jet spinning is therefore a realistically comparable method for relatively high-volume production of high modulus nonwoven nanofibre mats.

References

1. Chen, S., et al., *Electrospun nanofiber belts made from high performance copolyimide.* Nanotechnology, 2008. **19**(1): p. 015604.
2. Yao, J., et al., *High-performance electrospun co-polyimide nanofibers.* Polymer, 2015.
3. Yao, J., C.W.M. Bastiaansen, and T. Peijs, *High Strength and High Modulus Electrospun Nanofibers.* Fibers, 2014. **2**(2): p. 158-186.
4. Peijs, T., *High Performance Polyethylene Fibers*, in *In Reference Module in Materials Science and Materials Engineering*. 2017, Elsevier.
5. Ding, Y., et al., *Electrospun polyimide nanofibers and their applications.* Progress in Polymer Science, 2016.
6. Liaw, D.-J., et al., *Advanced polyimide materials: Syntheses, physical properties and applications.* Progress in Polymer Science, 2012. **37**(7): p. 907-974.
7. Yao, J., et al., *High performance co-polyimide nanofiber reinforced composites.* Polymer, 2015. **76**: p. 46-51.
8. Dupont. *Kevlar Technical Guide*. 30/06/2017]; Available from: http://www.dupont.co.uk/content/dam/dupont/products-and-services/fabrics-fibers-and-nonwovens/fibers/documents/Kevlar_Technical_Guide.pdf.
9. Rane, Y., et al., *Preparation of Superhydrophobic Teflon (R) AF 1600 Sub-Micron Fibers and Yarns Using the Forcespinning (TM) Technique.* Journal of Engineered Fibers and Fabrics, 2013. **8**(4): p. 88-95.
10. Upson, S.J., et al., *Centrifugally spun PHBV micro and nanofibres.* Materials Science and Engineering: C, 2017. **76**: p. 190-195.
11. Badrossamay, M.R., et al., *Engineering hybrid polymer-protein super-aligned nanofibers via rotary jet spinning.* Biomaterials, 2014. **35**(10): p. 3188-3197.
12. Erickson, A.E., et al., *High-throughput and high-yield fabrication of uniaxially-aligned chitosan-based nanofibers by centrifugal electrospinning.* Carbohydrate Polymers, 2015. **134**: p. 467-474.
13. Hang, F., et al., *In situ tensile testing of nanofibers by combining atomic force microscopy and scanning electron microscopy.* Nanotechnology, 2011. **22**(36): p. 365708.
14. Hwang, K.Y., et al., *Mechanical characterization of nanofibers using a nanomanipulator and atomic force microscope cantilever in a scanning electron microscope.* Polymer Testing, 2010. **29**: p. 375-380.
15. Tan, E., et al., *Tensile test of a single nanofiber using an atomic force microscope tip.* Applied Physics Letters, 2005. **86**(7): p. 073115.
16. Pai, C.L., M.C. Boyce, and G.C. Rutledge, *Mechanical properties of individual electrospun PA 6(3)T fibers and their variation with fiber diameter.* Polymer, 2011. **52**(10): p. 2295-2301.
17. Tan, E.P., S.Y. Ng, and C.T. Lim, *Tensile testing of a single ultrafine polymeric fiber.* Biomaterials, 2005. **26**(13): p. 1453-6.
18. Tan, E.P.S. and C.T. Lim, *Mechanical characterization of nanofibers - A review.* Composites Science and Technology, 2006. **66**(9): p. 1102-1111.

19. McEachin, Z. and K. Lozano, *Production and characterization of polycaprolactone nanofibers via forcespinning (TM) technology*. Journal of Applied Polymer Science, 2012. **126**(2): p. 473-479.
20. Rogalski, J.J., C.W.M. Bastiaansen, and T. Peijs, *Rotary jet spinning review – a potential high yield future for polymer nanofibers.* Nanocomposites, 2017. **3**(4): p. 97-121.

4

Rheological Modelling of the Rotary Jet Spinning Process

4.1 Introduction

Successful fibre production in RJS relies on the correct viscosity and viscoelasticity of the polymer solution or melt. It is this rheological window of opportunity which we seek to understand as it is doubtful that very low or very high viscosity solutions or melts will produce fibres. To achieve the required viscosity and viscoelasticity, polymer solutions can be altered by changing the polymer concentration in solution and/or polymer molecular weight, whereas polymer melt viscosity and melt strength can be adjusted through molecular weight and to a lesser extent the temperature of the melt. Moreover, changes will both also rely on the underlying polymer chains in terms of chain branching and molecular weight distribution.

In solution RJS, the dependence of the polymer concentration in solution has been investigated by Ren et al. [1], and as with electrospinning solutions, they demonstrate the presence of three solution regimes defining spinnability. Changes in these regimes occur when polymer chains are sufficiently entangled for chain overlap to occur, which results in a rapid increase in viscosity, aiding the fibre spinning process. This rapid increase in solution viscosity from a semi-dilute non-entangled to a semi-dilute entangled regime is termed the critical concentration (C*) where there is a sudden increase in zero shear viscosity.

This rapid increase in solution viscosity can be attributed to the increase in density of individual polymer coils present in the dilute solution. As the solution moves from a dilute regime, where adequate space exists between polymer coils, to a regime where the coils have a greater interaction with each other, an increase in viscosity is observed as per Rouse-Zimm model [2, 3]. It is at this increased interaction regime, termed the semi-dilute non-entangled regime, that sufficient polymer coil overlap occurs which results in chain connectivity and which induces viscoelastic effects in the solution. As the polymer concentration is increased to a critical concentration (C*), the polymer coils cease to remain separated and become entangled past this point in the semi-dilute entangled regime. This critical concentration can be estimated using the following equation [4],

$$C^* = \frac{M_w}{R_g^3 N_A} \tag{4.1}$$

where M_w is the weight average molecular weight, R_g is the radius of gyration and N_a is Avogadro's constant.

Ren et al. [1] reported the critical concentration for PLLA/PVP in dichloromethane solutions with polymer concentration in solution ranging from 1-10 wt.%, and PLLA:PVP ratios from 10:90 to 100:0. A critical concentration of 8 wt.% was reported where the first non-beaded fibres were produced by RJS due to sufficient polymer chain overlap, occurring at the changeover point from dilute non-entangled regime to semi-dilute entangled regime.

Another study by Lu et al. [5] evaluated the rotary jet spinnability of fibres from solutions of polyacrylonitrile (PAN, M_w = 150,000) and N, N-dimethyl-formamide. From their study these authors also concluded that bead free fibres could be produced from concentrations starting at 10 wt.%.

Two rheological processing regimes are relevant to polymer melts. These originate from sufficient or insufficient chain entanglements and are separated by a critical value termed the entanglement molecular weight (M_e). Before this value is reached, the slope of the $\eta_0 - M_w$ curve in logarithmic scale is ~1, whereas the instant chain entanglement increases sufficiently to reach M_e, the slope increases to ~3.4 [6, 7], suggesting a dense entangled regime:

$$\eta_0 \propto M_w^{3.4} \tag{4.2}$$

Typical entanglement molecular weights for polymers, as calculated by Vega et al. [8], include polyethylene (PE) at 1,200 g/mol, polypropylene (PP) at 5,200 g/mol and polystyrene (PS) at 14,900 g/mol.

According to Yan et al. [9], the viscoelastic properties of polyethylene's (PE) are also strongly affected by long chain branching of the polymer chains. The authors observed that compared to their linear counterparts with the same molecular weights, branched PE's gave higher viscosities at lower shear rates and lower viscosities at high shear rates. A similar study by Vega et al. [10] into the rheological behaviour of 13 narrow molecular weight distribution long chain branched PE's resulted in 8 of the polymers exhibiting a different rheological behaviour to that expected from linear (non-LCB) PE's.

The rheological behaviour of polymer solutions and melts below C* and M_e is approximately Newtonian. Non-Newtonian effects and the emergence of large extensional viscosities becomes more relevant with an increase in M_w [11]. Extensional viscosity is particularly important in spinning processes, in which the fluid elements are subject to substantial elongational flow or stretching.

For a Newtonian fluid, the extensional viscosity η_E is just three times the shear viscosity [12]. Therefore, for fluids that behave approximately Newtonian, the examination of the shear viscosity also provides a rough estimate of the extensional viscosity. However, for strongly non-Newtonian fluids the extensional viscosity can be much greater than three times the shear viscosity. In RJS and similar fibre spinning processes, the relation between extensional and shear viscosity is further complicated by the fact that fibre formation is a non-isothermal process in which viscosity increases dramatically during cooling.

Previous attempts to evaluate the fundamental characteristics of the fluid flow and fibre production of RJS have yielded limited results in terms of material selection biases. The numerical studies to date include a simple model for nanofiber size estimation from Mellado et al. [13] and several models for trends in fibre diameter and trajectories [14-17], including those specifically using models comparing Newtonian and non-Newtonian viscoelastic flow behaviour [18].

The studies mentioned here have exclusively reviewed the fibre characteristics such as trajectory and regions of fibre size reduction within the trajectory arc. However, none have evaluated the effect of changes in rheological behaviour of polymer solutions and melts to ascertain their spinnability in practical terms. The primary focus of these studies has assumed that the polymer solution or melt will produce a fibre, upon which their constitutive behaviour was used to evaluate the outcome of the final product.

To ascertain which rheological properties enable RJS fibre production, we will have to determine extrusion pressures, flow rates and a potential geometry dependence on predicting spinnability. To do this, computational fluid dynamics (CFD) will be used to evaluate the flow characteristics along with practical experimentation using a rotary jet spinner. From this data, we expect to produce a realistic viscosity region for the spinnability of different polymer solutions or melts based on their rheological profile and capabilities of the machine.

4.2 Experimental

To determine the spinnability of selected polymers for both solution and melt, physical experimentation and computational fluid dynamics (CFD) simulations were performed. Physical testing was conducted using a FibeRio L-1000D (USA) rotary jet spinner, whereas CFD was conducted using ANSYS CFX software. Solution spinning was the primary focus for the CFD analysis, however both solution and melt spinning experiments were conducted in the physical spinning trials.

4.2.1 Materials

The polymeric materials chosen for melt and solution spinning are presented in Table 4.1 and Table 4.2, respectively. A selection of polyethylene's (PE) was used with varying molecular weights for the melt spinning experiments (Table 4.1), while polyamide 6 (PA6) – formic acid solutions were created with different polymer concentrations in solution with the aid of magnetic stirrers for solution spinning experiments (Table 4.2).

Table 4.1: Polymers used in rotary jet melt spinning trials.

Ref.	**Polymer**	**M_w (g/mol)**	**T_m (°C)**
1	Polyethylene (Polywax 3000, Baker Hughes)	3,000	129
2	Polyethylene (HI-WAX™ , Mitsui Chemicals)	8,000	129
3	Polyethylene (Riblene MT10R, Versalis S.p.A.)	40,000	106
4	Polyethylene (InnoPlus HD5000S, PTT Chemical)	280,000	125

Table 4.2: Polymer solutions used in rotary jet solution spinning trials.

Ref.	**Polymer**	**Solvent**	**Polymer wt%**
5-11	Polyamide 6 (Durethan B31F, Lanxess)	Formic Acid	1, 5, 10, 15, 20, 25, 30

All polymers used were dried at 80°C as per the manufacturer recommendations prior to use in melt spinning and solution mixing to remove any residual moisture. After combining polymer and solvent, all solutions were stirred for several hours to ensure complete homogeneity before characterization and fibre spinning.

4.2.2 Rheology

For spinning processes, the extensional viscosity is an important parameter. However, measurements of extensional viscosity are challenging and require specialised equipment. Therefore, we have resorted to measuring shear viscosity only, under the hypothesis that the shear viscosity is proportional to the extensional viscosity for polymeric liquids that behave approximately Newtonian (for pure Newtonian fluids the Trouton ratio - being the ratio of extensional viscosity to shear viscosity - is 3). However, also outside the Newtonian regime, the characterization of shear viscosity still provides useful information about the response of a solution or melt to deformation.

Measurements of shear viscosity were obtained using both a TA instruments AR2000 (for melts) and TA instruments DHR3 (for solutions). Measurements were carried out in a plate-plate configuration. Shear viscosity vs. shear rate curves for solutions and melts are shown in Figure 4.1 and Figure 4.2, and are tabulated in Table 4.3. For polymers that exhibited non-Newtonian flow behaviour, rheological models were fitted to the flow curves for further analysis in comparison with Newtonian flows. The non-Newtonian model that showed the best fit for the measured data was the Cross model [19]:

$$\frac{\eta-\eta_\infty}{\eta_0-\eta_\infty}=\frac{1}{1+(k\dot{\gamma})^n} \tag{4.3}$$

where η_0 represents the zero shear viscosity, η_∞ represents the constant apparent viscosity attained at high shear rates, k is a time constant, $\dot{\gamma}$ is the shear rate and n is the power law index.

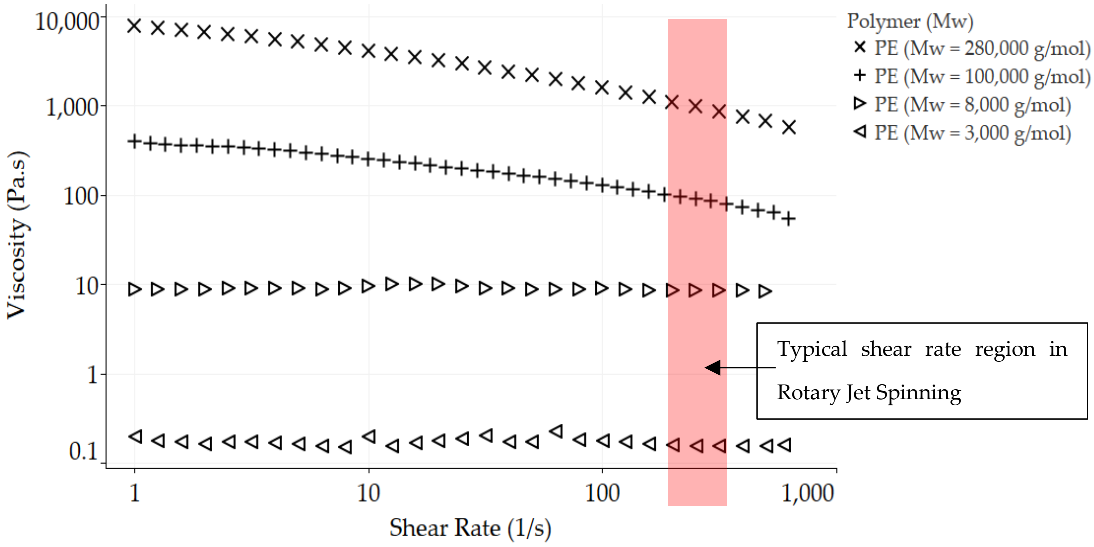

Figure 4.1: Viscosity measurements from plate-plate rheometry for polymer melts used in rotary jet spinning, showing a change from Newtonian behaviour for low M_w polyethylene to the non-Newtonian shear thinning behaviour for higher M_w polyethylene's.

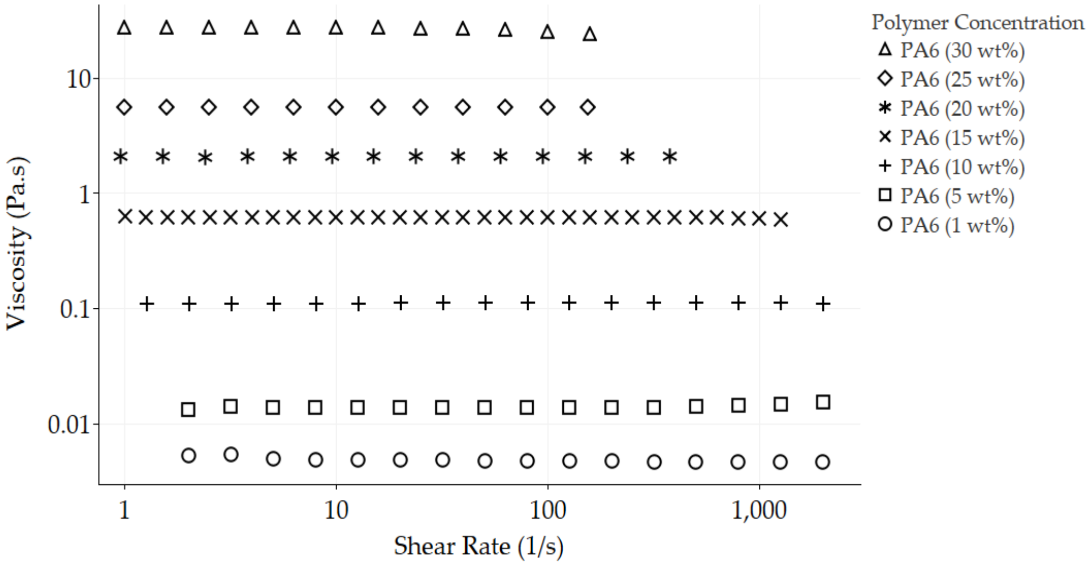

Figure 4.2: Viscosity measurements from plate-plate rheometry, showing the flow behaviour of the polymer solutions used in rotary jet spinning. All polyamide 6 solutions in formic acid exhibited Newtonian behaviour throughout all concentrations.

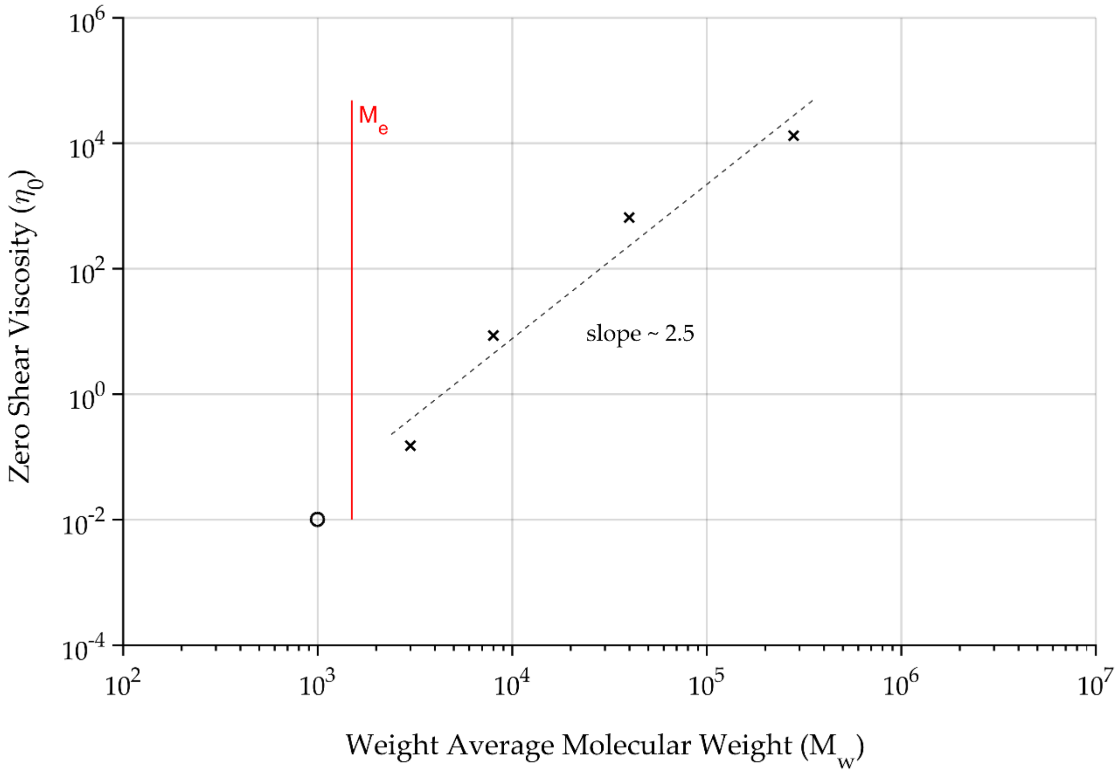

Figure 4.3: Weight average molecular weight versus zero shear viscosity of polyethylene's listed in Table 4.1, showing a slope of 2.5 for weight average molecular weight (M_w) values over entanglement molecular weight (Me) as indicated by the vertical red line. The slope value differs from 3.4 due to variations in polydispersity of polymer grades.

Table 4.3: Viscosity data for the range of polymer solutions and melts evaluated in rotary jet spinning. Newtonian flow behaviour parameters are shown as well as Cross model parameters for the non-Newtonian systems.

Ref.	**Polymer**	**Model**	η_0 **(Pa.s)**	η_∞ **(Pa.s)**	**k (s)**	**n**
1	PE – M_w 3,000 g/mol	Newtonian	0.145	-	-	-
2	PE – M_w 8,000 g/mol	Newtonian	8.58	-	-	-
3	PE – M_w 40,000 g/mol	Cross	646	-19.4	0.243	0.392
4	PE – M_w 280,000 g/mol	Cross	13156	254	0.653	0.455
5	PA6 – 1 wt.%	Newtonian	0.005	-	-	-
6	PA6 – 5 wt.%	Newtonian	0.015	-	-	-
7	PA6 – 10 wt.%	Newtonian	0.111	-	-	-
8	PA6 – 15 wt.%	Newtonian	0.598	-	-	-
9	PA6 – 20 wt.%	Newtonian	2.09	-	-	-
10	PA6 – 25 wt.%	Newtonian	5.58	-	-	-
11	PA6 – 30 wt.%	Newtonian	25.9	-	-	-

4.2.3 Computational fluid dynamics

For the validation and comparison of physical experimental data from RJS, a simple computational fluid dynamics (CFD) simulation was conducted. The variables used in the CFD analysis were identical to the experimental ones in terms of dimensions of the spinneret and rotational velocities. The internal geometry of the solution spinneret was replicated in the CFD simulation starting from a CAD model of the full device, as shown in Figure 4.4 (a-c).

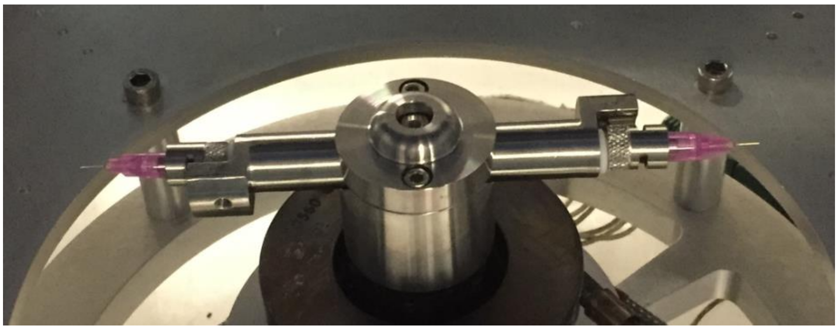
(a)

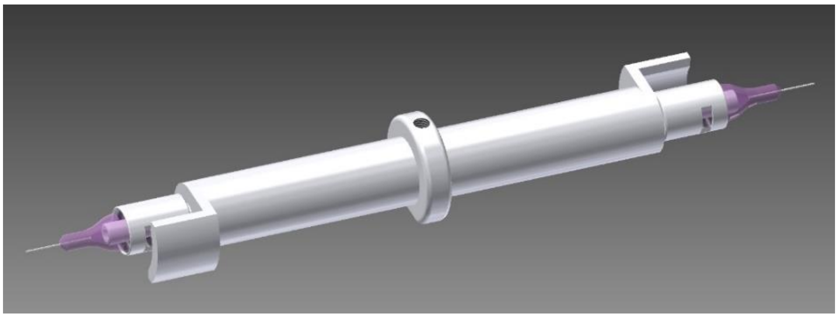

(b)

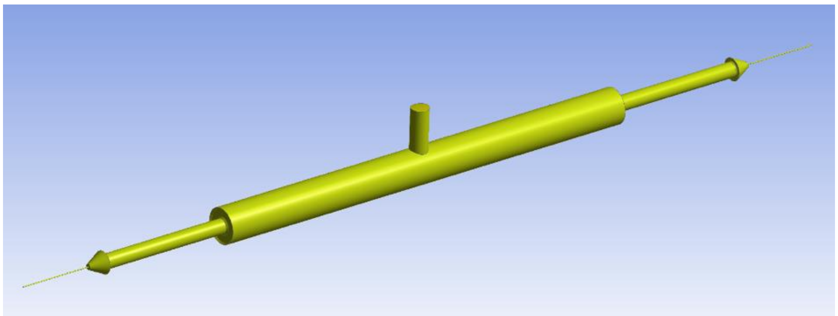

(c)

Figure 4.4: Rotary jet spinneret geometry from (a) the FibeRio L1000-D equipment and (b) its CAD representation; (c) the internal geometry used in the computational fluid dynamics (CFD) simulations.

The experimental parameters used in the simulations were classified as either material parameters (fluid density and viscosity) or CFD solver variables. For simplicity we assumed a Newtonian fluid with a dynamic viscosity η. The CFD solver variables included the device geometry, the atmospheric pressure, the rotational velocity, and the relevant boundary conditions at the inlet, outlet and channel walls. We assumed no-slip at the walls. The inlet and outlet were prescribed as openings, allowing flow in either direction. The geometry was set to rotate around an axis about the centre of the spinneret at rotational velocities ranging from 5,000 to 12,000 rpm, ensuring that a centrifugal force was generated during the simulations. Higher rotational velocities were used to adequately simulate practical capabilities in the lab scale RJS machine.

The flow variables of interest were the shear rate profile within the die section of the spinneret, the fluid velocity within the die and the volumetric flow rate. A series of CFD simulations were performed for Newtonian fluids with η equal to 1, 5, 10, 15, 20, 25 and 30 Pa.s. The rotational velocity in each simulation was varied between

5,000 and 12,000 revolutions per minute, in steps of 1,000 revolutions per minute. To explore a reasonably large parameter space, we carried out 56 simulations for different combinations of viscosities and rotational velocities.

Flow visualizations are useful in determining the effect of the spinneret geometry on the flow behaviour, for example the effect of sudden restrictions on the flow variables. Flow visualizations are displayed in Figure 4.5 to Figure 4.8 to illustrate the distribution of pressure and shear rates during spinning. To reduce the computational time, all simulations were run using the steady state solver. Thus, the results are representative of the flow behaviour when all transient effects have died out.

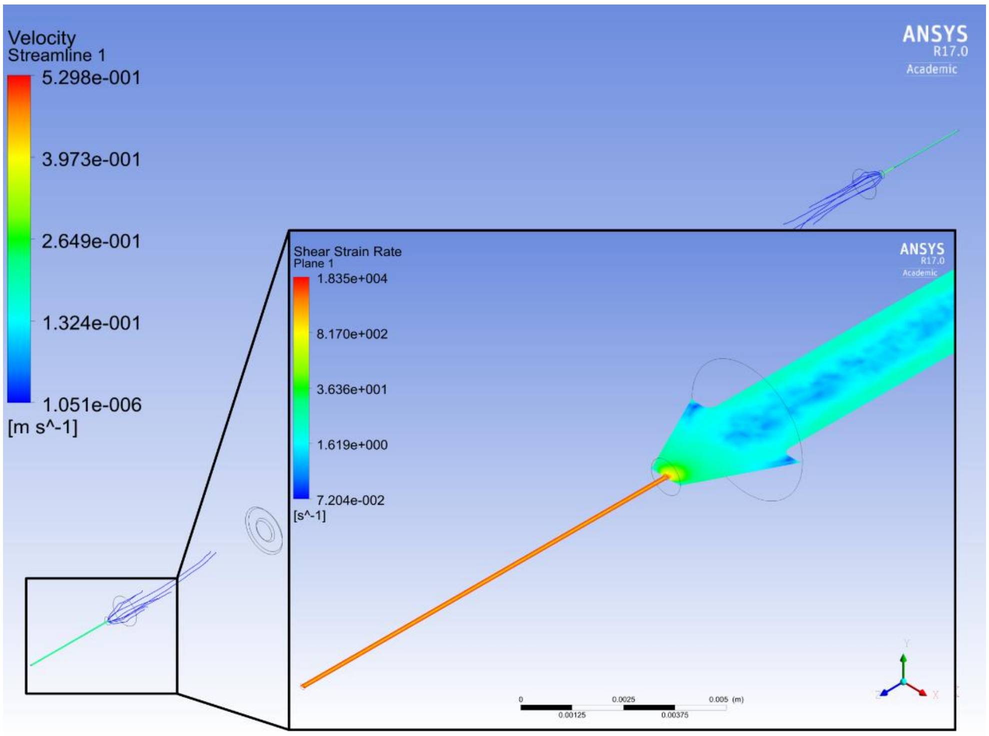

Figure 4.5: Simulated flow distribution within the spinneret for a viscosity of η *=1 Pa.s and rotation rate of 10,000 rpm (assuming Newtonian fluid). The streamline colour scale represents the velocity magnitude. Moving from the spinneret to the needle the fluid velocity increases from about* 10^{-6} *ms*$^{-1}$ *to 0.5 ms*$^{-1}$*. The inset shows the shear rate distribution. Within the spinneret, the shear rate is highest near the wall, as expected from a Poiseuille flow distribution.*

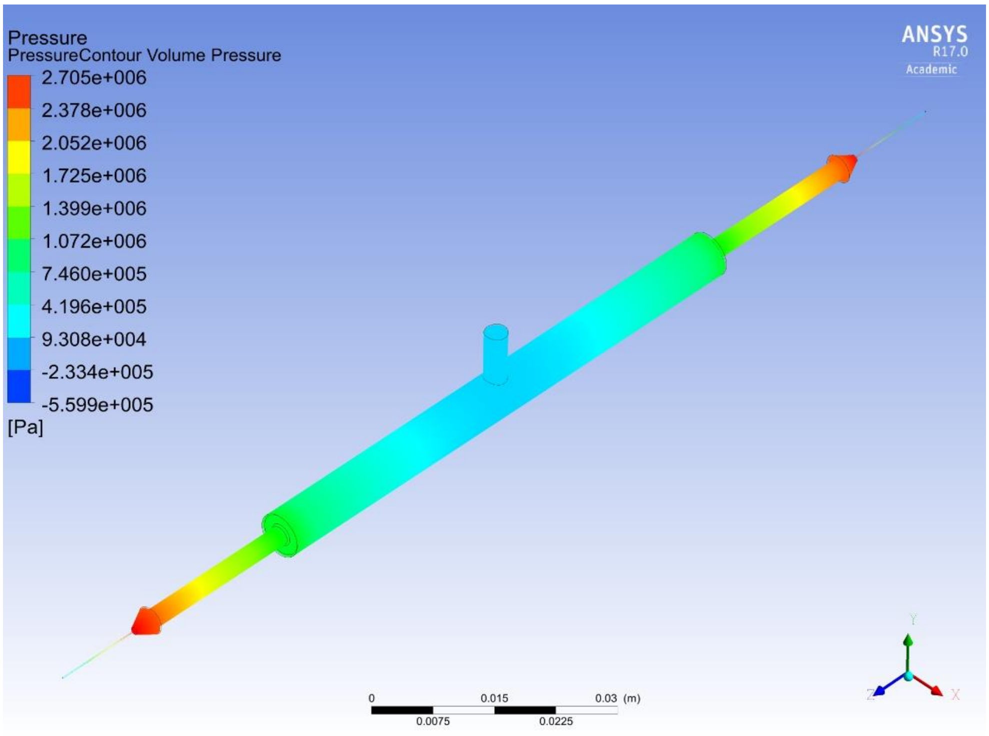

Figure 4.6: Pressure distribution within the spinneret for η =10 Pa.s and rotation rate 10,000 rpm. The pressure is seen to increase approximately linearly from the centre of rotation to the entry of the needle. After the fluid has passed this point, the pressure decreases along the die length to reach atmospheric pressure.

The shear stain rate illustrated by the inset of Figure 4.5 is calculated by the simulation in terms of a theoretical value, measuring a maximum of around 1835 s^{-1}. In our practical rheology testing, using a plate-plate rheometer, it was not possible to measure such high shear rates due to the limitations of this machine. Instead a capillary rheometer would be more suited to understanding the flow behaviour at such high shear rates, and has been noted as a limitation of the ability to directly model the required viscosity properties accurately.

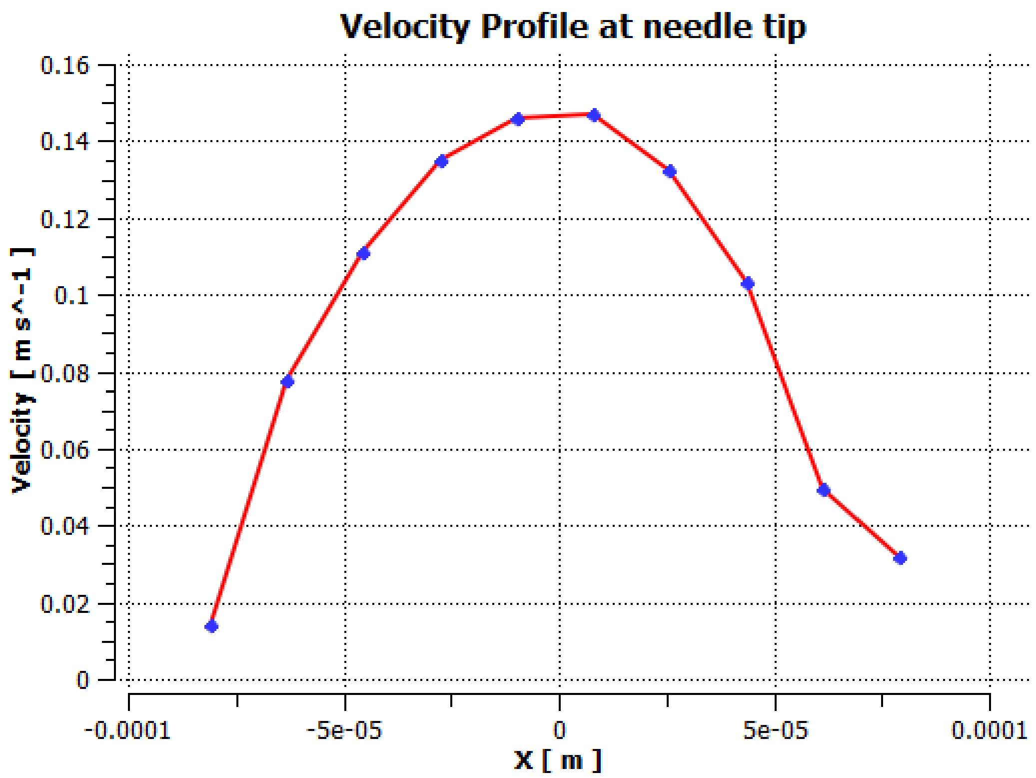

Figure 4.7: Velocity profile at the tip of the needle as the Newtonian solution flows, showing Poiseuille flow.

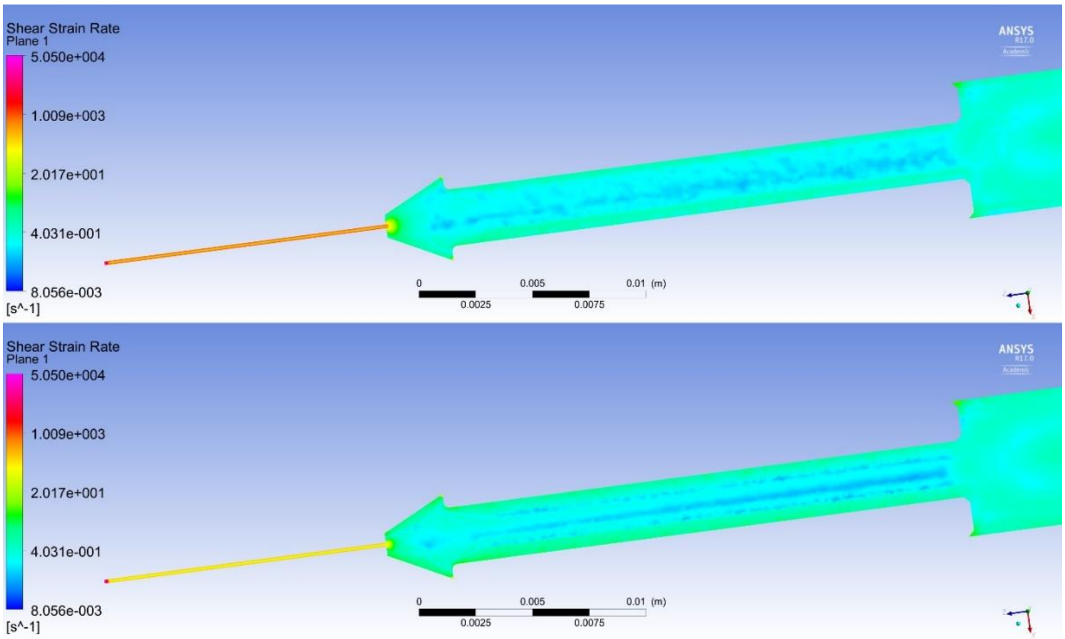

Figure 4.8: Simulated shear rate distribution for η =10 Pa.s and rotation rates 10,000 rpm (top) and 5,000 rpm (bottom). The shear rate magnitude increases due to the higher centrifugal forces produced by the faster rotation. The highest shear rates occur in the region where the polymer exits the die.

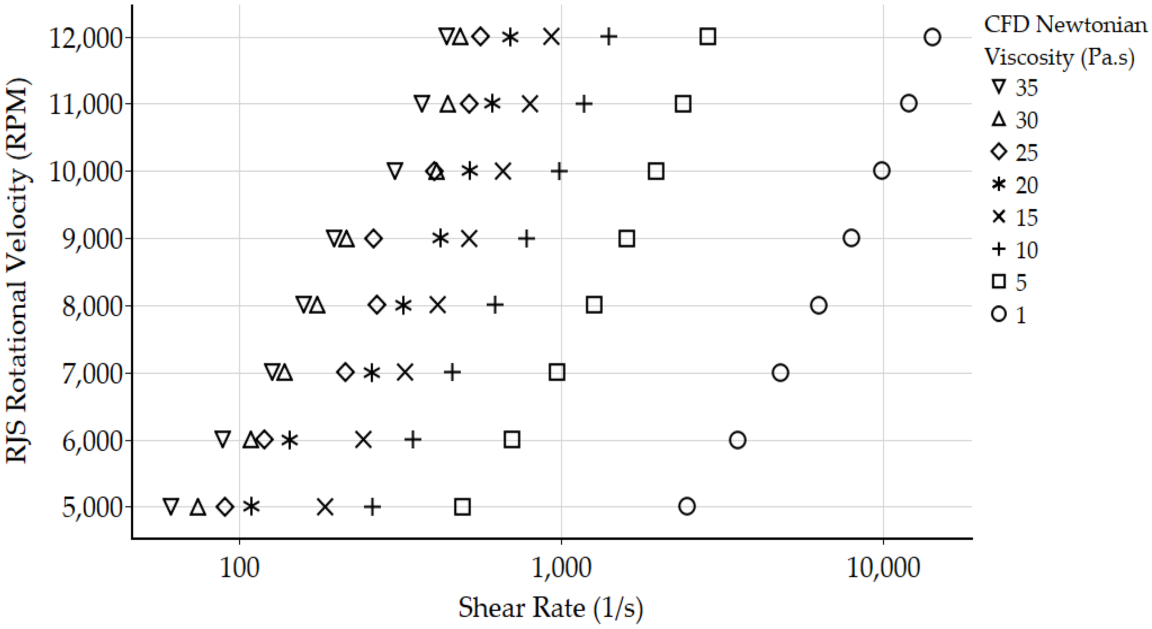

Figure 4.9: Highest shear rates from CFD simulations, using rotational velocities between 5,000 and 12,000 rpm. As expected, an increase in shear rates are observed for lower viscosities.

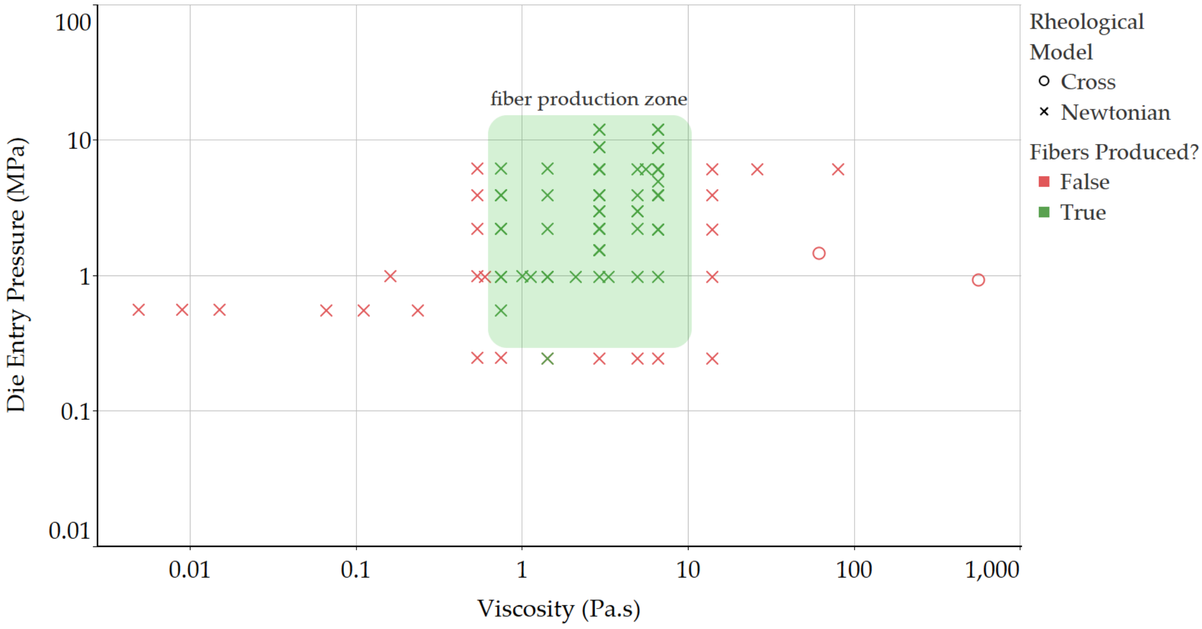

Figure 4.10: Pressure at the entry of the die versus fluid viscosity. Viscosity is evaluated at shear rate values that correspond to the entrance of the die region. The graph includes data for both fibre producing polymer systems (green symbols within green shaded area) and non-fibre producing polymer systems (red symbols). The green shaded area indicates the range of

pressures and viscosities for which a fibre is produced. Too low pressure or too high viscosity will not enable the polymer to flow.

4.2.4 Rotary jet spinning trials

To evaluate the ability of the various polymer solutions and melts to be spun into fibres, RJS was performed using the materials specified in Table 4.1 and Table 4.2. Polymers intended for melt spinning were used as is in sample quantities of 100 mg per spin, with solution spinning performed with a volume of 1 ml per spin.

RJS experiments were conducted using each solution or melt, with the outcome recorded to produce a graph showing the zones where successful fibre production occurred. A measure of the driving force for fibre production is the pressure exerted on the polymer as it approaches the die constriction. The reduction in the cross-sectional area results in an increase in the shear rate due to the increased flow velocity and reduction in length. A larger shear rate in turn leads to reductions in viscosity at these locations for non-Newtonian flows.

The pressure at the entry to the die was calculated from the CFD simulation to evaluate the rotational velocity and material density required for RJS to produce a fibre. The pressure due to centrifugal forces acting on the die can be calculated from:

$$P = \rho \Omega^2 S_0^2 \tag{4.4}$$

where ρ is density, Ω is rotational velocity (rad/s) and S_0 is the distance from the centre of rotation to the entry of the die.

The CFD simulations require the prescription of a Newtonian viscosity, which should be representative of the non-Newtonian viscosity evaluated at relevant shear rates. Based upon the data presented in Figure 4.9, the viscosity of each non-Newtonian polymer was evaluated at typical RJS shear rates between 500 s^{-1} and 800 s^{-1}. For the analysis, an average of these apparent viscosity values was used. The pressure at the die entry (as calculated from equation 4.4) either forces the polymer through the spinneret or results in a blockage, as observed during RJS experimentation and labelled in Figure 4.10. This effect is either due to insufficient pressure at the die entry or to the polymer being too viscous. By comparing the pressure and viscosity, a direct comparison can be made regardless of the polymer or spinneret geometry.

Figure 4.10 shows a comparison of die entry pressure and viscosity values from experimental trials using the polymer systems of Table 4.1 and Table 4.2. For a 0.16 mm internal diameter die, the data suggests a fibre producing zone (shaded green zone) where the viscosity (at shear rates of about 800 s^{-1}) should be between 0.9 Pa.s and 10 Pa.s.

Fibre production as indicated in Figure 4.10 does not solely rely on the ability of the polymer solution or melt to flow through the die. Fibre production will also rely on polymer solidification, be that through solvent evaporation or cooling of a polymer melt. In the fast-flowing air of the rotary jet spinning chamber, the rate at which solidification can happen is affected by several factors such as chamber temperature, solvent volatility, solution viscosity and spinning velocity [20]. Once a fibre has left the spinneret, the fibre is drawn due to the continual motion of the rotating spinneret and the rapid deceleration of the extrudate which is anchored by the continuous connectivity of the fibre to the collector.

Mellado et al. [13] produced the following estimate of the fibre radius based on the polymer viscosity and processing parameters:

$$r = \frac{aU^{1/2}\nu^{1/2}}{R_c^{3/2}\Omega} \tag{4.5}$$

where a is the diameter of the die (m), U is the velocity of the flow from the die exit (m/s), ν is the kinematic viscosity $\left(\eta/\rho\right)$, R_c is the collector radius (m) and Ω is the rotational velocity (rad/s). We have evaluated the ability of equation 4.5 to describe our experimental data, focusing on solution spun PA6 fibre diameter data.

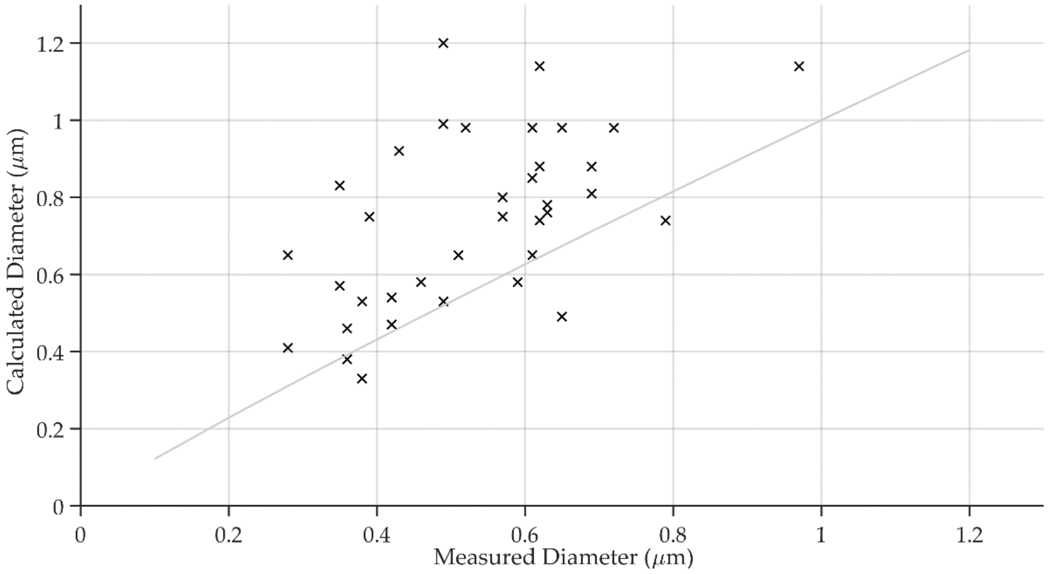

Figure 4.11: Fibre diameter comparison between Mellado et al. [13] model (line) and measured fibre diameter data. The variation in fibre diameter signifies a less than perfect fit. Alternative tests in melt spinning showed even greater disparity, confirming the need for additional parameters to be considered.

In Figure 4.11, the model by Mellado et al. is compared to data on rotary jet spun fibres produced using PA6 solutions only. Our experimental data showed relatively large scatter, and as a result a greater than expected variance with respect to model predictions. The model could be improved by considering additional effects such as solvent evaporation. Additional data, from solutions containing solvents with higher volatilities and fibre diameters from melt spinning showed even more scatter than Figure 4.11. For example, diameters for melt spun PE (M_w – 8,000 g/mol) averaged 11 μm, while the model by Mellado et al. predicts 1.1 μm.

4.3 Discussion

In this study we investigated rotary jet spinning as a method of fibre production and attempted to discover the lower and upper limits of solution or melt viscosities that would facilitate successful fibre production. The materials chosen for the trials varied in molecular weight and polymer concentration in solution, in the hope that variations in system viscosities and flow behaviours from Newtonian to non-Newtonian would produce differing results, to be analysed for their impact on fibre spinning.

It was shown that all investigated PA6 solutions showed mostly Newtonian behaviour (see Figure 4.2), while PE's of higher molecular weight exhibited non-Newtonian behaviour (see Figure 4.1). To establish spinnability, experimental trials were performed using each of the polymer systems (see Table 4.1, and Table 4.2) with varying rotational velocities to establish their potential for fibre production. In addition to experimental data, computational fluid dynamics (CFD) was performed using a broadly similar range of Newtonian viscosity values.

The CFD results demonstrated the flow behaviour within the geometry at various rotational velocities. Flow evaluation variables included the flow velocity and shear rates at varying positions within the geometry. Figure 4.5 to Figure 4.8 showed visualizations of the flow behaviour. From these images we can see that at the entry to the die an area of rapidly increasing flow velocity is present due to a sudden decrease in cross-sectional area. Correspondingly, there is a rapid increase in shear rate. It is at this location that polymers which exhibit very high viscosities (above 10 Pa.s at shear rate ~800 s^{-1}) seem to block the channel. The pressure and shear rate comparison are illustrated in Figure 4.6 and Figure 4.8 respectively, showing that maximum pressure exists at the entry to the die, with shear rates that increase as the rotation rate is increased from 5,000 to 10,000 rpm.

Having gained some insight into the flow behaviour from the CFD analysis, experimental trials were then conducted for model validation. During RJS, polymer systems that blocked the die channel or flowed through but created droplets on the collector were marked as failures, as continuous, bead-free fibres were not produced. These unsuccessful spinning experiments would form the basis of the lower and upper viscosity limits of the trial. Following this, pressure calculations were made for each respective trial and compared against the viscosity of the polymer at shear rates (~800 s^{-1}) that would be experienced during spinning. The data as shown in Figure 4.10 represents the outcome of the spinning limitation study that we set out to do. In this graph we showed that polymers with a viscosity below ~1 Pa.s did not produce fibres due to insufficient chain entanglement in either polymer melt or solution. On the other hand, for polymers with viscosities exceeding ~10 Pa.s we experienced blockage in the spinneret as discussed.

In future it is worth considering the evaporation mechanism of polymer solutions during spinning. Polymer solutions contain a solvent which is required to evaporate during spinning to produce a fibre. In case of a too volatile solvent, the fast-moving air in the spinning chamber will start to solidify the polymer leaving the tip of the die before it gets a chance to extrude, causing a blockage. Conversely, if the solvent has a too low volatility and does not readily evaporate through exposure to fast flowing air, the polymer fibre will be heavily beaded upon collection. This could therefore lead to solutions with shear viscosities outside the processing window that has been suggested here, for example solutions based on rapidly evaporating solvents could have a shear viscosity below 1 Pa.s and still produce fibres.

Die entry pressures increase through a change in geometry, rotational velocity or the addition of an external pressure coupling, such as in the pressurized gyration process [21-23]. A combination of any of these modifications could potentially widen the overall range of fibre producing viscosities. As shown in our data, the pressure at which a polymer starts to extrude from a 0.16 μm diameter die exceeds 400 kPa.

Further research into the model could include variations of die geometries and die channel lengths which would allow for much higher pressures, and therefore viscosities, to produce fibres. Reducing the channel length will reduce the pressure required to extrude the polymer in addition to a variation in the radius of the spinneret, which would increase die entry pressure for larger radius geometries. Directions for further research could also include reduction and recovery of solvents in solution spinning or spinning of higher molecular weight polymer melts, allowing for enhanced mechanical performance over existing polymer melt options.

4.4 Conclusions

Rotary jet spinning (RJS) was investigated for the analysis of rheological material limitations. Using computational fluid dynamics (CFD) and physical spinning trials, a viscosity range for spinning was determined. RJS was shown to produce fibres that were continuous and bead-free in the case of Newtonian solutions with viscosities of 1 to 10 Pa.s. In evaluating successful and unsuccessful experimental spinning outcomes, we have produced a region of spinnability that has not yet been reported. From this region, the pressure and viscosity ranges that show successful fibre production from a specific die geometry were identified. Newtonian flow behaviour is most suited to RJS, however high shear rates of around 800 s^{-1} are operative in the process, which opens up possibilities for shear thinning non-Newtonian fluids with low enough viscosities at these shear rates. Further considerations are necessary to evaluate the impact of solution evaporation rates and polymer melt temperature on the production of fibres by RJS.

References

1. Ren, L., et al., *Large-scale and highly efficient synthesis of micro- and nano-fibers with controlled fiber morphology by centrifugal jet spinning for tissue regeneration.* Nanoscale, 2013. **5**(6): p. 2337-45.
2. Zimm, B.H., *Dynamics of Polymer Molecules in Dilute Solution: Viscoelasticity, Flow Birefringence and Dielectric Loss.* The Journal of Chemical Physics, 1956. **24**(2): p. 269-278.
3. Rouse, P.E., *A Theory of the Linear Viscoelastic Properties of Dilute Solutions of Coiling Polymers.* The Journal of Chemical Physics, 1953. **21**(7): p. 1272-1280.
4. Teraoka, I., *Models of Polymer Chains*, in *Polymer Solutions: An Introduction to Physical Properties*. 2002, John Wiley & Sons, Inc. p. 64-65.
5. Lu, Y., et al., *Parameter study and characterization for polyacrylonitrile nanofibers fabricated via centrifugal spinning process.* European Polymer Journal, 2013. **49**(12): p. 3834-3845.
6. Fox, T.G. and P.J. Flory, *Further Studies on the Melt Viscosity of Polyisobutylene.* The Journal of Physical Chemistry, 1951. **55**(2): p. 221-234.
7. Colby, R.H., L.J. Fetters, and W.W. Graessley, *The melt viscosity-molecular weight relationship for linear polymers.* Macromolecules, 1987. **20**(9): p. 2226-2237.
8. Vega, J.F., et al., *Rheology and reptation of linear polymers. Ultrahigh molecular weight chain dynamics in the melt.* Journal of Rheology, 2004. **48**(3): p. 663-678.
9. Yan, D., W.J. Wang, and S. Zhu, *Effect of long chain branching on rheological properties of metallocene polyethylene.* Polymer, 1999. **40**(7): p. 1737-1744.
10. Vega, J.F., et al., *Rheological criteria to characterize metallocene catalyzed polyethylenes.* Macromolecular Chemistry and Physics, 1999. **200**(10): p. 2257-2268.
11. Shenoy, S.L., et al., *Role of chain entanglements on fiber formation during electrospinning of polymer solutions: good solvent, non-specific polymer–polymer interaction limit.* Polymer, 2005. **46**(10): p. 3372-3384.
12. McKinley, G.H. and T. Sridhar, *Filament-Stretching Rheometry of Complex Fluids.* Annual Review of Fluid Mechanics, 2002. **34**(1): p. 375-415.
13. Mellado, P., et al., *A simple model for nanofiber formation by rotary jet-spinning.* Applied Physics Letters, 2011. **99**(20): p. 203107.
14. Padron, S., D.I. Caruntu, and K. Lozano, *On 2d Forcespinning (Tm) Modeling.* Proceedings of the Asme International Mechanical Engineering Congress and Exposition, 2011, Vol 7, Pts A and B, 2012: p. 821-830.
15. Padron, S., et al., *Influence of Viscosity on Forcespinning™ Dynamics.* International Mechanical Engineering Congress and Exposition - 2012, Vol 4, Pts A and B, 2013: p. 889-893.
16. Taghavi, S.M. and R.G. Larson, *Regularized thin-fiber model for nanofiber formation by centrifugal spinning.* Phys Rev E Stat Nonlin Soft Matter Phys, 2014. **89**(2): p. 023011.
17. Noroozi, S., et al., *Regularized string model for nanofibre formation in centrifugal spinning methods.* Journal of Fluid Mechanics, 2017. **822**: p. 202-234.

18. Divvela, M.J., et al., *Discretized modeling for centrifugal spinning of viscoelastic liquids.* Journal of Non-Newtonian Fluid Mechanics, 2017. **247**: p. 62-77.
19. Osswald, T. and N. Rudolph, *Polymer Rheology Fundamentals and Applications*. 2014: Carl Hanser Verlag GmbH & Co. KG.
20. Golecki, H.M., et al., *Effect of Solvent Evaporation on Fiber Morphology in Rotary Jet Spinning.* Langmuir, 2014. **30**(44): p. 13369-13374.
21. Mahalingam, S. and M. Edirisinghe, *Forming of polymer nanofibers by a pressurised gyration process.* Macromol Rapid Commun, 2013. **34**(14): p. 1134-9.
22. Mahalingam, S., et al., *Facile one-pot formation of ceramic fibres from preceramic polymers by pressurised gyration.* Ceramics International, 2015. **41**(4): p. 6067-6073.
23. Mahalingam, S., G. Ren, and M. Edirisinghe, *Rheology and pressurised gyration of starch and starch-loaded poly(ethylene oxide).* Carbohydr Polym, 2014. **114**: p. 279-87.

5

Polymer Derived Ceramic Fibres by Rotary Jet Spinning

5.1 Introduction

Thus far, rotary jet spinning has shown us that it is comparable to other polymer fibre production methods such as electrospinning and melt blowing in terms of size and volume production, which combine benefits from other processes to produce small fibre diameters and the relatively high-volume output.

We have already evaluated the ability of the rotary jet spinning (RJS) process to create high strength and modulus polymer fibres by means of imidization, when all other options were not available. However, we could potentially also produce high modulus and strength fibres in the form of inorganic ceramic or glass fibres, should we find a suitable preceramic polymeric material to process using RJS.

Inorganic fibres have shown to provide beneficial properties such as a high strength and thermo-chemical resistance in applications such as ceramic matrix composites [1], high temperature air filtration [2], and even biomedical applications using biocompatible ceramics such as 45S5 Bioglass® [3, 4].

Electrospinning has been widely used in the past to produce preceramic fibres [5, 6] but has recently been joined by RJS. Preceramic polymers are processable using methods that are not suitable to ceramic materials, requiring an additional transformation step to convert them to ceramics once processed. Glass ceramic (SiOC) fibres produced from electrospinning were reported by Guo et al. in which fibre diameters as low as 1.65 μm were reported [7]. Production rates approaching 50 times greater are seen when comparing commercially available electrospinning versus rotary jet spinning machines as discussed in 1. In demonstrating the capability of RJS to produce preceramic fibres, Ren et al. created multilevel structured silica micro/nanofibres with tuned porosity and hollow internal structures [8]. Other studies by Muller et al. [9] and Salinas et al. [10, 11] have also successfully utilised the RJS method.

Ceramic fibres are made using the polymer derived ceramic (PDC) route, in which precursors such as polysilanes, polycarbosilanes, polysiloxanes, polysilazanes, and polysilylcarbodiimides enable the production of nanostructured SiC, SiOC, and SiCN ceramics via a thermal conversion step in an inert atmosphere [12].

The manufacturing process from preceramic polymers to ceramic fibre relies on a four-step sequence for which each step has a specific requirement. These include 1) the synthesis of preceramic polymers from molecular precursors, 2) spinning of the polymer through one of several methods, 3) crosslinking of green fibres if not already crosslinked from solution, and lastly 4) the pyrolysis of crosslinked fibres to produce ceramic fibres [5]. Various ways exist to render the crosslinked pre-pyrolised fibres, for example the use of gamma-rays or electronic irradiation causing radical reactions, or through ammonia-curing [13].

Mahalingam et al. [14] demonstrated this concept using a facile one-pot formation of ceramic fibres from preceramic polymers by pressured rotary jet spinning in which a binary solvent system was used with the addition of polyvinylpyrrolidone (PVP) to aid with the fibre generation process. Pressurised rotary jet spinning is the same as RJS, however an additional pressure coupling is installed to enable the increase in pressure during spinning. In their research, they successfully created preceramic fibres and converted them to ceramic fibres, having diameters between 10 and 50 μm.

In this research, we aimed to produce preceramic fibres with the smallest diameters possible by trialling both melt and solution RJS. We preferred not to use a sacrificial polymer such as PVP but opted to include it as a comparison for the rheological variation it would provide in solution spinning. Once preceramic fibres were produced, they were characterised according to size, before conversion to ceramic fibre by means of pyrolysis.

5.2 Experimental

5.2.1 Materials

A commercially available silicone resin (Silres MK®, M_w = 9,400 g.mol^{-1}, Wacker-Chemie GmbH, Munchen, Germany) was used as the preceramic precursor, with the chemical structure shown in Figure 5.1. Polyvinylpyrrolidone (PVP, M_w = 1,300,00 g.mol^{-1}, Sigma Aldrich, Poole, UK) was used as an additive to alter the rheological properties of one of our solutions, where it was used as a sacrificial polymer. Chloroform, N,N-Dimethylformamide (DMF), and acetone (Sigma Aldrich, Poole, UK) were used as solvents in the preparation of the spinning solutions. An organotin compound dibutyltin dilaurate (Sigma Aldrich, Poole, UK) was used as the catalyst for crosslinking solutions, while ammonia (Sigma Aldrich, Poole, UK) was used as catalyst for melt spun fibres.

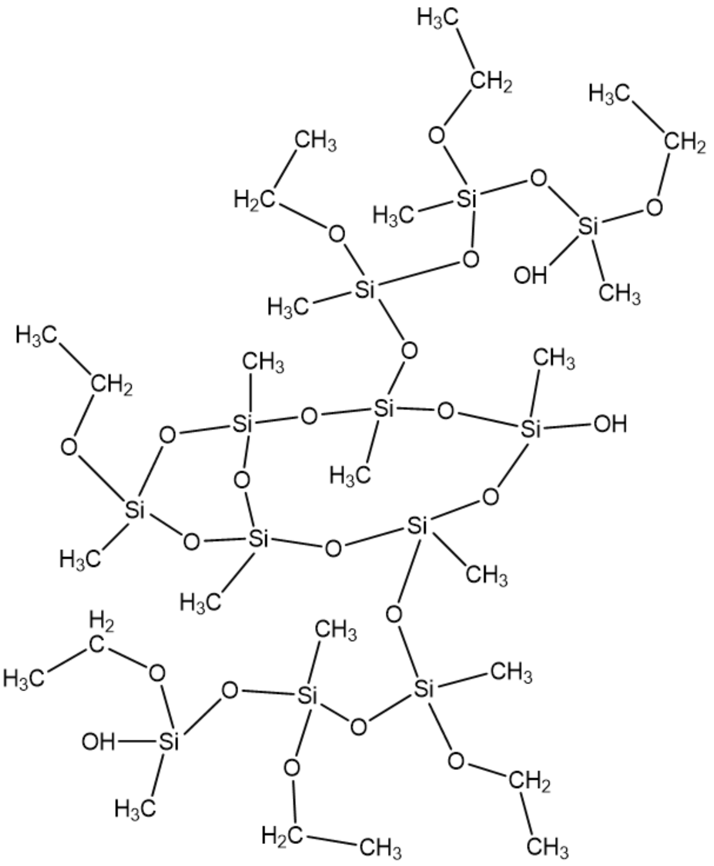

Figure 5.1: Chemical structure of polysiloxane used (Silres MK®), showing the partial cage structure. Crosslinking catalysts such as ammonia (NH_3) or dibutyltin dilaurate ($C_{32}H_{64}O_4Sn$) were used to produce ceramic fibre.

5.2.2 Solution preparation and rheology

As previously discussed in Chapter 4, the required shear viscosity for successful rotary jet spinning is predicted to be about 1-12 Pa.s. This is typically from a Newtonian fluid, although non-Newtonian fluids which have apparent shear viscosities in this region between the shear rates of 500 – 800 s^{-1} could also be trialled.

To investigate preceramic fibre production we prepared three solutions, one using acetone, and two more using a chloroform/dimethylformamide combination with one containing polyvinylpyrrolidone (PVP). Solutions were prepared as per Table 5.1 (5-8), where upon combining solvent and polymer, the solutions were stirred for between 24-48 hours to ensure solution homogeneity.

A binary solvent system was trialled in which a 1:1 ratio of chloroform and dimethylformamide was used in solutions 7 and 8 (see Table 5.1). One primary solvent system was also used in which acetone was also trialled as it showed good solubility. The variation of the solvent systems allowed the volatility of the solvents to be evaluated.

Melt RJS was also conducted due to a relatively low (55°C) melting temperature of the silicon resin. Using this combination of fibre solutions and melts allowed the investigation of the morphology from either solvent evaporation or melt cooling. The two solvent systems are also beneficial in allowing the volatility of the specific solvents to influence solvent evaporation, and hence fibre diameter.

Plate-plate rheometry was conducted as per Figure 5.2 using a TA Instruments AR2000 rheometer fitted with an environmental chamber for the melt rheology, and Peltier plate for the solution rheology.

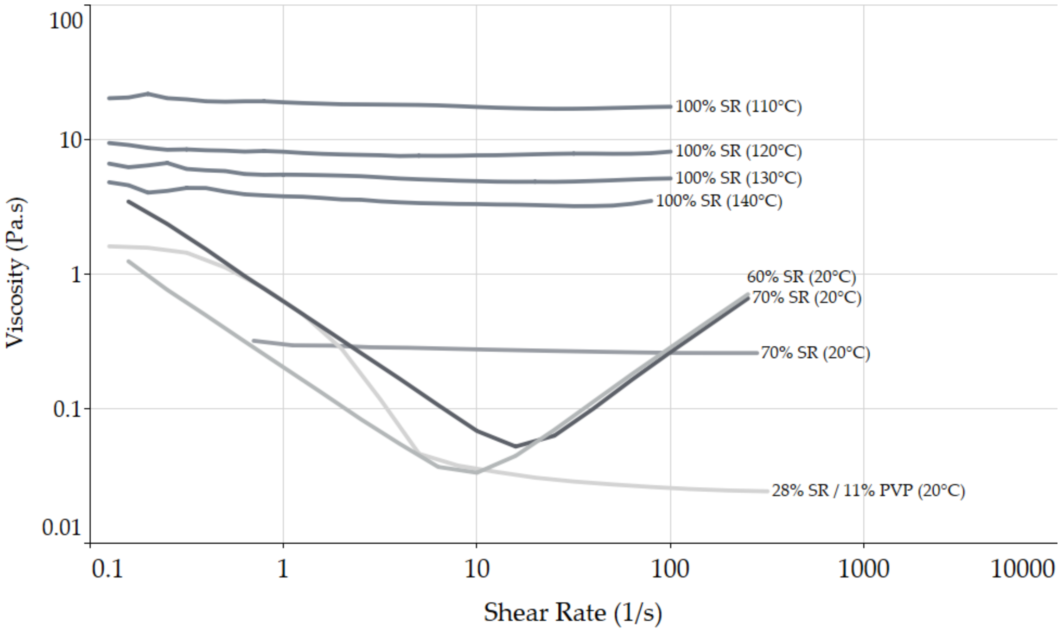

Figure 5.2: Shear viscosity of ceramic precursor (Silres MK®) solutions and melts at the temperatures used for fibre spinning. Melt rheology shows Newtonian flow behaviour whereas solutions demonstrate shear thinning as well as shear thickening due to solvent (acetone) evaporation during rheological testing.

From the rheological data shown, the 60 wt.% and 70 wt.% polymer solutions (Silres MK®/acetone) show complex behaviour, possibly due to the volatility of acetone. It has the fastest evaporation rate between all solvents used, which during rheological tests could not successfully be compensated for over the test duration due to the rapid solvent evaporation, even when fitted with a solvent trap to reduce evaporation rate.

Table 5.1: List of solution and melt combinations used in rotary jet spinning, with processing temperature and apparent viscosity at the shear rate range (500 – 800 s^{-1}) of fibre production.

#	**Polymer(s)**	**Solvent**	**Temp. (°C)**	**Apparent viscosity (Pa.s)**
1	Silres MK	None (Melt)	110	17.5
2	Silres MK	None (Melt)	120	8.2
3	Silres MK	None (Melt)	130	5.1
4	Silres MK	None (Melt)	140	3.5
5	Silres MK (60 wt.%)	Acetone	20	~1-5
6	Silres MK (70 wt.%)	Acetone	20	~1-5
7	Silres MK (70 wt.%)	Chloroform/Dimethylformamide	20	0.26
8	Silres MK (28 wt.%) PVP (11 wt.%)	Chloroform/Dimethylformamide	20	0.02

5.2.3 Rotary jet spinning

Preceramic fibres were produced via rotary jet spinning for both melt and solutions, using a FibeRio Cyclone L1000D Forcespinner® attached with spinnerets having exit die diameters of 0.16 μm. Fibres were collected at a radius of 25 cm using vertical collector bars arranged in equal radial spacing around the spinneret. The rotational velocity was varied between runs to determine optimum fibre production, having the capability of rotational velocities between 1,000 and 15,000 rpm. During melt spinning, the mass of polymer resin used in each spin varied between 0.5 g and 1.0 g, whereas the solution spinning volume was a constant 1 ml due to the size of the spinneret tank.

5.2.4 Morphology

The fibre diameters were evaluated using a Jeol JSM-6300F scanning electron microscope (SEM), after being Au coated for 30 s. to prevent charging effects. All imaging samples were then evaluated using ImageJ software to determine the diameter of around 50 to 100 individual fibres per image.

Figure 5.3 shows the fibre diameter histograms with SEM images inserted for all processing variations including melt spinning and solution spinning using the three solution systems.

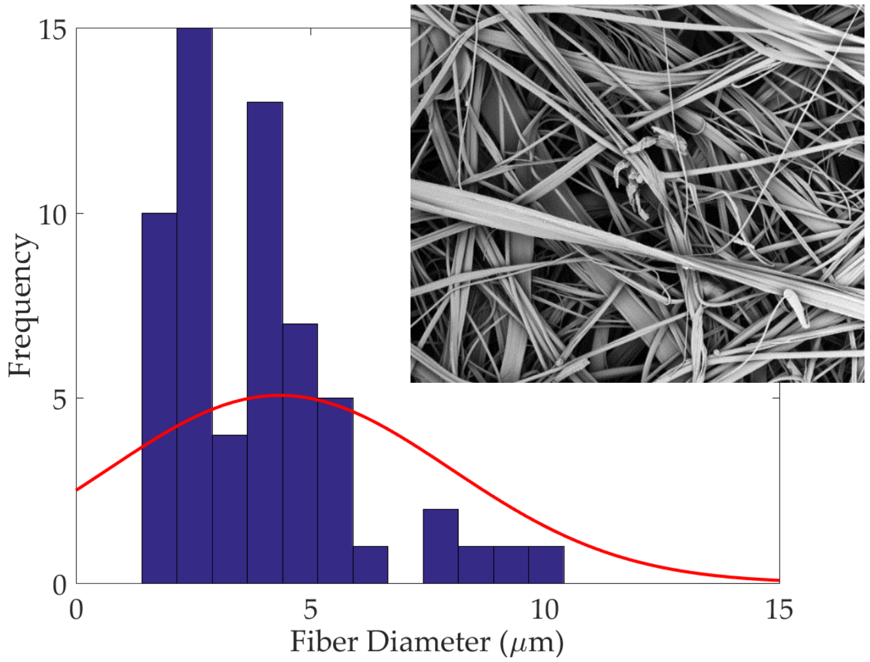

(a)

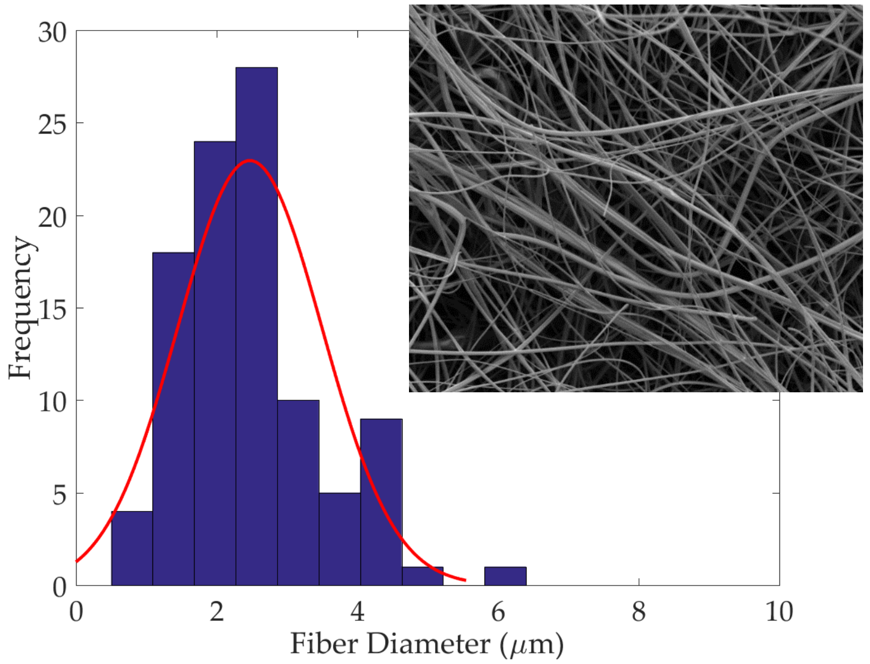

(b)

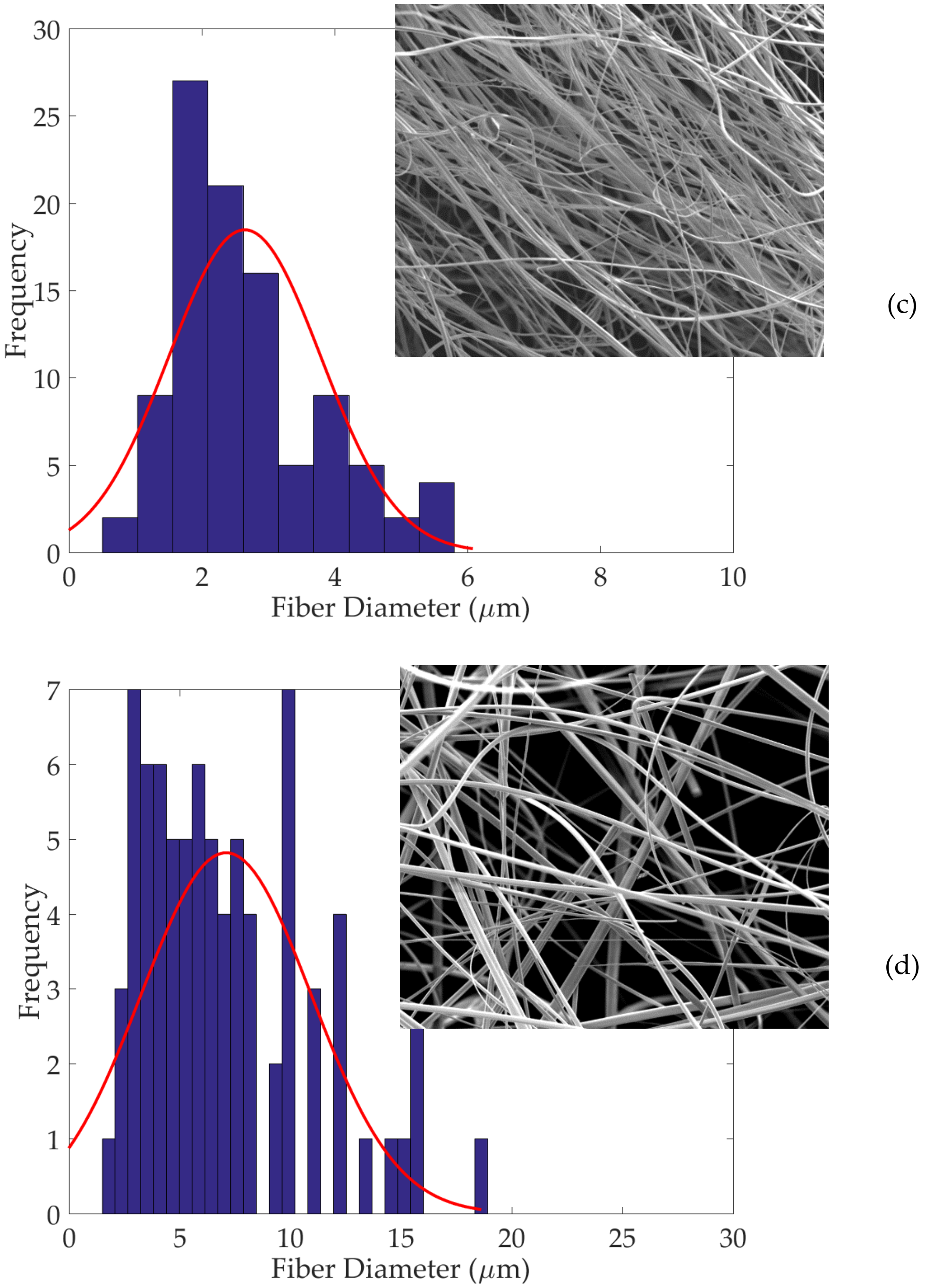

Figure 5.3: Fibre diameter histograms with SEM image insets for the lowest diameters from each experimental group, namely a) melt processing (130°C), b) 70 wt.% Silres in chloroform / dimethylformamide solution, c) 28 wt.% Silres with 11 wt.% PVP in chloroform / dimethylformamide solution, and d) 70 wt.% Silres in acetone solution.

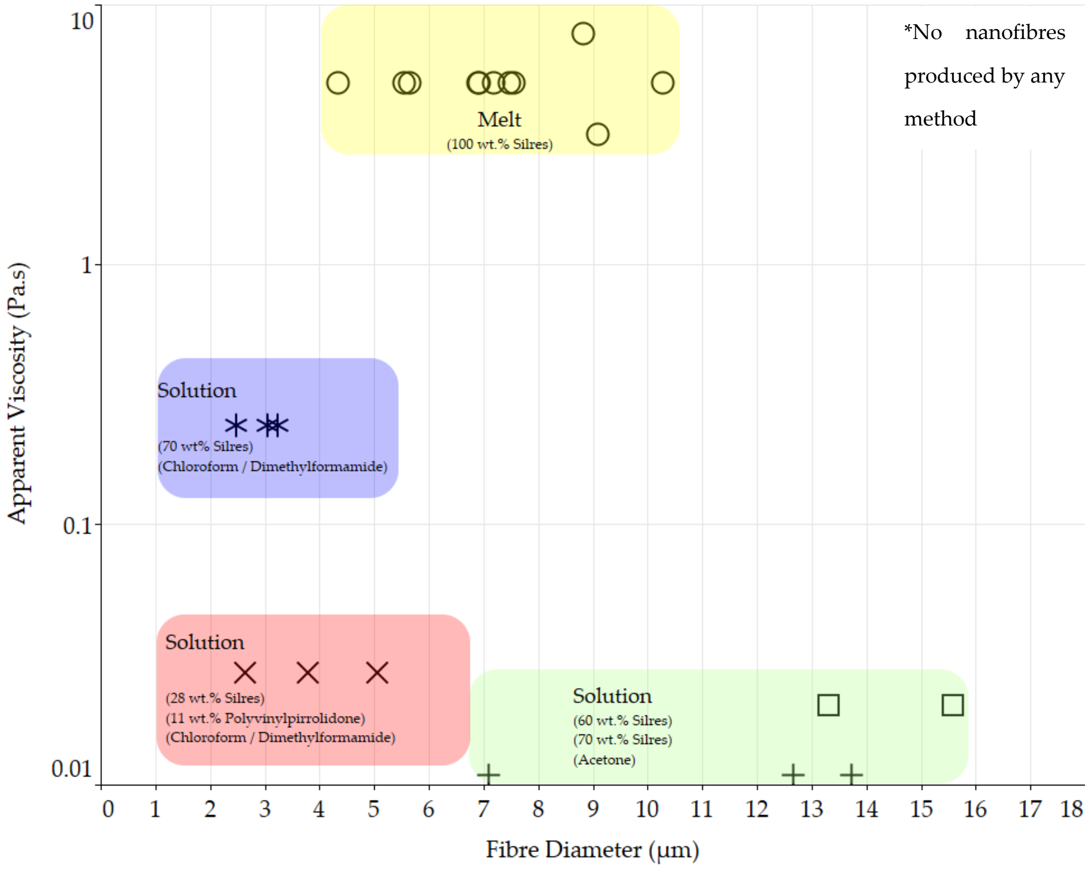

Figure 5.4: Graph showing the fibre diameters produced using each of the four systems trialled. Demarcated zones demonstrate the variability of the fibre diameters based on solvent type and concentration, showing the solvent-based systems producing the smallest fibre sizes.

Table 5.2: Lowest fibre diameter values produced from solutions and melt systems.

#	**Polymer(s)**	**Solvent**	**Temp. (°C)**	**Average diameter (μm)**
3	Silres MK	None (Melt)	130	4.35
6	Silres MK (70 wt.%)	Acetone	20	7.10
7	Silres MK (70 wt.%)	Chloroform / Dimethylformamide	20	2.47
8	Silres MK (28 wt.%) PVP (11 wt.%)	Chloroform / Dimethylformamide	20	2.65

5.2.5 Crosslinking

Fibres produced from the melt did not contain any crosslinker or additive and were therefore required to undergo crosslinking before conversion to ceramic fibres via pyrolysis.

Ammonia was used in a polycondensation reaction at 30 °C using an increasing timescale to establish crosslinking completion times. As-spun fibres were suspended in a covered vessel above a bath of ammonia for 24, 36, 48 and 60 hrs before evaluating the crosslinking reactions. Evaluation was done by placing the fibres in an oven at 200 °C for 1 hour. If the fibres were fused together by examination under an optical microscope, the crosslinking was unsuccessful – see Figure 5.5c. Fibres crosslinked for less than 60 hrs failed through this observational method, providing a required time for successful crosslinking of melt spun fibres at around 60 hrs.

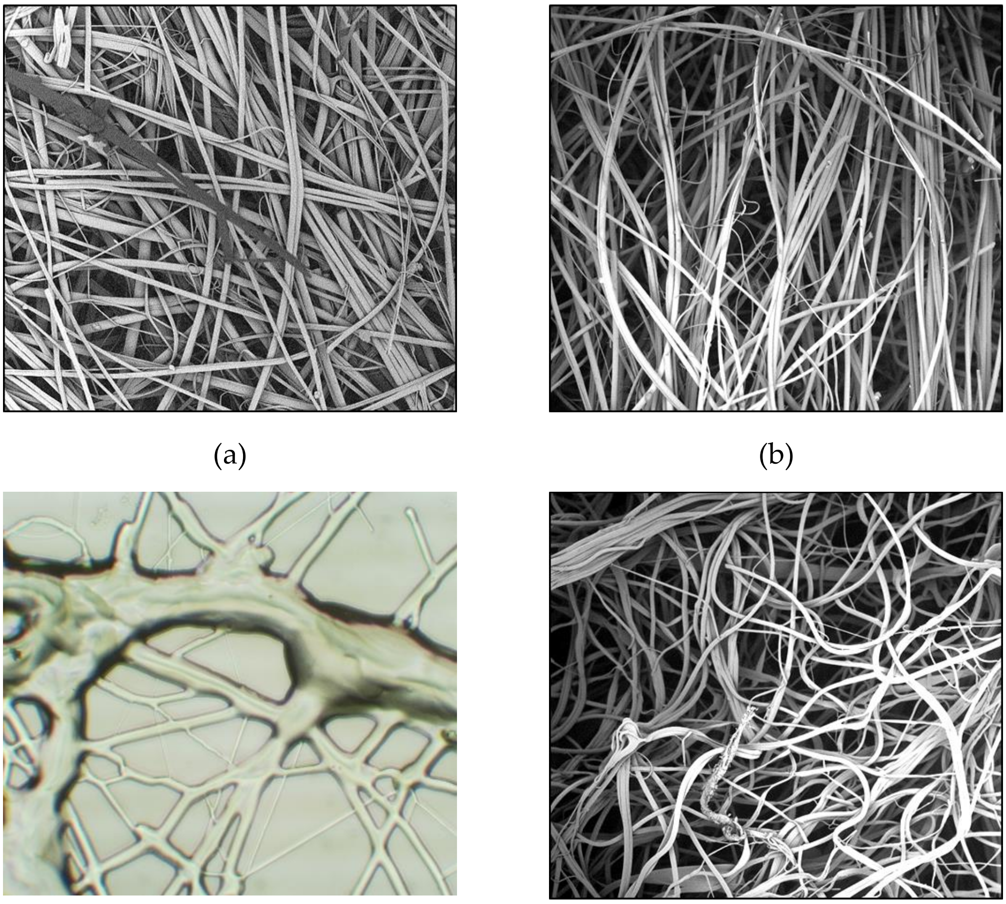

(a) (b)

(c) (d)

Figure 5.5: Crosslinking trials of melt rotary jet spun fibres, showing a) the as spun fibre, b) post crosslinked fibres prior to validation at elevated temperatures, c) unsuccessful crosslinking where all fibres have fused together following heating to 200 °C for 1 hour (crosslinked < 60 hrs), and d) successfully crosslinked and validated fibres following 1 hour at 200 °C (crosslinked > 60 hrs).

Crosslinking of solution spun fibres was conducted using an organotin compound (dibutyltin dilaurate) which was combined with solutions shortly before spinning. As the crosslinking process occurs at room temperature (RT), it is paramount to spin the fibres as quickly as possible to avoid an increase in viscosity, which could in turn lead to larger fibre diameters, or no fibres at all due to blockage of the spinneret.

5.2.6 Pyrolysis

Successfully crosslinked fibres from both melt spinning and solution spinning underwent a pyrolysis process to convert the preceramic fibres into glass ceramic fibres. The pyrolysis process was conducted in a nitrogen atmosphere by placing the fibres within a crucible in a Lenton Tube Furnace as shown in Figure 5.6a. The temperature was increased by 2 °C.min^{-1} to 1000 °C with a dwell time of 1 hour before returning to RT. The fibres were then removed from the furnace (Figure 5.6b) and crucible for analysis using a scanning electron microscope (Figure 5.6c).

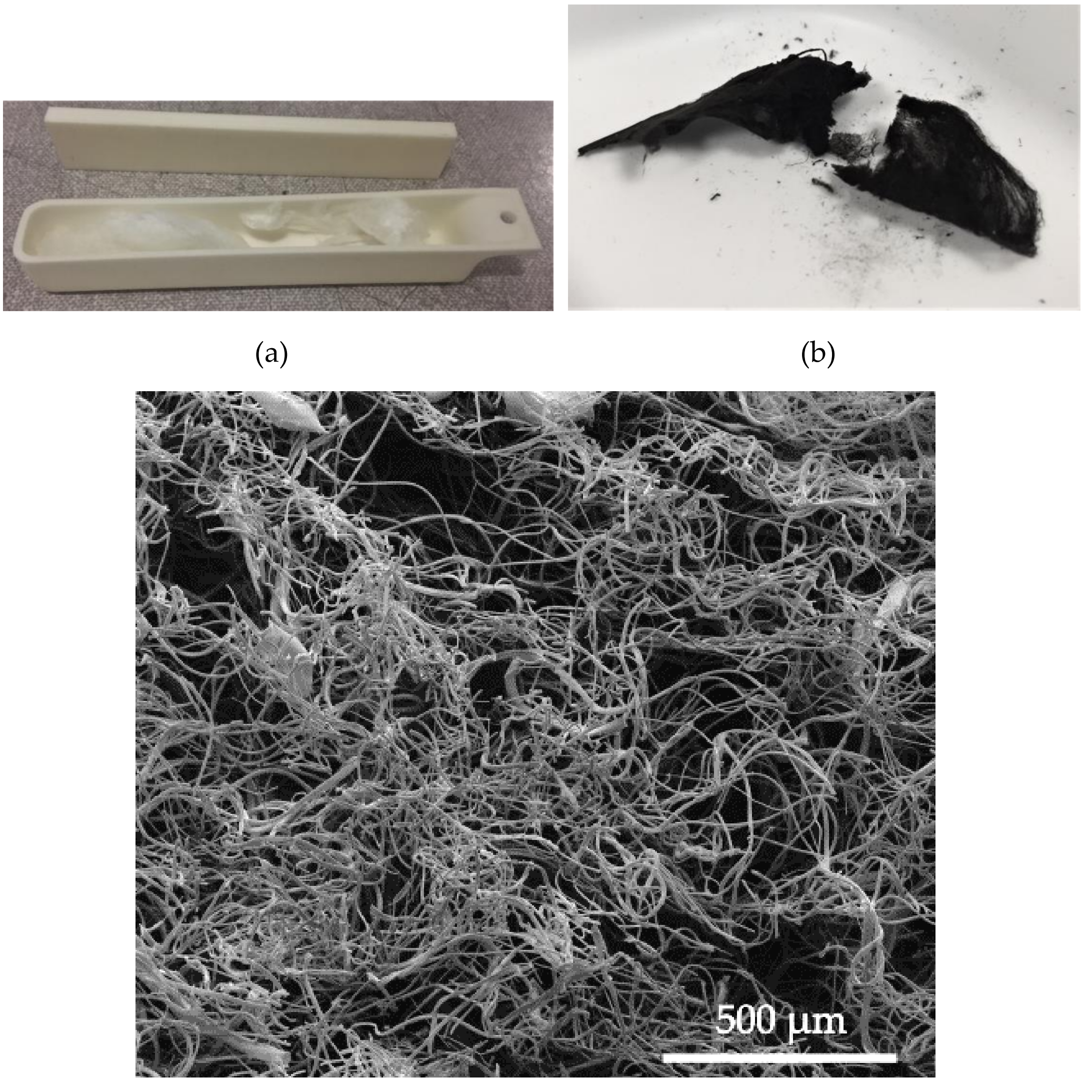

(a) (b)

(c)

Figure 5.6: Images showing a) the preceramic fibre placed in crucible before pyrolysis, b) glass ceramic fibre following pyrolysis, and c) showing an SEM image of the converted glass ceramic fibre where an intact fibre network is visible.

5.3 Discussion

In this study, glass ceramic SiOC fibres were produced by means of rotary jet spinning. A polysiloxane preceramic precursor with the brand name Silres MK® was used. It was intended that the lowest possible fibre diameter be produced, whereby multiple systems were trialled. These included melts which utilised the ceramic precursor only, without any additives, followed by trials using three different solvent-based systems. The solvent-based systems consisted of the solvents acetone, chloroform and dimethylformamide (DMF). Acetone was used individually, whereas a 1:1 ratio of chloroform and DMF was utilised in a binary solvent system, with PVP being incorporated into one solution to aid with rheological properties by incorporating a shear thinning polymer.

Each solvent/melt system (Table 5.1) was spun at various rotational velocities to determine the speed at which the smallest fibre diameters were produced. After spinning, fibre diameters were obtained by means of scanning electron microscopy (SEM) and subsequently evaluated using ImageJ software. Results of each fibre diameter measured are shown in Figure 5.4, with different zones demarcated to show the variation of fibre diameter for each system more clearly, demonstrating that the lowest fibre diameters (2.47 μm) were produced using solution 7 (Table 5.2).

Polyvinylpyrrolidone (PVP) was combined with the ceramic precursor in solution 8 in a bid to increase the viscosity and improve the spinnability of the solution by introducing shear thinning behaviour. The PVP acts as a sacrificial polymer which will be removed during pyrolysis. The solutions without PVP were tuneable in such a way that an equivalent or even smaller fibre diameter could be achieved without the use of PVP.

Once the fibres were produced, melt spun fibres were required to undergo a crosslinking reaction which took place utilising an ammonia polycondensation reaction over a period of 60 hrs. During this reaction time, the hydroxyl (O-CH_2-CH_3) and ethoxy groups (OH) react with the ammonia (NH_3) to produce water (H_2O) and ethylene (C_2H_4) as a by-product during crosslinking. Successful crosslinking of the fibres was evaluated by submitting the fibres to elevated temperatures of 200 °C for

1 hour, whereby unsuccessful fibre crosslinking was evident through fibre fusing (see Figure 5.5c).

Solution spun fibres had an organotin crosslinking agent within the solution, which was added immediately prior to spinning. These fibres were also tested at elevated temperatures to evaluate their crosslinking reactions prior to pyrolysis.

Once successfully crosslinked, the fibres underwent pyrolysis to convert the fibres from a preceramic fibre to a glass ceramic fibre. This process took place in an inert nitrogen atmosphere at temperatures reaching 1000 °C, where ramping was as slow as 2 $°C.min^{-1}$. A crucible with lid was used to ensure the fibres were not disturbed during the process, as nitrogen was constantly flowing over the fibres.

We set out to produce a glass ceramic SiOC fibre that was as close to the nanoscale as possible, producing a fibre diameter just above 2 μm from a binary solvent system containing a ceramic precursor and crosslinking agent. The ability to reduce the size of the fibres to below 1 μm does seem possible by tuning the solvent system, polymer weight concentration and/or rotary jet spinning variables.

Ceramic micro/nanofibres are capable of high strength and modulus in both tension and compression. Commercially available ceramic fibres are around 10 μm in diameter with tensile moduli in the region of 170 to 415 GPa [15]. With the ability of rotary jet spinning to produce high volumes of such fibres at the nano- or sub-micron scale versus alternative nanofibre production methods such as electrospinning, it should not be long before this method is used for the commercial production of ceramic nanofibres.

The ability to use the fibres produced from rotary jet spinning will naturally depend on the end use, and ultimately the morphology and properties of the fibres required. To date, it is not possible to produce aligned fibres for use in unidirectional ceramic composites for example, however, applications such as high temperature filtration will benefit greatly from this process. With the ability to regularly operate in harsh chemical and high temperature environments up to 1000 °C, ceramic nanofibres are of great benefit.

5.4 Conclusions

In this study, we focused on achieving small diameter (less than commercial scale) glass ceramic SiOC fibres by rotary jet spinning. A preceramic precursor was used to spin fibres from both the melt, as well as solutions that utilised both a single and binary solvent system. The smallest fibre diameters achieved used a 70 wt.% polymer concentration in solution that consisted of a 1:1 ratio of chloroform and dimethylformamide. Fibres were successfully converted from preceramic fibres to glass ceramic SiOC fibres by means of pyrolysis. It has successfully been established that ceramic fibres can be produced at large scales using rotary jet spinning, however a diameter of 2.47 µm was the smallest achieved so far, allowing scope for a further reduction in fibre diameter through experimentation with solvent systems and optimization of rotary jet spinning processing parameters.

References

1. Peijs, T., *Electrospun Polymer Nanofibers and their Composites*, in *Comprehensive Composite Materials II*, C.H. Zweben and P.W.R. Beaumont, Editors. 2018, Elsevier Ltd. p. 162-200.
2. Wang, H., et al., *Ultralight, scalable, and high-temperature-resilient ceramic nanofiber sponges.* Sci Adv, 2017. **3**(6): p. e1603170.
3. Rahaman, M.N., et al., *Bioactive glass in tissue engineering.* Acta Biomater, 2011. **7**(6): p. 2355-73.
4. De Diego, M.A., N.J. Coleman, and L.L. Hench, *Tensile properties of bioactive fibers for tissue engineering applications.* Journal of Biomedical Materials Research, 2000. **53**(3): p. 199-203.
5. Sigmund, W., et al., *Processing and Structure Relationships in Electrospinning of Ceramic Fiber Systems.* Journal of the American Ceramic Society, 2016. **89**(2): p. 395-407.
6. Guo, A., et al., *Hierarchically structured polymer-derived ceramic fibers by electrospinning and catalyst-assisted pyrolysis.* Journal of the European Ceramic Society, 2014. **34**(2): p. 549-554.
7. Guo, A., et al., *Preceramic polymer-derived SiOC fibers by electrospinning.* Journal of Applied Polymer Science, 2014. **131**(3): p. n/a-n/a.
8. Ren, L., R. Ozisik, and S.P. Kotha, *Rapid and efficient fabrication of multilevel structured silica micro-/nanofibers by centrifugal jet spinning.* J Colloid Interface Sci, 2014. **425**: p. 136-42.
9. Müller, A., et al., *Calcium Cl/OH-apatite, Cl/OH-apatite/Al2O3 and Ca3(PO4)2 fibre nonwovens: Potential ceramic components for osteosynthesis.* Journal of the European Ceramic Society, 2014. **34**(15): p. 3993-4000.
10. Salinas, A., et al., *Production of beta-Silicon Carbide Nanofibers using the Forcespinning (R) Method.* Journal of Ceramic Science and Technology, 2016. **7**(3): p. 229-234.
11. Salinas, A., M. Lizcano, and K. Lozano, *Synthesis of Beta-SiC Fine Fibers by the Forcespinning Method with Microwave Irradiation.* Journal of Ceramics, 2015. **2015**: p. 5.
12. Colombo, P., et al., *Polymer-Derived Ceramics: 40 Years of Research and Innovation in Advanced Ceramics.* Journal of the American Ceramic Society, 2010. **93**(7): p. 1805-1837.
13. Bernard, S., et al., *Boron-Modified Polysilazane as a Novel Single-Source Precursor for SiBCN Ceramic Fibers: Synthesis Melt-Sinning, Curing and Ceramic Conversion.* Journal of Materials Chemistry, 2005. **15**: p. 289-299.
14. Mahalingam, S., et al., *Facile one-pot formation of ceramic fibres from preceramic polymers by pressurised gyration.* Ceramics International, 2015. **41**(4): p. 6067-6073.
15. Motz, G. and R.K. Bordia, *11 - Processing, structure and properties of ceramic fibers*, in *Handbook of Textile Fibre Structure*, S.J. Eichhorn, et al., Editors. 2009, Woodhead Publishing. p. 378-424.

6

Conclusions and Future Work

6.1 Summary

6.1.1 Fibre diameter

Utilising rotary jet spinning (RJS) to produce polymeric fibres was the primary focus in this research project. It was initially hypothesised that it would be possible to produce polymeric fibres which could be classified as nanofibres, having fibre diameters under 100 nm. Initial tests, however, produced fibre diameters from melt RJS between 1000 - 10,000 nm and solution RJS between 250 – 1,000 nm, much larger than expected.

Fibres with diameters averaging in the nanoscale have not consistently been achieved through RJS by many referenced studies, with the average diameter being 10% larger than those produced by electrospinning (ES) when comparing the two processes directly, as discussed in Chapter 1. ES is already known to be the fibre production process having the best capability of producing the smallest mass-produced polymeric fibres, demonstrating that RJS can be a competitive alternative with fibre diameters only slightly higher than those produced by ES.

It should be highlighted that the fibres produced from RJS in this study were not consistently in the nanoscale, with the lowest achieved diameters averaging between 250 –1,000 nm. Melt spinning did not produce sub-micron sized fibres due to the uncharacterised extensional viscosity that seemed to dominate and hinder the ability of the fibres to continue being drawn into smaller fibre diameters.

6.1.2 Material selection

Having the capability to produce fibres from both melt and solution RJS, there was a varied selection in the materials and processing conditions utilised to achieve successful fibre creation. It was discovered that the rheological characterisation of the spinning fluids was crucial in being able to predetermine the spinnability of the polymer solution or melt.

Newtonian flow behaviour was found to be the most processable rheological fluid flow model, having failed to successfully spin almost any fluids that showed non-Newtonian behaviour. If fibre spinning was to be successful, the zero-shear viscosity of non-Newtonian fluids was required to be sufficiently low to ensure rapid viscosity reduction at shear rates approaching 500 – 800 1/s – the shear rates typical in RJS.

Newtonian flow behaviour fluids with viscosities between 1 – 10 Pa.s were always able to produce fibres, however in some instances, when the viscosity was too low due to low molecular weights, chain overlap in polymer melts or low solution concentrations in solution spinning, droplets and discontinuous fibres were formed.

6.1.3 Solvent selection and chamber temperature

Solvent systems play a significant role in the variability in the evaporation time during spinning. If a highly volatile solvent is chosen, the evaporation rate increases and larger fibres are created due to the crystal structures forming more rapidly, ceasing further fibre extension which is responsible for the reduction in the overall fibre diameter.

If the solvent chosen is not very volatile, the evaporation time is increased, leading to the fibres breaking up during spinning where too much solvent is present for too long during the fibre extension process. This can lead to only droplets forming and/or discontinuous fibre mats being produced.

The chamber temperature influences the rate of evaporation, with higher temperatures promoting faster evaporation, which can allow the production process to be tuned to the solvent system being used. During melt spinning, the chamber temperature also affects the spinnability of the fibres, due to the temperature gradients during spinning affecting the cooling rate of the molten polymer. Higher temperatures within the chamber would lead to smaller fibre diameters by promoting a lower cooling gradient over the drawing period from fibre extrusion to capture.

6.1.4 Yield and scalability

Rotary Jet Spinning conducted in this research agrees with the values cited in Chapter 1 regarding fibre yields. It has been quoted that up to 50 times the volume, when compared to electrospinning, is possible when evaluating a single orifice. As electrospinning is typically conducted through the method of individual needle or needless systems which have high power requirements, RJS, with its much lower power requirements, is a more suitable option for large scale production.

The large-scale production of RJS would incorporate several spinneret heads working in unison to produce a continuous non-woven fibre mat.

6.1.5 Rotational velocity

Contrary to initial estimations, the rotational velocity of the spinneret does not have a major contributing factor to the fibre diameter. In studies where multiple spinning velocities were trialled in order to classify the change in fibre diameter in relation to the spinning velocity, it was found that there was no discernible pattern.

Overall, solution spinning was performed at 4,000 to 8,000 RPM whereas melt spinning was performed at 7,000 to 12,000 to achieve the smallest possible fibres. Variations in fibre diameters over these ranges were present and did not consistently reduce in diameter with an increase in rotational velocity.

During the spinning process, it was visually confirmed that higher velocities resulted in greater disorder in the fibre mat, with increased lack of fibre orientation. Although single fibre orientation was not possible in the laboratory scale RJS system utilised, the rotational velocity did affect the “capture” mechanism of the fibres as they were collected on the vertical collector posts. Lower spinning velocities were often used to ensure “good” fibre deposition.

6.2 Future work

All experimental work was conducted using a select number of die geometries, for which data was analysed and conclusions made. On reflection of the variability of the processing completed in this work, future work in this field would benefit greatly from studying the effects of geometrical changes to the spinneret to include a variation in the diameter of the die and its effects on polymer processability, as well as the distance from the rotating axis to the die exit (pressure variations). Variations in deposition and collection methods such as those shown in Figure 6.1 were studied by Capulli et al. [1] and Deravi et al. [2]. They are useful for the development of new and innovative ideas in rotary jet spinning techniques.

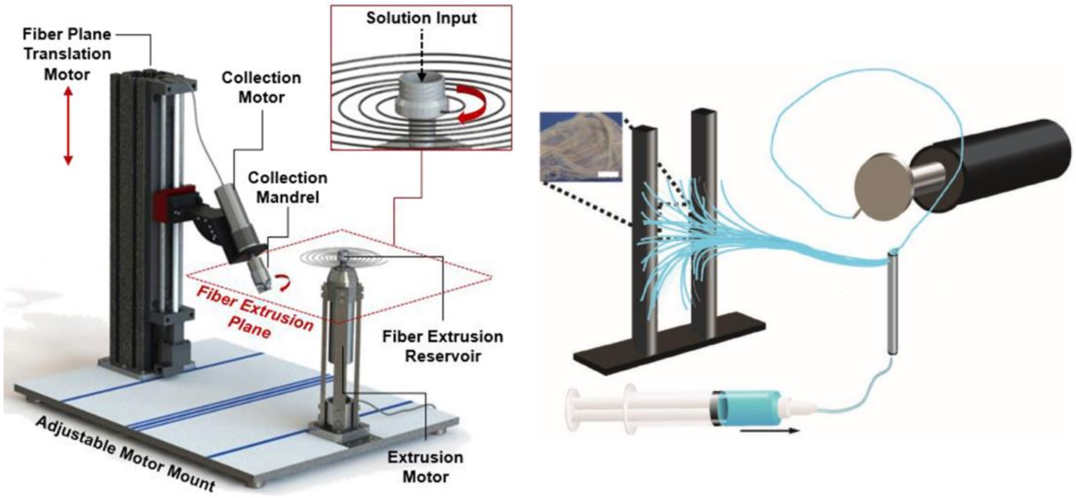

Figure 6.1: Examples of alternative fibre spinning methods, showing work by Capulli et al. (left) and Deravi et al. (right). These alternative methods to conventional rotary jet spinning offer alternatives to collection and deposition techniques.

Capulli et al. were interested in developing an end use product from as-spun nanofibres which were deposited onto a rotating collection mandrel, show excellent use of the rotary jet spinning concept for final product application design. Although not all end products can be adapted to this type of fibre deposition, the variability in the deposition shape as shown by Capulli et al. makes good progress. Similarly, Deravi et al. moved away from the concept of the fluid contained within the spinneret and instead opted for a deposition method that collected the material from a stationary source before centrifugal forces ejected the solution filled pendant drop to a stationary collector (see Figure 6.1). Future work by this author would focus on the fundamental design of the rotary jet spinning apparatus and investigate the variations described, to report on the effects.

Polymer solutions and melts with high viscosities were unable to be spun directly, which is a limiting factor in producing as-spun, high modulus fibres. This is due to the requirements for low molecular weight polymers which exhibit low enough viscosities to be spun. By adding pressure to this system, such as in pressure gyration, it would potentially increase the viscosity range at which fibres could be produced in a conventional rotary jet spinning setup, but relies on the adaption of the spinneret to include a pressure inlet. Further research on the inclusion of pressure vessels in RJS will be required for this to act as another adaptation to the geometry requirements of spinneret. Conclusions from this research could include a variation of spinneret design as per the materials' rheological behaviour to better facilitate a larger range of viscosity processability.

Further numerical and computational modelling is required to fully understand the effects that are present in fibre formation during rotary jet spinning. In the work reviewed in Chapter 1, numerical and computational models have not always considered non-Newtonian flow, with some even utilising inviscid theory. Riahi [3] has started along this theme by utilising a phenomenological viscosity model to understand the behaviour of the polymeric jet as it is stretched after leaving the spinneret. Material properties such as relaxation time and non-Newtonian viscosity are considered in his work, which are understood to impact greatly on the ability to accurately predict fibre behaviour. In Chapter 4, an attempt was made to understand the behaviour of the solution flow through the spinneret, however further work is necessary to construct models for the melt spinning to include thermal effects during pre-heating, soak time, and subsequent spinning.

Even though applications were not directly researched in this Thesis, it is good to comment on the expanding areas of research within rotary jet spinning that continue to focus on materials which are processable at the temperatures and viscosities that are relevant to the successful production of fibres for the given spinneret geometry/equipment that is currently available. Applications for rotary jet spun fibres are continuing along the trends highlighted in Chapter 1, with applications such as insulation [4], energy (battery separators, energy storage, etc.) [5, 6] and composites (both as reinforcement and those with nanofillers) [7, 8] continuing to be actively researched. It is biomedical applications [9-15] however, that remain a front runner in the study of this technology. Further work by this author would include high strength and high modulus fibres from polymeric precursors, as it has been established that high viscosity fluids will not spin fibres without further processing.

References

1. Capulli, A.K., et al., *JetValve: Rapid manufacturing of biohybrid scaffolds for biomimetic heart valve replacement.* Biomaterials, 2017. **133**: p. 229-241.
2. Deravi, L.F., et al., *Design and Fabrication of Fibrous Nanomaterials Using Pull Spinning.* Macromolecular Materials and Engineering, 2017: p. 1600404.
3. Riahi, D.N., *Modeling and computation of nonlinear rotating polymeric jets during forcespinning process.* International Journal of Non-Linear Mechanics, 2017. **92**: p. 1-7.
4. Limura, K., H. Satone, and M. Suzuki, *Fabrication of Water Glass Fibers by Centrifugal Spinning and Characterization of Their Thermal Conductivity as a Heat-Insulator.* Kagaku Kogaku Ronbunshu, 2017. **43**(3): p. 145-149.
5. Lv, R., et al., *Poly(vinylidene fluoride)/poly(acrylonitrile) blend fibrous membranes by centrifugal spinning for high-performance lithium ion battery separators.* Journal of Applied Polymer Science, 2017. **134**(8).
6. Zhang, X., et al., *Preparation and performance of novel polyvinylpyrrolidone/polyethylene glycol phase change materials composite fibers by centrifugal spinning.* Chemical Physics Letters, 2018. **691**: p. 314-318.
7. Jeong, S.-H., et al., *Squid pen-inspired chitinous functional materials: Hierarchical chitin fibers by centrifugal jet-spinning and transparent chitin fiber-reinforced composite.* APL Materials, 2018. **6**(1): p. 016102.
8. Zander, N.E., M. Gillan, and D. Sweetser, *Composite Fibers from Recycled Plastics Using Melt Centrifugal Spinning.* Materials (Basel), 2017. **10**(9): p. 1044.
9. Rampichova, M., et al., *Platelet-functionalized three-dimensional poly-epsilon-caprolactone fibrous scaffold prepared using centrifugal spinning for delivery of growth factors.* Int J Nanomedicine, 2017. **12**: p. 347-361.
10. Upson, S.J., et al., *Centrifugally spun PHBV micro and nanofibres.* Materials Science and Engineering: C, 2017. **76**: p. 190-195.
11. Vocetkova, K., et al., *A comparison of high throughput core–shell 2D electrospinning and 3D centrifugal spinning techniques to produce platelet lyophilisate-loaded fibrous scaffolds and their effects on skin cells.* RSC Advances, 2017. **7**(85): p. 53706-53719.
12. Witkowska, E., et al., *Polymer mat prepared via Forcespinning as a SERS platform for immobilization and detection of bacteria from blood plasma.* Mater Sci Eng C Mater Biol Appl, 2017. **71**: p. 345-350.
13. Cremar, L., et al., *Development of antimicrobial chitosan based nanofiber dressings for wound healing applications.* Nanomedicine Journal, 2018. **5**(1): p. 6-14.
14. Matharu, R.K., et al., *The effect of graphene-poly(methyl methacrylate) fibres on microbial growth.* Interface Focus, 2018. **8**(3): p. 20170058.
15. Zhou, H., et al., *Cotton-like micro- and nanoscale poly(lactic acid) nonwoven fibers fabricated by centrifugal melt-spinning for tissue engineering.* RSC Advances, 2018. **8**(10): p. 5166-5179.